Development of a Hardware-in-the-loop Platform for Hybrid and Electric Vehicles

By

Mohammad Basiri

A thesis

presented to the University of Waterloo

in fulfillment of the

thesis requirement for the degree of

Master of Applied Science

in

Mechanical Engineering

Waterloo, Ontario, Canada, 2012

AUTHOR'S DECLARATION

I hereby declare that I am the sole author of this thesis. This is a true copy of the thesis, including any required final revisions, as accepted by my examiners.

I understand that my thesis may be made electronically available to the public.

Abstract

On a larger scope, improving the hybrid electric vehicles (HEVs) and electric vehicles (EVs) could address the public concern on climate changes and environmental issues. While ongoing research at the University of Waterloo targets improving HEVs and EVs through studying their various components, there was a pressing need to develop setups or tools to assist in the progress of this research. Hence, the primary problem at hand was the time-consuming and costly procedure of developing individual experimental setups/tools for the proposed experiments.

The approach taken to solve these interconnected challenges was the design and development of a modular test bench capable of running various hardware-in-the-loop (HIL) studies on HEV powertrain components. The HIL approach was adopted in order to increase the accuracy of computer-generated simulations through the use of physical components in combination with software simulations. MATLAB Simulink software was employed to create the models and programs, which were then downloaded to dSPACE, a device employed to control the various components of the test bench. The scope of this project expanded not only to accommodate specific experimental setups, such as the HWFET drive cycle test, but also to consider modularity requirements that would address unforeseen circumstances and experimental needs. Meeting the modularity requirements would greatly reduce the cost and time needed for running the experiments.

As a result of this project, a test bench was developed with four major components: a modular area (for attaching various physical components that comprise the proposed experiment's setup), a control panel, a dSPACE, and the electrical energy supply and load. Through running various experiments, numerous components of the test bench were characterized. The developed test bench is capable of accommodating various experimental setups as well as producing relevant data for further analysis. The implications of this project are that the ongoing research on HEVs at the University of Waterloo can now employ the test bench to run proposed experiments more effectively in order to obtain more accurate data.

Acknowledgements

Apart from my own efforts, just like any other project, the success of my project greatly depends on the encouragement and guidelines of many others. I would like to take this opportunity to express my gratitude to people who have been instrumental in the successful completion of my project. First and foremost, I would like to sincerely thank my thesis supervisor, Dr. Amir Khajepour, in the department of Mechanical and Mechatronics Engineering, for providing me the opportunity to work on my project "Development of a hardware-in-the-loop platform for hybrid and electric vehicles" while continuously guiding and supporting me throughout the completion of my study.

Furthermore, I would like to avail myself of this opportunity and express a sense of gratitude and love to my friends and family, especially my beloved parents for their moral support, and strengthening positive energy. Without their unconditional support and inspiration this project would not have materialized. I am truly grateful for their constant support and help when it was most required.

Table of Contents

List of Figures

List of Tables

List of Abbreviations

HIL	Hardware-in-the-Loop
EV	Electric Vehicle
HEV	Hybrid Electric Vehicle
SOC	State of Charge
HPPC	Hybrid Pulse Power Characterization
PID	Proportional, Integral, Derivative
PWM	Pulse Width Modulated
DC	Direct Current
AC	Alternating Current
ICE	Internal Combustion Engine
SIL	Software In the Loop
PHEV	Plug-in Hybrid Electric Vehicle
ISG	Integrated Starter Generator
ANL	Argonne National Laboratory
MATT	Modular Automotive technology test bed
ADC	Analog Digital Converter
DAC	Digital Analog Converter
EPA	United States Environmental Protection Agency
HWFET	Highway Fuel Economy Test
CVT	Continuously Variable Transmission
GPU	Graphic User Interface

Chapter 1 Introduction

Recently, public concern has been shifting significantly towards climate change, environmental issues, greenhouse gases, and the depletion of global fuel supplies, leading government and industry researchers to develop more energy-efficient and environmentally-friendly vehicles. While the research is targeted towards improving vehicle efficiency by studying various components, there is a clear need to develop tools to assist in the research. However, as developing separate experimental tools for various studies is time-consuming and costly, the design and development of a modular test bench that is compatible with the requirements of several different studies is highly beneficial for ongoing research in this field. Consequently, the ongoing research on hybrid electric vehicles (HEVs) at the University of Waterloo, Waterloo, Canada, has prompted this project. Specifically, through a comprehensive study of HEVs and the various research approaches taken (e.g., software- and hardware-in-the-loop), a modular test bench is designed, fabricated, and tested for hardware-in-the-loop analysis of HEVs.

Why hybrid electric vehicles

There are several options in a vehicle to produce the required power. These choices are internal combustion engines (ICE) and the electric motors. Conventional vehicles employing the ICE raise major concerns. Firstly, the combustion reaction uses fuel and air as the reactants in order to release heat and combustion products. While heat is a useful product that is converted to mechanical energy, some of the toxic side products such as nitrogen oxides, unburned hydrocarbons and carbon monoxides pollute the environment and are harmful for living organisms [1]. Furthermore, internal combustion engines are inefficient when operating to supply peak power necessary for acceleration. Additionally, the ICE is inefficient during frequent start-stop operations, which are routinely required in urban driving [2].

In contrast, an electric vehicle utilizes electrical energy supplied by a battery or fuel cell, producing kinetic energy to run the vehicle. Some of the advantages of an electric vehicle include its zero emission, high start torque, lower heat produced (compared to an ICE engine), and lower noise. On the other hand, some of its disadvantages include high vehicle cost and low range due to the low content of the currently used electrical energy storage systems in electrical vehicles. Many research

efforts are now directed towards developing an improved vehicle that overcomes the ICE and electric vehicle problems.

By combining the advantages of both internal combustion engine and an electrical motor, HEV systems have become one of the best working solutions. HEVs utilize the advantage of the fuel's highly dense energy storage (which is lacked by electrical energy storage systems), allowing for ease of energy storage transport. Furthermore, considering that the ICE is inefficient at low speeds, the employment of an electric motor in an HEV overcomes this disadvantage. Also, in urban driving, where the vehicle is subject to frequent stops (due, for instance, to red lights), the ICE can be turned off and quickly started again in HEVs, preventing the ICE engine from working in idle status. This enables HEVs to achieve low emission and lower fuel consumption.

At cruise speed, an HEV relies more on the ICE, which has better efficiency as well as the capability to charge batteries. Moreover, an HEV can capture lost kinetic energy during braking, resulting in improved vehicle efficiency. Also, in plug-in hybrid electric vehicles (PHEV), the batteries can be recharged using electrical energy from the grid. As a result of the stated benefits, HEVs offer a solution that achieves higher fuel efficiency and environmental compatibility. Figure 1-1 illustrates the automotive development over the past few years as well as its future trends [3].

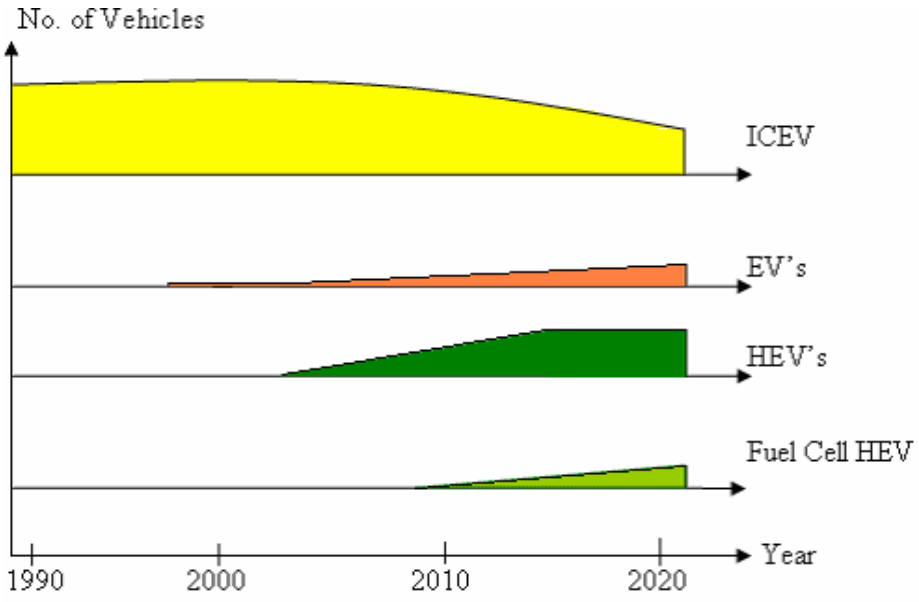

Figure 1-1: Automotive development over the past few years and future trends [3].

Towards higher accuracy testing

Without a doubt, the complexity of an automobile design requires tools that allow an efficient and accurate way to analyze the many involving variables and factors. Nowadays, computers play a significant role by assisting engineers in the design, testing, and optimization stages of vehicle development. While computers allow development of preliminary simulations for various engineering tests by using a system commonly referred to as software-in-the-loop (SIL), having physical components can help to improve the accuracy of these simulations. To achieve higher accuracy and to obtain more realistic results in studies, hardware-in-the-loop (HIL) simulations have been used by engineers. HIL achieves better accuracy in real-time tests by enabling the interactions of actual (physical) components of the system and virtual (computer-based) simulations.

Research contribution

As mentioned previously, research on HEVs is ongoing, primarily in response to public concern regarding environment of related issues. The goal of this project is to increase the accuracy of data obtained for future HEV studies. In order to do this, a scalable and modular test bench has been designed and fabricated that can easily be upgraded in accordance to requirements of the designed real-time simulations and tests. The device responsible for controlling different components of the test bench is a dSPACE RTI1006. MATLAB Simulink software is used to create models and programs, which are then downloaded to the dSPACE. Furthermore, with Control Desk software, it is possible to monitor the program's variables and to vary them in real-time tests. The scalability and modularity of the test bench allow for easy addition and removal of components in accordance with the proposed test plans, such as the requirement for different HEV configurations. Moreover, the test bench contains almost all the components of a HEV powertrain, which enables full hardware studies with a higher accuracy. The test bench can also be used effectively for other electric and hybrid electric vehicle powertrain studies as part of an ongoing automotive research at the University of Waterloo. Figure 1-2 shows a schematic of the test bench.

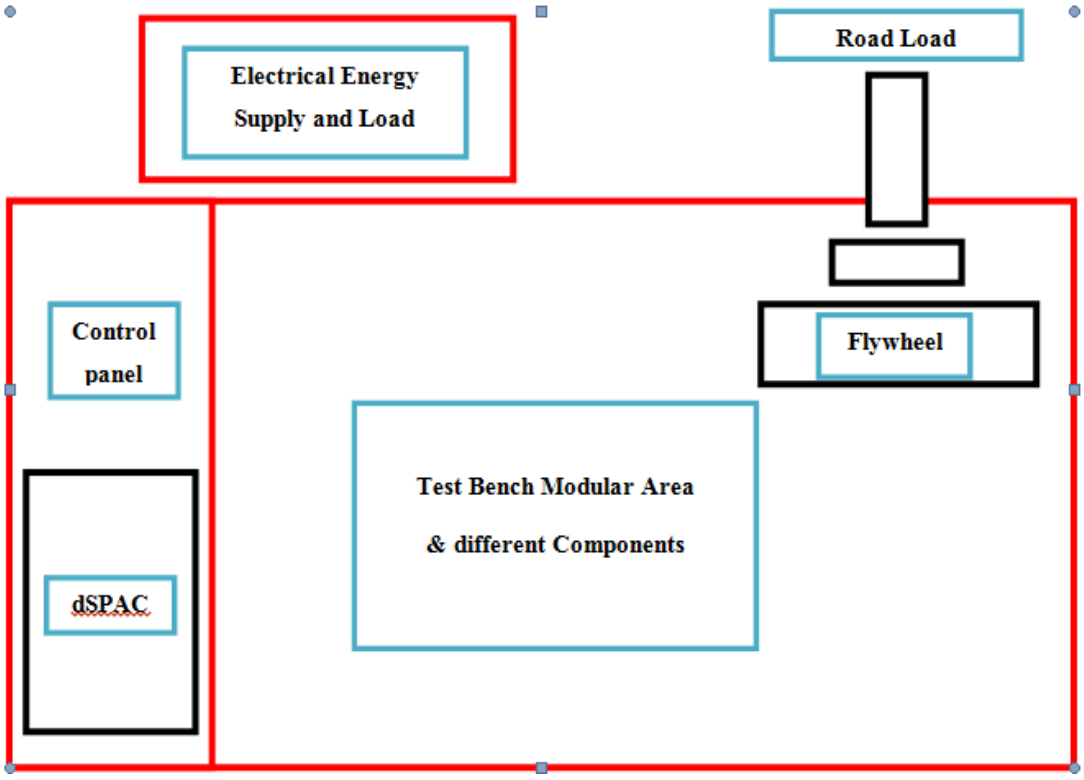

Figure 1-2: Test bench schematic.

The research is presented in five chapters. Chapter 2 presents a literature review of HEVs and an overview of HIL test platforms. Chapter 3 provides a comprehensive explanation of the fabricated test bench and a brief description of its components and functions. Chapter 4 presents the results of various tests that were conducted to find tuned computer models of the components; it also gives the results of the HWFET drive cycle energy consumption test. Finally, Chapter 5 concludes the thesis and provides suggestions for future work.

Chapter 2 Background

2.1 Introduction

For more than a century, both industry and academic researchers have been focusing on developing improved technology while aiming for increased fuel efficiency and more environmentally friendly vehicles. The first HEV was reported in France in 1899 [4]. It was a parallel hybrid electric vehicle with a small air-cooled gasoline engine supported by an electric motor and lead-acid batteries; it also boasted a novel electric starter. The first series HEV was introduced in the same year. This vehicle had a ¾ hp gasoline engine to run a 1.1 kW electric generator that charged the vehicle's batteries for a higher range. Boosted by these early successes, engineers and scientists have been researching and developing alternative solutions for HEV ever since [1].

2.2 HEV's Powertrain and Architecture

The function of a vehicle's powertrain is to produce the power for the vehicle and to carry the energy required to sustain the vehicle's essential driving range. While a vehicle can have more than one powertrain (each driving on various power sources, such as diesel, an electric motor system, or a chemical battery), the term "powertrain" is used to refer to the system of power sources and energy convertors as a whole. The HEV is an example of a hybrid vehicle that uses an electrical powertrain in combination with one other powertrain [1].

There are various types of powertrain configurations in HEVs. Each of these configurations has its particular characteristics and method of operation. HEVs often use a combination of no more than two powertrains. As stated, one of the two powertrains in an HEV is an electric powertrain, which, as implied, employs an electric motor. The second powertrain discussed here is an ICE. The connection between these two powertrains defines the type of HEV architecture. Generally speaking, an HEV can have a series, parallel, or a series-parallel architecture.

2.2.1 Concept of HEV drivetrain

An HEV drivetrain has many possible routes for energy flow. As depicted in Figure 2-1, nine combinations of routes for power flow are used to meet the load requirements. The various combinations of routes for delivering the required power to the load are listed below [1], [5]:

Traction: Power delivery to load from:

1. Only Powertrain 1
2. Only Powertrain 2
3. Both Powertrain 1 and 2 at the same time

Battery Charging: Source of power for Powertrain 2

4. The load (regenerative braking);
5. Powertrain 1
6. Both Powertrain 1 and the load at the same time

Various power delivery combinations:

7. Powertrain 1 to load and Powertrain 2 at the same time
8. Powertrain 1 to Powertrain 2; Powertrain 2 to load
9. Powertrain 1 to the load, the load to Powertrain 2

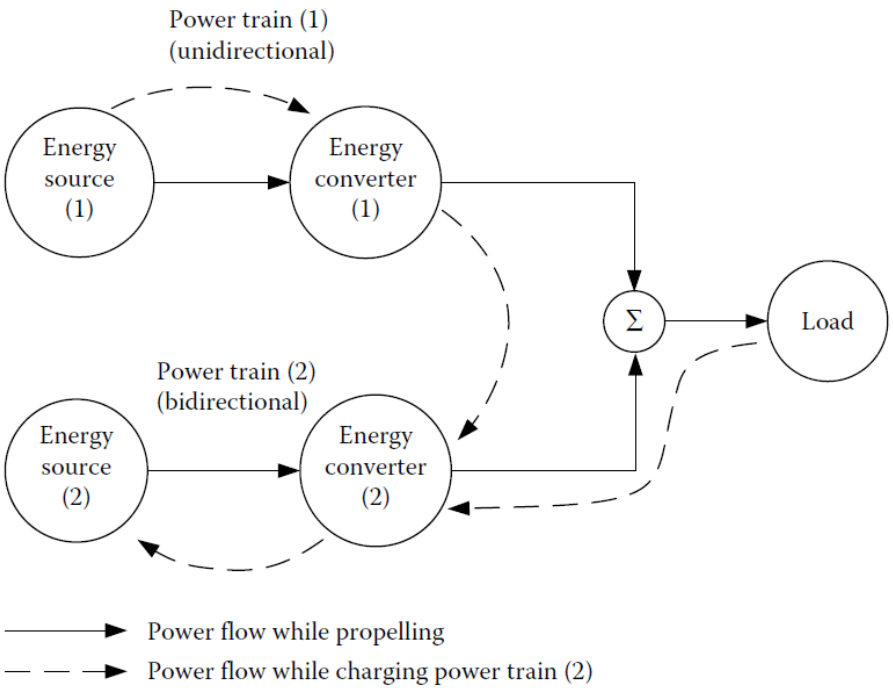

Figure 2-1: Conceptual illustration of a hybrid electric drivetrain [1].

In operation mode, a vehicle's load power randomly fluctuates as a result of variations in speed or due to climbing up and down grades. As shown in Figure 2-2, the load power can be decoupled into two signals. The first signal shows the average (steady-state) power as a constant in time, while the second signal shows the dynamic power corresponding to fluctuations as a function of time. The average of the dynamic power signal would be zero. Interestingly, an HEV employs the use of its powertrain to supply each of these signals. Specifically, the IC engine, which favors steady-state operation, could be used to supply average power, and the electric motor supplies dynamic power.

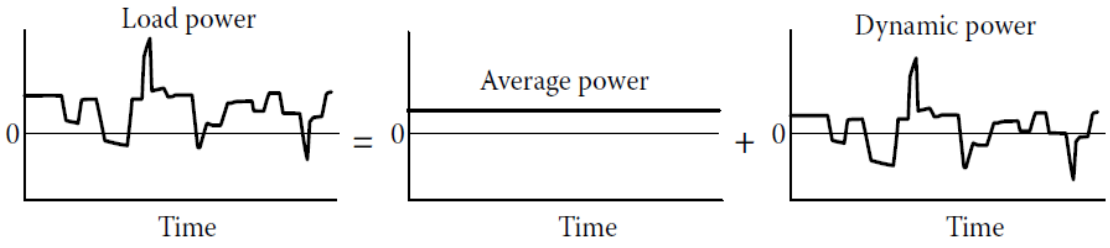

Figure 2-2: Load power is decomposed into steady and dynamic components [1].

During one driving cycle, the total output energy of the dynamic powertrain would be zero, implying that the energy capacity of the power source is not lost at the end of the driving cycle. In effect, the dynamic powertrain functions as a power damper. An IC engine or a fuel cell is employed to provide the power for the steady-state load. Since, as mentioned, the IC engine favors steady-state operation, it allows the operation point to be designed and controlled within an optimal region in order to achieve the highest operational efficiency. On the other hand, the electric traction system, consisting of the traction motor and the chemical batteries, provides the dynamic load power. This allows the vehicle to meet peak power demand and recover braking power [6][1].

Various vehicle manufacturers utilize a hybrid configuration consisting of a gasoline or diesel engine along with a motor linked to a generator with a battery system. The concept of the hybrid drivetrain can be employed by various architectures, such as series HEV, parallel HEV, and the series-parallel HEV, as discussed in detail below [7], [8]. In the following, HEV configurations are briefly reviewed.

2.2.2 Series HEV

In series configuration, there are two electric motor-generators in the vehicle. One of the motor-generators is driven by the IC engine and operates as a generator to charge the battery. Subsequently, the stored electrical energy is delivered to the other motor-generator responsible for driving the wheels and propelling the vehicle. This configuration is illustrated in Figure 2-3. As mentioned earlier, the problem with electrical energy storage in, for instance, batteries is that they have low content potential. To solve this problem in HEVs, an ICE with a high content energy gas tank is

added to an EV drive train. Furthermore, the series HEV configuration allows the vehicle to work in the electric mode, giving off zero emissions.

Series HEVs have many advantages. For example, there is no mechanical connection between the ICE and the wheels, so the ICE can work at a speed that is best in terms of fuel efficiency. This advantage has allowed engineers to design a more efficient ICE for a specific speed. Also, in the series configuration, where electric motors can work closely to the ideal profile of torque-speed, the addition of a CVT or multi-gear transmission to the drive train may not be necessary. Therefore, the drive train can be significantly simplified, lowering vehicle cost. An additional advantage is that the control strategy of this type of HEV can be simplified more than other configurations due to the ICE and the wheels being fully decoupled [1].

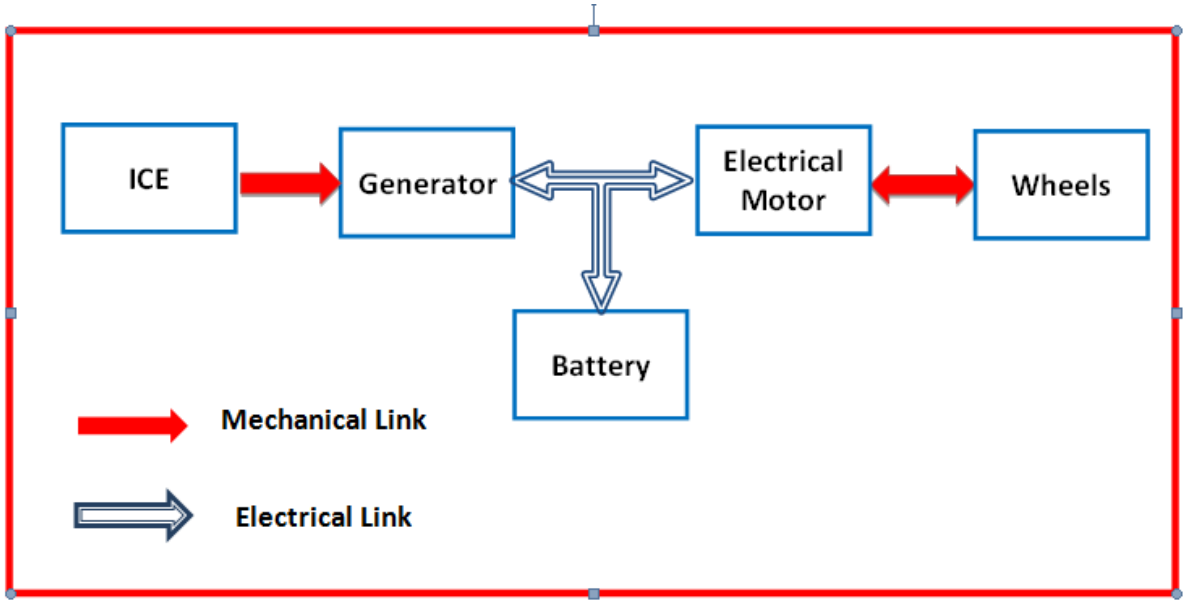

Figure 2-3: Schematic of series HEV.

2.2.3 Parallel HEV

The parallel configuration is able to offer many advantages due to its ability to switch between two power sources, such as the internal combustion engine and the electric motor. This allows the vehicle to selectively employ the power sources separately or in combination, according to their optimal/high efficiency range. In other words, the choice of configuration for utilizing the engines depends on driving conditions. If necessary, both power sources can be utilized simultaneously to attain maximum output power and peak performance. In driving conditions where vehicle speed does not vary significantly (i.e., during highway driving), the system can rely solely on the IC engine to drive the wheels. This achieves the highest efficiency. However, when driving in the city (where the IC engine would be operating at its lowest efficiency), the electric motor is utilized, resulting in a higher overall efficiency [7]. Figure 2-4 shows the system configuration of a parallel hybrid electric vehicle.

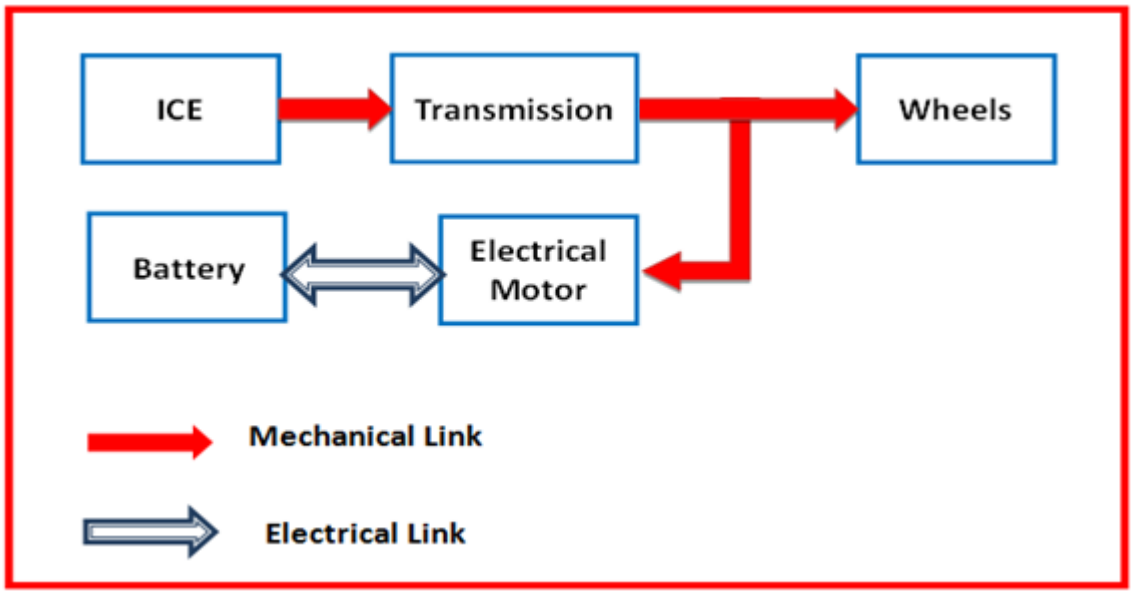

Figure 2-4: Schematic of a parallel HEV.

2.2.4 Series-parallel HEV

Another configuration is the series-parallel HEV. Figure 2-5 illustrates a typical example of this powertrain configuration, which utilizes a planetary gear unit for decoupling engine and wheel speeds. The planetary gear unit is shown in Figure 2-6, where the motor-genarator speed is ω_1, vehicle speed is ω_2 and engine speed is ω_3. Table 2-1 shows the speed-torque relationship between three gears of the planetary gear unit. By adjusting the motor-generator speed at a given vehicle speed, the engine speed can be adjusted as well. The series-parallel HEV's power flow route is comprised of the motor-generator, the engine, and the planetary gear unit. Furthermore, at a negative (opposite direction versus the torque) motor-generator speed, the electric motor would be operating in the generating mode. Here, the engine's power is divided into two and transferred to the generator and the drivetrain. A positive motor speed results in the motor-generator being able to operate in traction mode, increasing power to the driven wheels. As a result, through controlling motor-generator speed, the engine speed can be adjusted in its optimal region. The traction motor is another source in order to add torque to drive wheels. [1], [5], [9], [10].

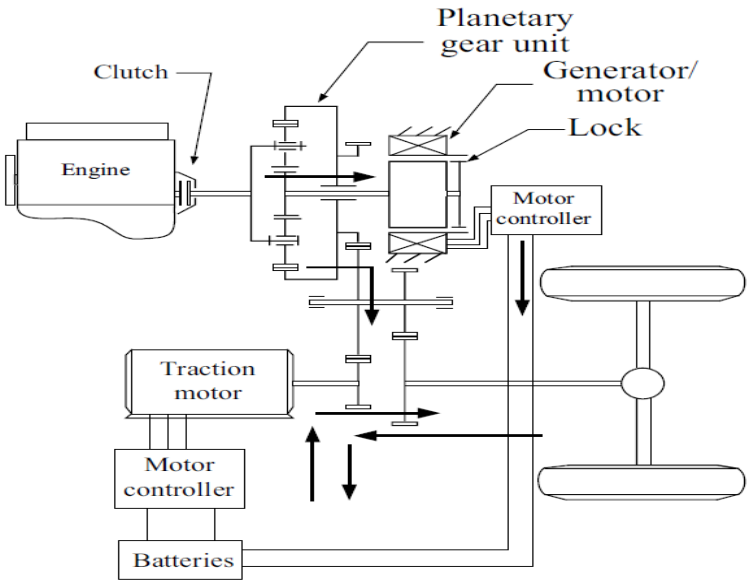

Figure 2-5: Series-parallel hybrid drivetrain by using a planetary gear unit [5].

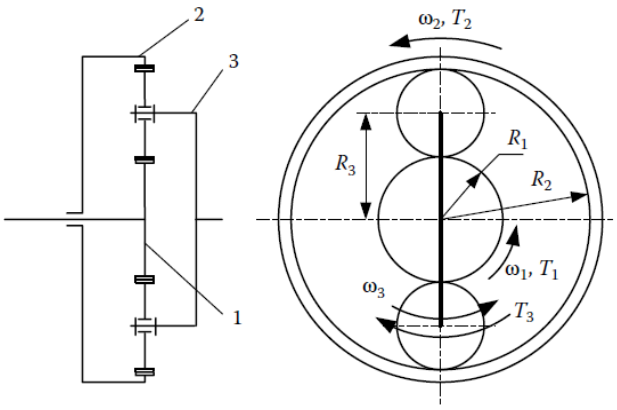

Figure 2-6: Planetary gear unit used as a speed-coupling device [1].

Element fixed	Speed	Torque
Sun gear	$\omega_3 = \frac{i_g}{1+i_g}\omega_2$	$T_3 = -\frac{1+i_g}{i_g} T_2$
Ring gear	$\omega_3 = \frac{1}{1+i_g}\omega_1$	$T_3 = -(1+i_g)\, T_1$
Yoke	$\omega_1 = -i_g\, \omega_2$	$T_1 = \frac{1}{i_g} T_2$

Table 2-1: Speed and torque relationships while one element is fixed [1].

2.2.5 Plug-in HEV (PHEV)

The advancement of hybrid vehicle technology has given birth to the plug-in HEV (PHEV) [11]. Due to its externally chargeable high energy density battery pack, a PHEV can run solely on electrical power for a longer range compared to regular HEVs [12]-[16].

Figure 2-7 illustrates the architecture of a plug-in parallel hybrid vehicle. With the aim of enhancing the efficiency of HEVs, many companies have been converting conventional HEVs into PHEVs by adding a high energy density battery pack or by replacing the HEV's battery pack in order to extend the driving range while relying on electrical power. The new battery pack is required to have the

capability of storing sufficient electrical energy from external charging and regenerative braking. Furthermore, it must be capable of supplying the traction motor system with the stored electrical energy [17].

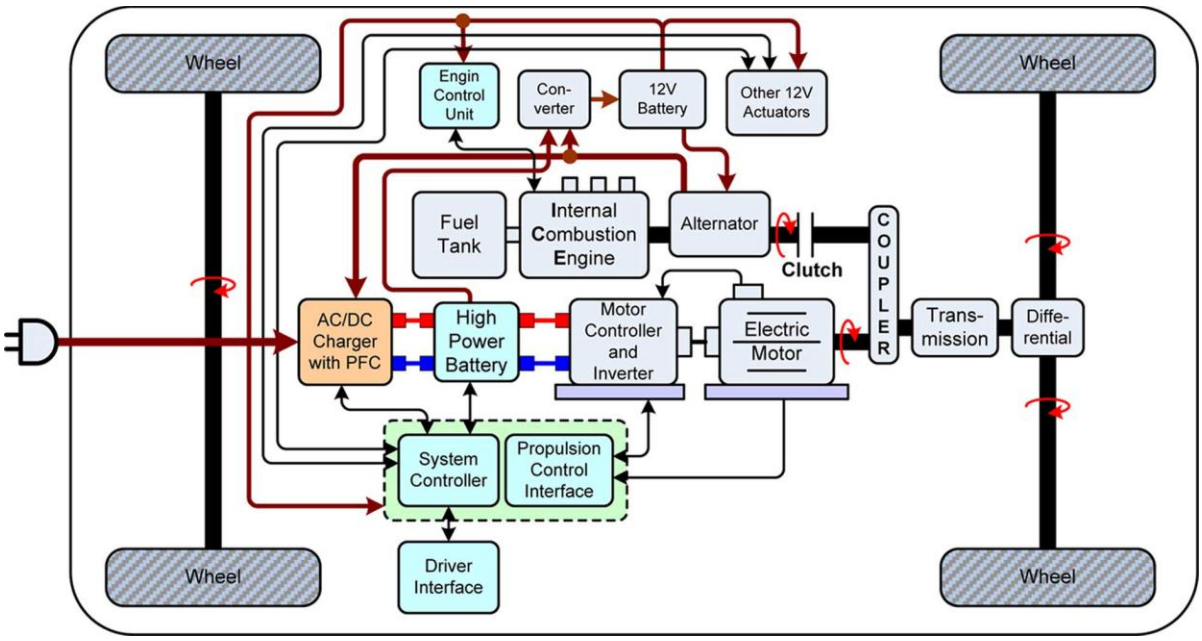

Figure 2-7: Plug-in hybrid electric vehicle (parallel configuration) [17].

AC outlet charging requires a few components. First, it must have a battery charger that consists of an AC-DC convertor with a power factor correction (PFC). As well, it requires a programmable digital controller with a suitable voltage-current profile for the high-energy battery packs. Moreover, to transfer energy between the battery and the traction motor system, a bidirectional DC-DC converter and charge-discharge profile is also necessary.

Although PHEVs offer substantial advantages, several issues still need to be addressed. Examples of such issues include stability concerns of simultaneously utilizing a large number of high-power battery chargers with PFC, cell-balancing of high energy batteries (lithium batteries) for applications in automotive, and safety and thermal management [17].

2.3 Hardware-in-the-loop Testing

While computer models are often used to simulate actual components of a system for real-time hardware studies, these simulations are not always a plausible choice for modeling systems or subsystems, due to lack of accurate models or uncertainties. To overcome these issues, this technique is actual components in line with virtual computer-based simulation models are used. Called hardware-in-the-loop (HIL) simulations, that employs actual components to enhance the accuracy of test results HIL has been applied to various disciplines.

The application of HIL systems covers a wide range, including powertrain controllers, unmanned underwater vehicles, automotive safety systems and aircraft [18]-[22]. Hence, HIL systems are powerful methods for HEV powertrain studies [21], [23]-[27]. The advantage of using HIL is that it significantly reduces costs by eliminating the need for building expensive full-sized prototypes for test analysis of drivetrain systems. Often, the hardware developed for HIL simulations are scaled-down versions of actual-sized components that are built to evaluate performance and feasibility rather than fully recreating the original system [23]-[28]. Using the HIL in a closed-loop configuration would be useful in studying interactions between highly coupled subsystems that exist in HEVs [29].

Figure 2-8 and Figure 2-9 illustrate a system developed by the Harbin Institute of Technology. It is capable of running tests on various electric motor and engine combinations in parallel with simulations on transmissions and high voltage battery components [30]. However, while the test bench designed here is flexible, it is too large and not portable.

Argonne National Laboratory (ANL) developed a modular HIL test bench referred to as a Modular Automotive Technology Test (MATT) bench. This system is designed to operate on a chassis dynamometer. Although this system is mobile (due to being integrated with automotive suspension components), it is not appropriate as a passenger vehicle. As shown in Figure 2-10, MATT is designed solely as a test bench that meets higher flexibility and mobility criteria. MATT is illustrated in Figure 2-10 in a configuration that explores an engine, transmission and final drive, while a high voltage battery and electric traction motor hardware were imitated. Both of the above-mentioned models are capable of performing engine, controller HIL, and electric motor simulations [31].

Figure 2-8: Harbin Institute of Technology HIL test bench [30].

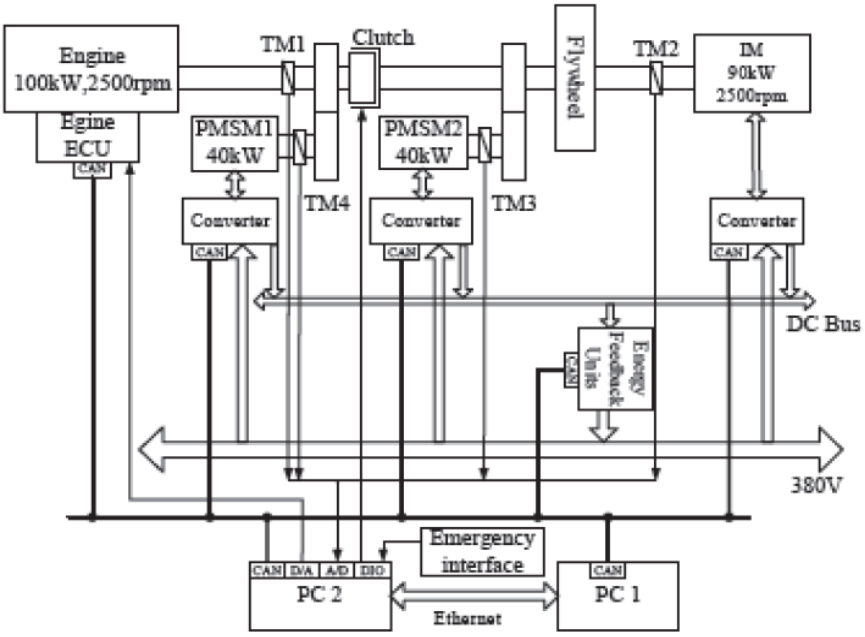

Figure 2-9: Harbin Institute of Technology HIL test bench diagram [30].

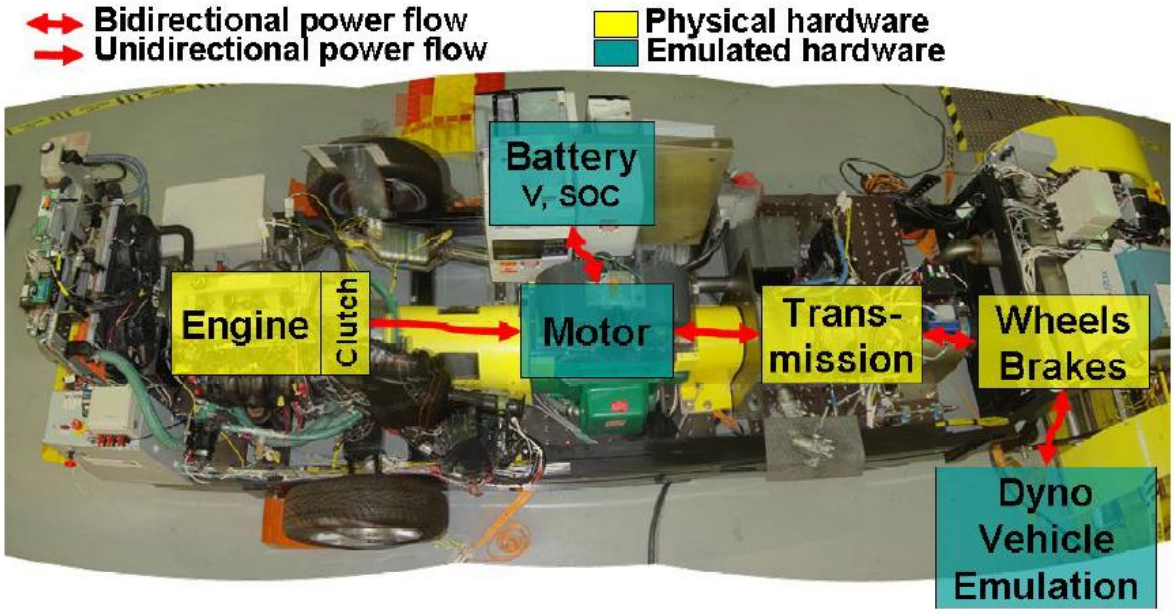

Figure 2-10: Argonne National Laboratory Modular Automotive Technology Test bench [31].

On the other hand, both the ANL HIL and the Harbin Institute of Technology test benches are designed to test full-size vehicle components. This is useful, as it removes the complexity of having to deal with scaling component factors.

Summary

In this section, the concept of HEVs was described and various HEV architectures were explained. A brief description of plug-in HEVs has also been provided, along with a discussion of HIL simulations.

Chapter 3 Test Bench Design

In light of the amount of effort directed at EV and HEV research as well as the variations in HEV configurations, there is a need for a more complete modular test bench. At the University of Waterloo, a project to develop a modular test bench was initiated, with the goal of conducting future studies. The aim was to create a single test bench that would be capable of achieving the various configurations of components to allow testing numerous EV and HEV architectures. Some examples of these tests are mentioned in Chapter 4. The development of this test bench involved engineering design of hardware and software components. Figure 3-1illustrates the four main components of the test bench, namely the test bench workspace, the electrical energy supply and load, and the control panel with the dSPACE on top of it. The test bench is illustrated in Figure 3-2.

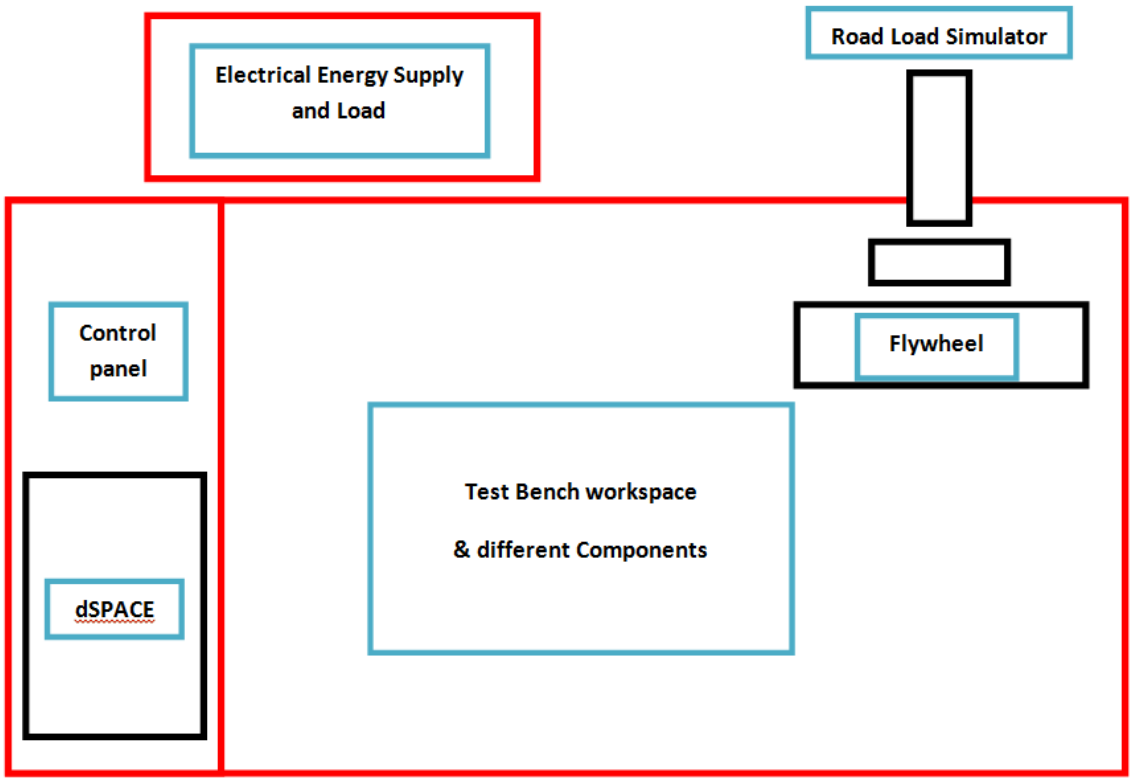

Figure 3-1: Test bench schematic.

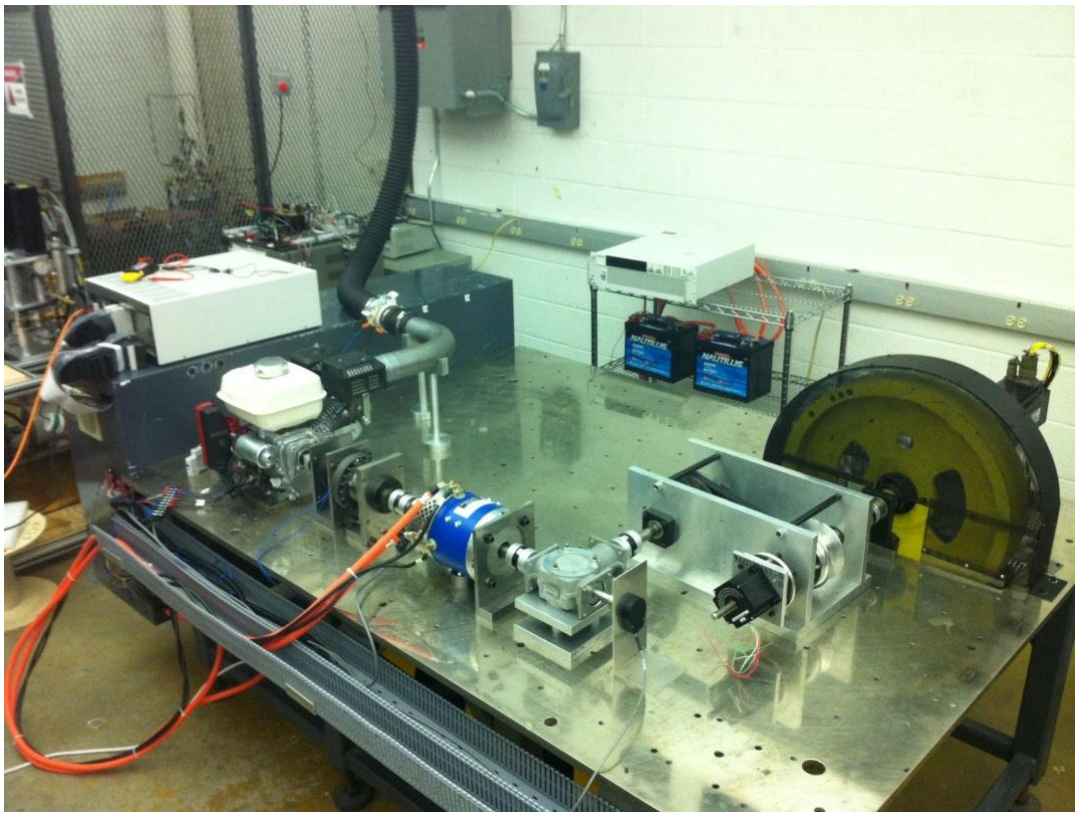

Figure 3-2: Test Bench.

Figure 3.3 illustrates the test setup control idea. The programming and control of this test setup is done in MATLAB Simulink environment. The MATLAB Simulink file is then downloaded onto the dSPACE. The dSPACE is a real time interface which has input/output electrical boards in order to generate signals to control the control panel unit and also to read the signals from different sensors. The control panel is composed of many electrical circuits and is designed and fabricated to control all the components such as the power supply, the batteries, and the ICE. Another software that aids the User is the Control Desk software. Having developed a Graphical User Interface (GUI) in the Control Desk software, the user is provided with the capability to fully control and monitor the desired variables. The GUI allows the monitoring of the different sensed values, controlling the different components of the test setup, and varying the variables of the MATLAB Simulink file in real time testing. The following sections further discuss the various parts and components of the test setup.

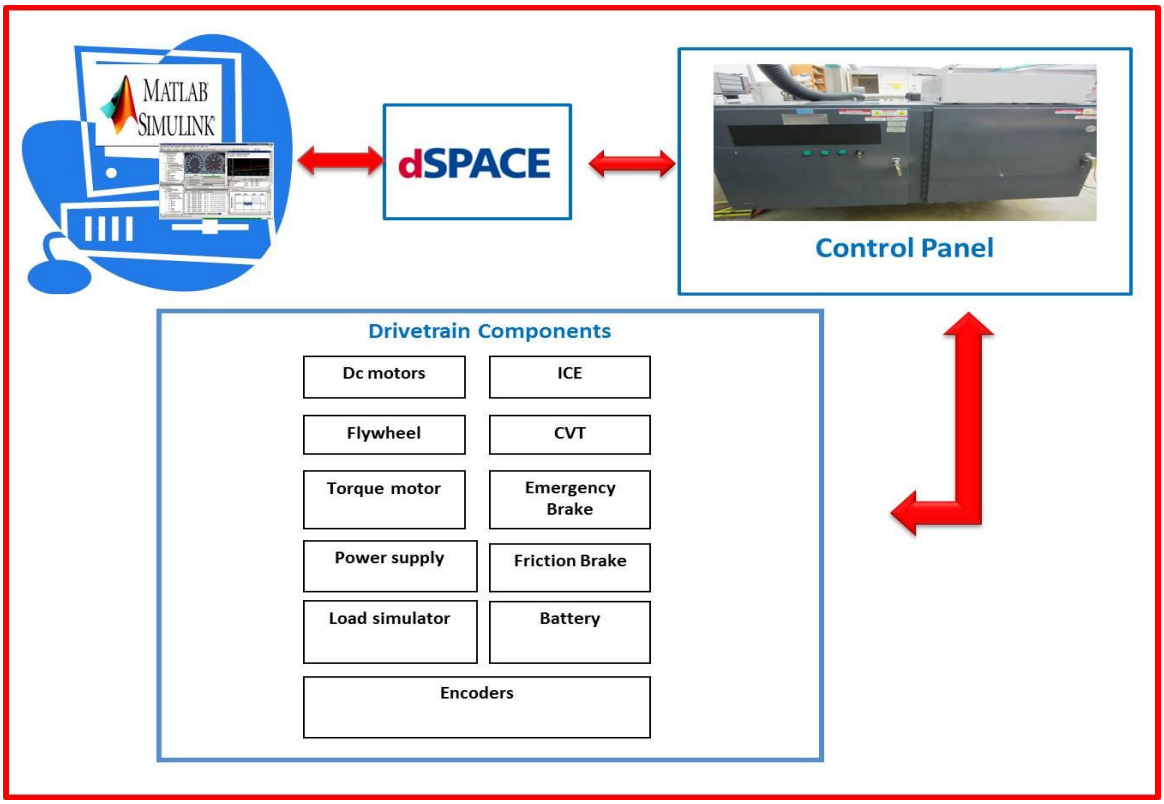

Figure 3-3: Control schematic of the test bench.

3.1 dSPACE Controller

For the overall control of the test bench, a dSPACE controller with an RTI 1006 processor board and four added boards are used. Figure 3-4 illustrates the dSPACE controller. The RTI 1006 processor board has a 2.4 GHz processor quad-core and an RS232 serial port. The four boards added to this board in the dSPACE controller are DS2103, DS4004, DS2002 and DS3001.

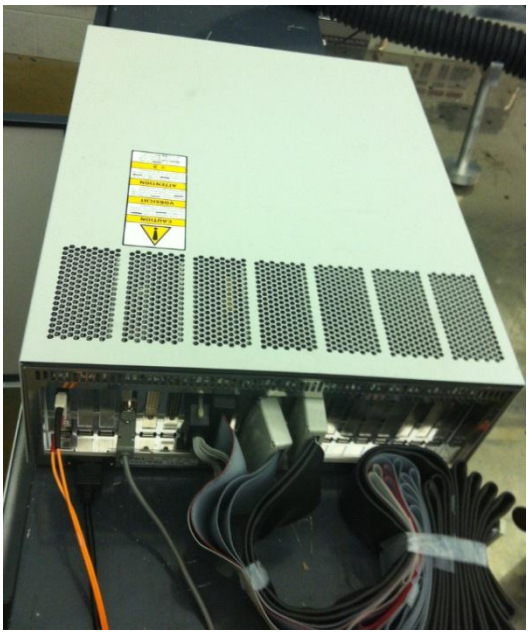

Figure 3-4: dSPACE Controller.

The DS2103 is a digital-to-analogue convertor board (DAC) that can convert digital data to analogue voltage with a maximum 5mA current supply, a voltage range of -10V to +10V, and a resolution of 16 bits. This board is used to control the components that require a voltage input. Examples of these components include the DC motor driver, the DC load driver, the power supply, and the electrical load.

The DS4004 is a digital output board with a digital output of 5V. This board is used to control all on/off components such as the fan, the power supply, the electrical load power, the various solid state relays, the contactors, and the emergency brake.

The DS2002 board is an analogue-to-digital convertor (ADC) with an input voltage of -10 to 10V and a maximum resolution of 16 bits. This board is used to read the voltage output of sensors such as voltage sensors and the current sensors.

The DS3001 board is employed to read the encoders' outputs. This board can connect to five different encoders at the same time and read them in real time.

To program the dSPACE, the desired program is coded in MATLAB Simulink (Figure 3-5) and later downloaded into the dSPACE processor. Subsequently, using software called Control Desk 4.0 Next Generation (Figure 3-6), a real-time (online) monitoring of each variable can be performed. Using this software, it is possible to adjust the value of each variable and graph the data for later analysis.

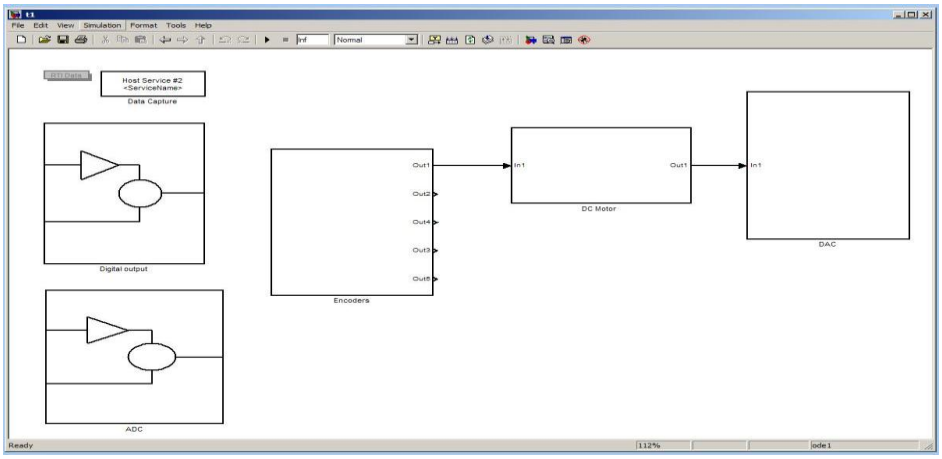

Figure 3-5: MATLAB Simulink file for test bench.

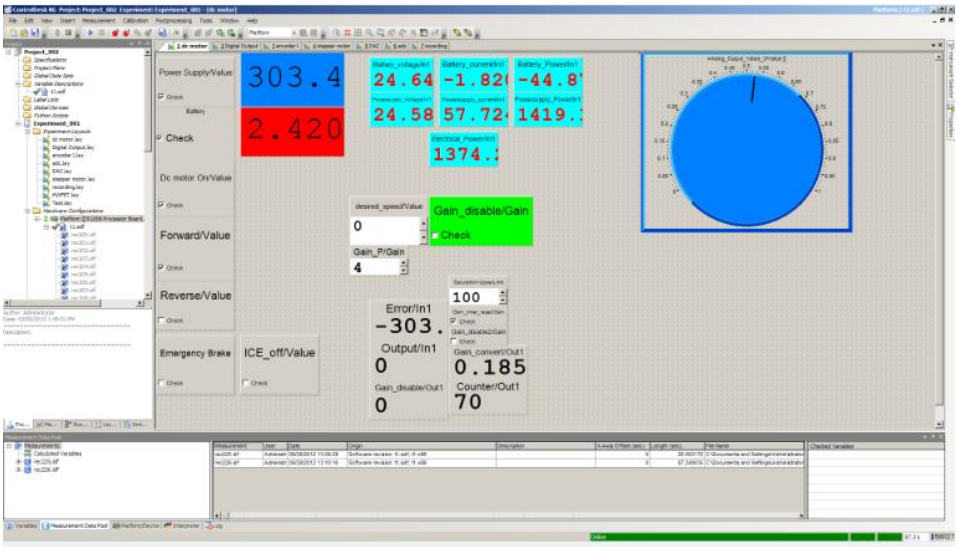

Figure 3-6: Control Desk software.

3.2 Test bench workspace

In the test bench workspace, the physical (hardware) components of the hybrid electric vehicle powertrain can be attached for different purposes. As can be seen in Figure 3-2, the metal table has numerous tapped holes. These holes and holders fix the location of a desired component on top of the table for the duration of the testing procedure. The flexibility in determining the orientation of the component placement and their relationship to one another is a feature designed to meet the modularity criterion of the test component. The modularity feature is beneficial for conducting numerous studies requiring different arrangements of components. As discussed below, there are nine components in this test bench. A major advantage of this table is that its function is not limited to just these nine components. It is easy to add new components or use as many of them as required by the experimental procedure. In the following the main components of the test bench are discussed and their models are derived.

3.2.1 DC motor

The electric motor is a key component of HEVs and EVs. As stated previously, one of the powertrains in an HEV belongs to an electric motor and its electric power source. Generally speaking, an HEV's electric motor has two modes. The first mode is when the motor is a traction motor that generates mechanical power. The second mode is when the motor is a generator, making electrical power from the mechanical power applied to it. Considering that the two motors' modes have different characteristics, choosing the right motor plays a critical role in HEV performance and fuel consumption. It is thus very important to have sufficient knowledge of the motor and its functionality. This is where graphs related to power and motor-torque-speed profile are useful. The ideal torque-speed contour for the traction area shows a constant power for all speeds [32]. A constant power profile results in maximum acceleration performance of the vehicle at given power ratings or at minimum power ratings at given acceleration performance [33], [34]. Figure 3-7 shows the ideal torque-speed profile of an electric motor.

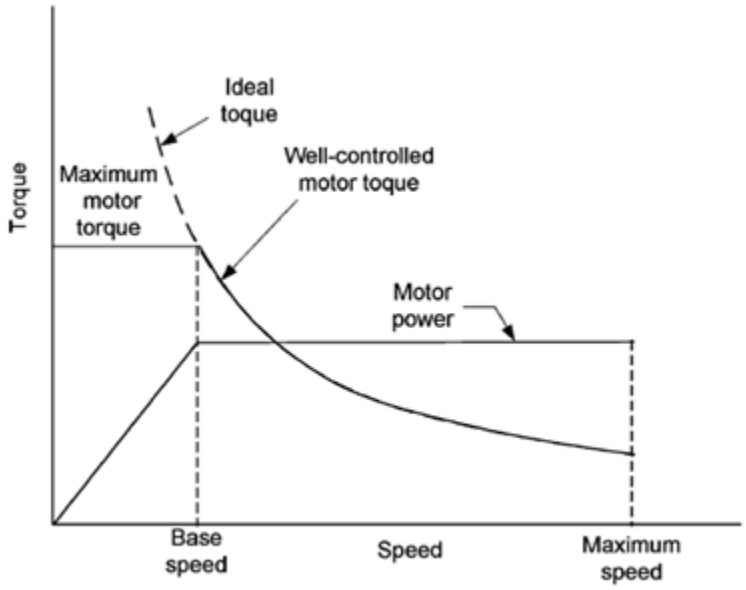

Figure 3-7: Ideal torque-speed profile required that a well-controlled motor can produce [34].

There are many different types of motors that could be employed in EVs and HEVs. These are generally classified into AC and DC motors. Each of these two classifications has different types. For example two important types of DC motors are permanent magnet DC motors and separately-exited DC motors. The field of a permanent magnet DC motor is generated by a constant magnet, whose only control is on the armature of the motor. In a separately-exited DC motor, the field flux can be separately changed via changes in currents passing through the field coil. There is more control on this motor, as the current of both the field and armature can be varied. This will allow the user to maximize control of the power and the motor's torque-speed profile. In fact, this is the reason for employing the use of a separately-exited DC motor. The DC motor used in this test bench is a separately-exited 24V DC motor which generates a 5hp mechanical energy with a nominal speed of 3600 rpm. Figure 3-8 shows the E3-71A-52 model DC motor.

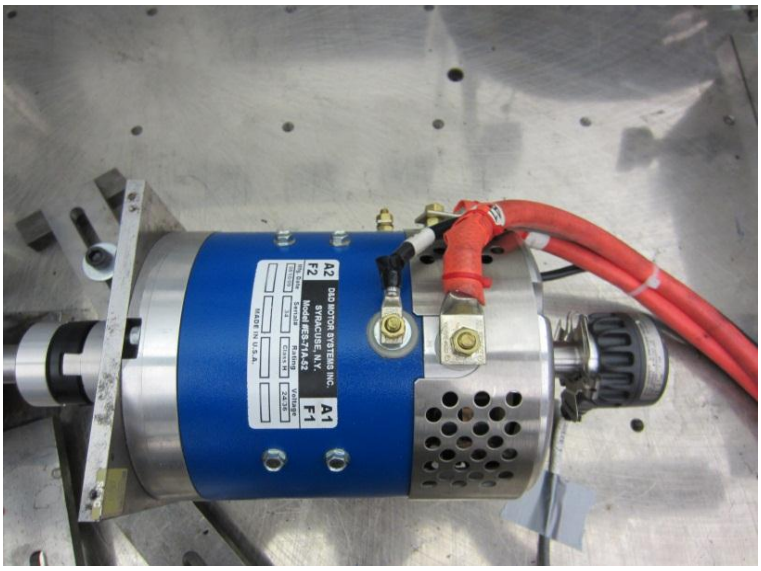

Figure 3-8: DC motor.

In Section 4.2, a case study is conducted on this DC motor to delineate its essential profile for both motor and generator modes. Further factory-supplied details are available in Appendix B.

In order to control the DC motor, a Navitas TSX 500 motor driver was used (Section 3.4.1 discusses the motor driver further). This motor driver can power the field and armature separately, providing enhanced freedom in controlling the torque and speed of the motor in the test bench. For example, while the motor is employed to generate power from ICE in the series configuration, the amount of power it generates can be kept at maximum or optimal points. This requires changing the field and armature's maximum motor drive currents and choosing the appropriate signals to be sent from the dSPACE to the motor driver. In Section 4.4, more information is provided. The motor driver needs an analog voltage as an input command assigned as a throttle input signal. Figure 3-9 shows the MATLAB Simulink PID controller block with a speed feedback from the encoder, which is attached to the motor's shaft. As well, the Control Desk's layout shows how to manually or automatically control the motor's operation.

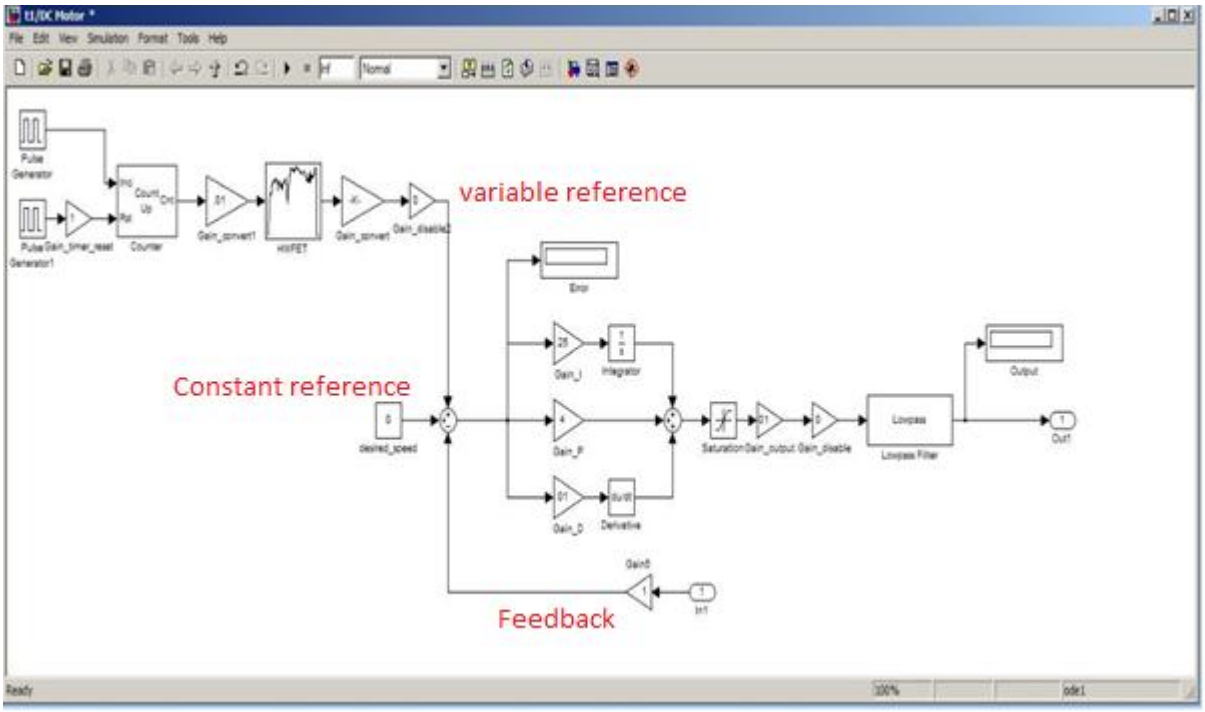

Figure 3-9: DC motor PID controller in MATLAB Simulink.

3.2.2 Internal combustion engine (ICE)

One of the most important powertrain components of all hybrid electric vehicles is the internal combustion engine, or ICE. The Honda GX 200 is the ICE that is used in the test bench. It can produce a maximum power of 5.5 HP equal to 4.1 KW, at 3600 rpm. Section 4.4 further discusses information about the fuel consumption of this motor. GX 200 can produce 12.4 Nm torque at a speed of 2500 rpm [35].

It is important to have control of the ICE. The only degree of freedom is the speed of this motor, and speed control is via a throttle on the side of the engine. In order to move the throttle, a servo motor has been added. Figure 3-10 shows a picture of the motor and the controllable throttle. The servo motor is connected to its power supply and also to the dSPACE in order to control the frequency and width of the pulse which has been generated through the dSPACE to control the servo motor position.

Figure 3-10: ICE and throttle controller with graduate gas cylinder.

An exhaust is hooked up to a fan to remove the ICE's fumes and blow them outside. Figure 3-11 shows a picture of the fan used to vacuum the smoke. The ICE can be turned on in three ways. The first way is starting the engine manually. The second way is with a starter motor which draws a 12V power from a lead-acid battery and is controlled by the dSPACE, giving it the ability to turn on the engine in 3 seconds. The third method to turn on the ICE is with the main DC motor. This method is called Integrated Starter-Generator (ISG). Most manufacturers are interested in using ISG, as it starts the ICE quickly and quietly. ICEs in HEVs are classified as smaller engines compared to conventional vehicle ICEs. With this method, it is possible to cold-crank an HEV ICE. ISGs also have the following advantages: (1) low cost; (2) minimal changes in the electrical system; (3) no need to change the mechanical design; (4) very easy to implement [17]. In this test bench, to turn on the ICE, the DC motor first starts the ICE and then the ICE starts working. Subsequently, the ICE generates

mechanical power and the DC motor converts that mechanical power to electrical power and charges the batteries.

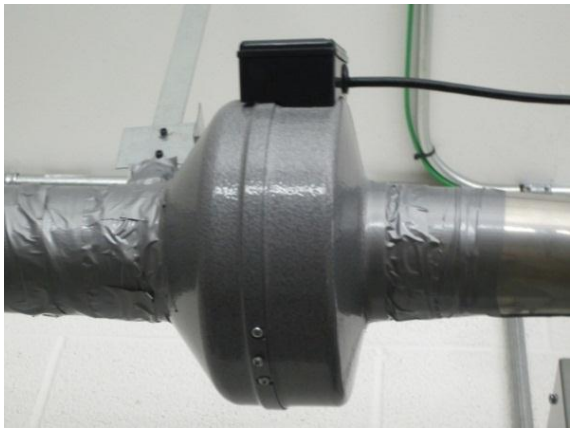

Figure 3-11: Exhaust fan.

3.2.3 Road load simulator motor

To broaden the scope of the test bench for various studies, adding capabilities to simulate various road conditions as external effects was considered. Being able to simulate road conditions allows one to obtain more realistic results using a test bench. The road conditions fall into one of two categories. The first category considers all possible road conditions that assist the movement of the car, such as moving downhill. These conditions are resembled as a positive load on the flywheel axle, which would be produced by the positive torque generated by the motor. The second category considers all negative road conditions that are against the movement of the car, such as moving uphill or tires rolling resistance. These resemble a negative load on the flywheel axle, which would be produced by the negative torque generated by the motor.

As shown in Figure 3-12, the motor employed for this apparatus is a three-phase brushless servo motor, which operates at 460V with a rated power of 5 horse power. The maximum torque provided by this motor can be up to 13 Nm with a rated speed of 3500 rpm [36]. The motor is controlled by an Emerson MX-1600 that is further discussed in the control panel section.

Three-phase brushless servo motor

Rated speed: 3500 rpm

Rated power: 5 HP

Voltage: 460 V

Figure 3-12: Road load simulator motor.

3.2.4 Flywheel

When studying the powertrain components of a vehicle, its mass becomes a crucial component. Consequently, the flywheel is introduced as a test bench component that represents a scaled-down vehicle mass. Figure 3-13 shows the flywheel employed in the test bench.

Using the SolidWorks model of this flywheel, the inertia is measured to be 3.994 kg.m^2. The flywheel stored kinetic energy can be obtained using:

$$E = \frac{1}{2} I\omega^2 \tag{3.1}$$

where (I) inertia is in $kg.m^2$ and speed (ω) is in rad/s.

Furthermore, the kinetic energy of a moving object is:

$$E = \frac{1}{2}\, mv^2 \tag{3.2}$$

Where v is the speed of the object and m is the mass. By equating these two equations, it is possible to find the desired speed of the flywheel. For example, in the Highway Fuel Economy Test (HWFET), which is a standard drive cycle test introduced by the U.S. Environmental Protection Agency (EPA) [37], the maximum speed of the car is 96 km/h. For a desired car with a mass of 157 kg, the maximum rotational speed of the flywheel can be obtained using the following equation:

$$\frac{1}{2}\, mv^2 = \frac{1}{2}\, I\omega^2 \tag{3.3}$$

$$\omega = 167.5\ {}^{rad}/_{sec} \equiv 1600\ rpm \tag{3.4}$$

In some studies, the flywheel can be considered as an energy source. For example, in heavy hybrid vehicles, the flywheel is used for the storage of energy. In order to save the energy, the motor can increase the speed of the flywheel so that when energy is needed, the motor is switched to the generator mode and the stored kinetic energy in the flywheel is converted to electrical energy, producing the additionally required energy.

Figure 3-13: Flywheel.

3.2.5 Encoders

In order to measure the speed of the test bench components, three appropriate encoders are used. Details about the encoders can be found in Appendix F. As an example, Figure 3-14 displays one of the encoders that in placed for the measurement of the DC motor shaft speed.

Figure 3-14: Encoder.

3.2.6 Friction brake

Another component of the powertrain is the friction brake, which is employed to reduce the flywheel speed as needed. In other words, in experimental tests, the speed of the vehicle, represented by the flywheel, would decrease when the friction brake is activated. In order to decrease the flywheel's speed, the motor is switched to generator mode, starting the generation of electrical power. This is commonly referred to as regenerative braking. However, sometimes regenerative braking is not sufficient to decrease speed to the desired level, so a friction brake is added to the system to help the regenerative braking reach the desired speed level using the appropriate braking torque.

The results of experimental tests using the friction brake can be found in Section 4.3, showing how the DC motor and friction brake work together to reach a certain speed. The friction brake employed in the test bench is a 24V DC, as shown in Figure 3-15. A DC load controller produces a varying voltage in a range of 0V to 24V, that in supplied to the friction brake. The voltage is proportional to the torque provided. In order to obtain the relationship between these two parameters (voltage and torque) of the friction brake, a computer model has been developed.

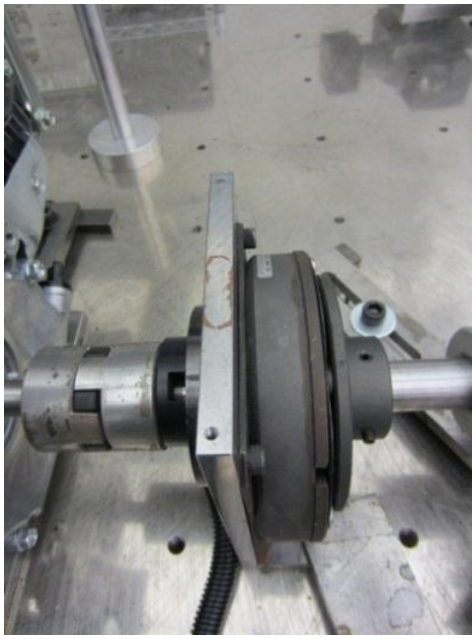

Figure 3-15: Friction brake.

3.2.7 Emergency brake

For safety purposes, there is a need to quickly bring the flywheel to a full stop in case of emergency. To achieve this, an emergency brake is put in place behind the flywheel. This brake requires a 24V DC voltage, which generates a negative torque of up to 200 Nm, sufficient for stopping the system in less than 4 seconds. Figure 3-16 shows the emergency brake connected to the flywheel.

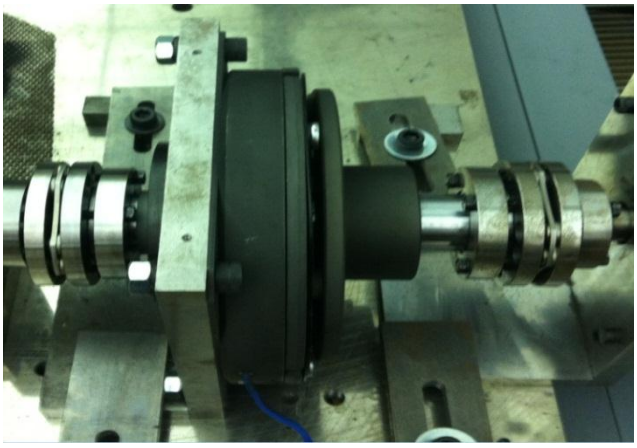

Figure 3-16: Emergency brake.

3.2.8 Clutch

In some HEV configurations, a clutch is needed to connect the ICE to the drivetrain and disconnect it. Similarly, in this test bench the clutch is employed to provide the ability to add or remove the ICE component from the powertrain. The clutch is controlled by a 24V solid state relay located in the control panel. Figure 3-17 illustrates an image of the clutch.

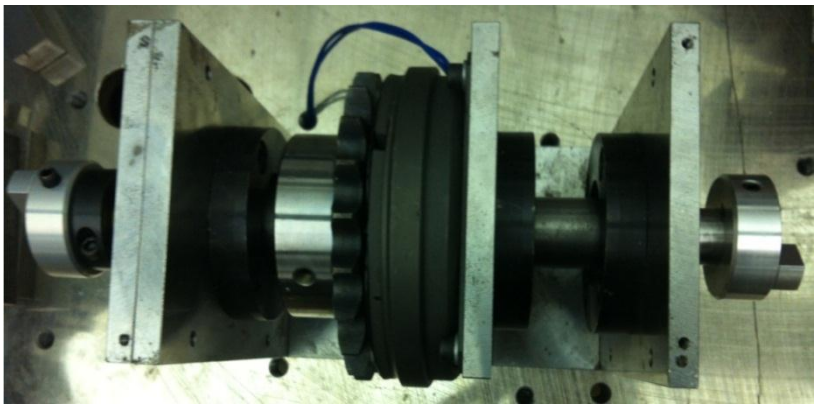

Figure 3-17: Clutch.

3.2.9 Continuously Variable Transmission (CVT)

The CVT is an intermediate component between the motor and the flywheel, allowing one to control the ratio of the input speed (applied by the motor) to the output speed (applied to the flywheel). The CVT was designed and fabricated in order to fulfill the special requirements and needs of the test bench. The CVT's input-to-output ratio varies between 0.24 and 0.97, and is controlled by a linear actuator. The linear actuator is a 48V stepper motor that is controlled by a stepper motor controller located in the control panel. The stepper motor was purchased from Haydon Switch & Instrument Inc. and the driver was purchased from Oregon Micro Systems Inc. Figure 3-18 displays the CVT and the stepper motor connected to it in order to change the ratio of the CVT.

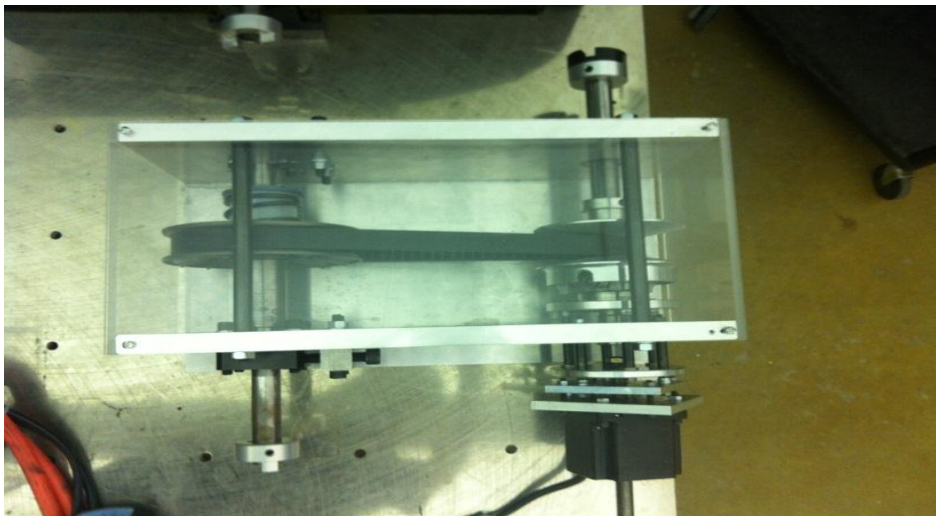

Figure 3-18: CVT.

3.2.10 Gearbox

In order to overcome the dimensional limitations of the test bench, it was necessary to allow a greater variability in the orientation of component placement. The gearbox selected for this purpose allows for better use of the space on the test bench by making 90-degree changes in axel direction possible with a gear ratio of one. Additionally, the straight point of attachment is developed for fulfilling the modularity requirements, accommodating the attachment for encoders or other components. Figure 3-19 shows the gearbox used in the test bench.

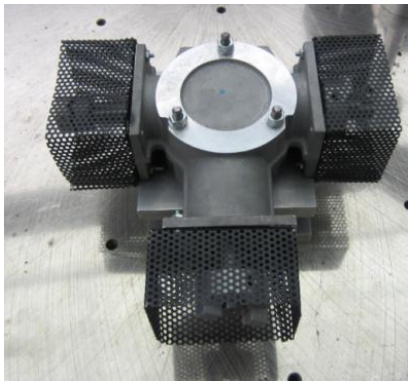

Figure 3-19: Gearbox.

3.3 Electrical Energy Supply and Load

The electrical energy source is composed of a power supply, a power load simulator and lead-acid batteries that not only supply power but can also be used for power-load-related experiments. The power supply and batteries are used to supply energy to the DC motor. In the generator (regenerative) mode, the motor's produced energy can be stored in the batteries or used by the power load. The electrical wiring of the three components is shown in Figure 3-20. To fulfill modularity requirements, the electrical bus has been designed and fabricated to allow the attachment of other sources, such as a lithium ion battery.

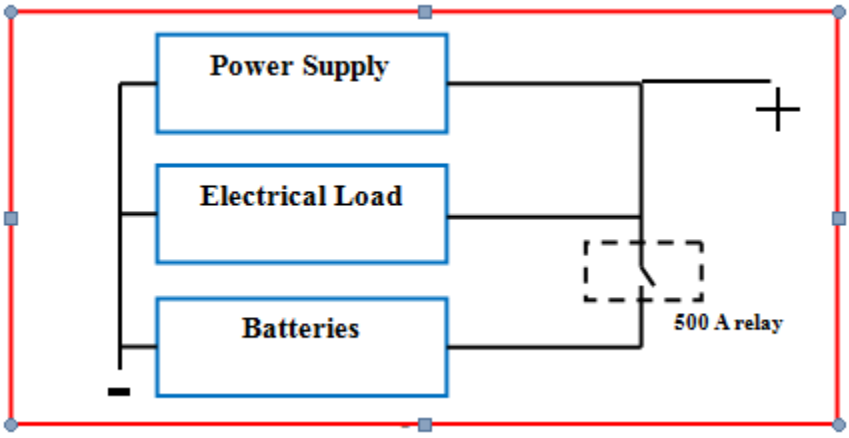

Figure 3-20: Electrical energy supply and load.

The power supply and power load are fully controllable by the dSPACE controller. As a result, this system allows various types of hardware-in-the-loop simulations to be performed. Figure 3-21 shows an example of an HIL simulation, where the battery is the component under study and the power supply and the power load are controlled based on the vehicle model. Tests are carried out in Chapter 4 showing how different degrees of control are possible with these three components used as a full electrical energy pack. The ability to control and program the combination of these components together makes it possible to integrate various types of energy packs. For example, to use a different type of battery, the user simply needs to know how that battery works and what the characteristics of

that battery are. Then, by applying a different variable, the energy pack can be controlled to act as the desired battery with appropriate internal resistance or current response time.

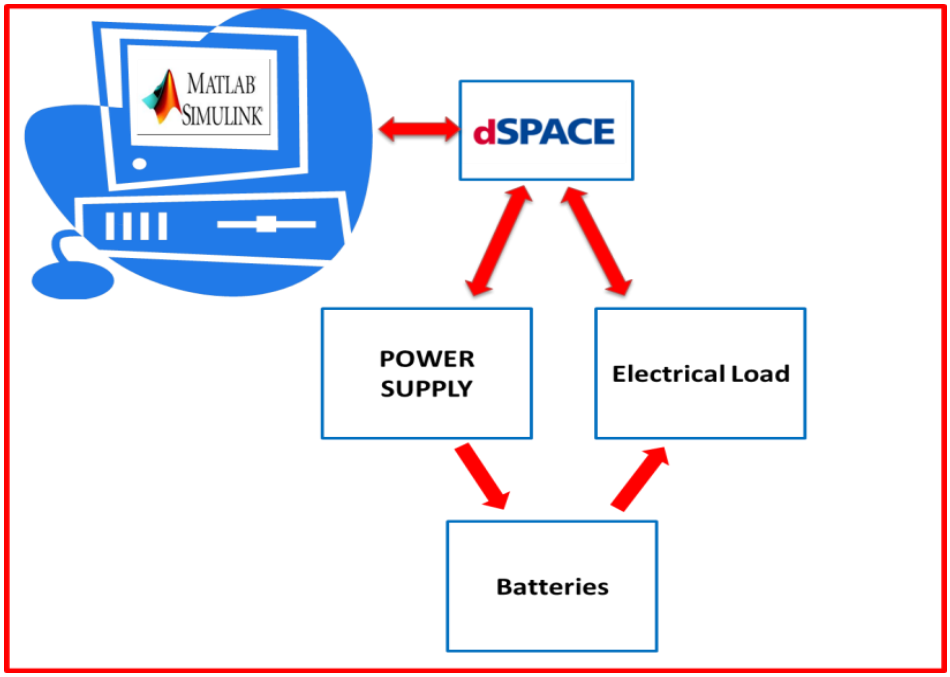

Figure 3-21: HIL example.

3.3.1 Power supply

The digital controllable DC power supply is a Xanrex XDS 30-200 model that is controlled by the dSPACE 2103 board. The power supply can produce up to 200 A with a voltage range of 0V to 30V DC. The dSPACE board used to control the power supply is a Digital to Analog Converter (DAC) and is further described in Section 4.1. Figure 3-22 shows the power supply.

Figure 3-22: Power supply.

3.3.2 Electrical Load

The controllable digital electrical load is a WCL 232 50-1200-12000 model with an upper limit of 12000 Watts. The electrical load is used for various purposes acting as a constant current, constant voltage or constant resistor load on the electrical bus. This electrical load is another component that is controlled by the DS2103 board and is an integral component used in HIL simulations. Figure 3-23 shows the front view of the electrical load.

Figure 3-23: Electrical load.

3.3.3 Lead-acid battery

Two lead-acid batteries are placed in series, producing the 24V DC power necessary for the electrical bus. The type of battery used is the deep cycle lead-acid battery that maximizes the percentage use of the stored charge. The cranking current of this battery is 1000 A. A comprehensive study involving

computer modeling is performed on the lead-acid batter to find its internal resistor and state of charge (SOC). This is further discussed in Chapter 4. Some examples of lead-acid batteries are displayed in Figure 3-24.

Figure 3-24: Lead-acid batteries.

3.3.4 Lithium ion battery

The test bench also has a lithium ion battery. This battery has a Battery Management System (BMS) with related software that monitors the SOC and the current flow controller variables. The BMS connects to the computer with a National Instrument USB interface adaptor, as shown in Figure 3-25. Figure 3-26 presents the bqWizard software used for monitoring the voltage, the current, and the SOC of the battery in real time.

Figure 3-25: Lithium ion battery.

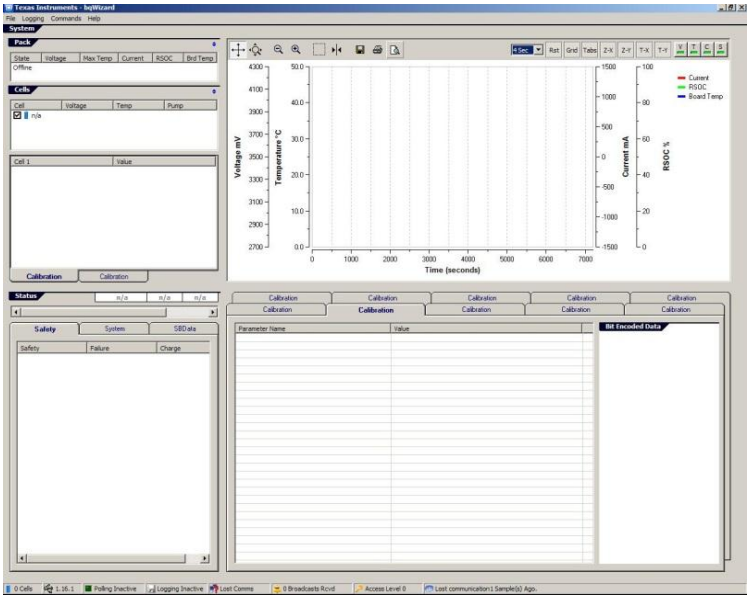

Figure 3-26: bqWizard software.

3.4 Control Panel

As stated previously, components for controlling the test bench work with different voltage and current values. Consequently, a control panel should be the intermediate between dSPACE and components. Power supplies for different components are also needed that have been placed in the control panel. For this particular test bench, a control panel was designed and fabricated. The appropriate drawing can be viewed in Appendix A. The control panel requires three input voltages of 110V single-phase, 208V three-phase, 460V three-phase, and currents of 20A, 20A, and 13A, respectively. The control panel has numerous components, such as relays, motor drivers, contactors, sensors. Figure 3-27 shows four views of the control panel. The control panel's components are sorted into high voltage and low voltage and are placed on opposite sides of the control panel (high voltage components are on the far left, and low voltage components are on the far right, as shown in Figure 3-27).

Figure 3-27: Control panel.

3.4.1 DC Motor Driver

As the DC motor of the test bench is a critical component of the powertrain, it is crucial to have full control over it. To achieve this, Navitas TSX 500, a DC Motor Driver that can drive a separately-exited DC motor with a maximum armature current of 500A and a field current of 50A, is employed. The TSX 500 obtains its commands from DS2103 board to control the DC motor. With the software-called PCProbitII-148, it is possible to manage the peak current value for the field and armature. Furthermore, the software relates parameters such as the field armature voltage and the current for traction and regenerative modes. Figure 3-28 shows the DC motor driver, Figure 3-29, shows two snapshots of its software that have been used to change the driver's principle variables.

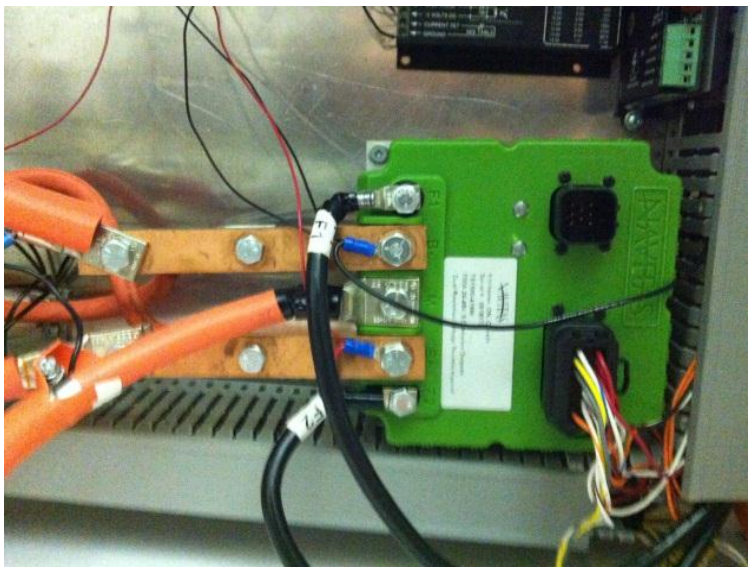

Figure 3-28: DC Motor driver.

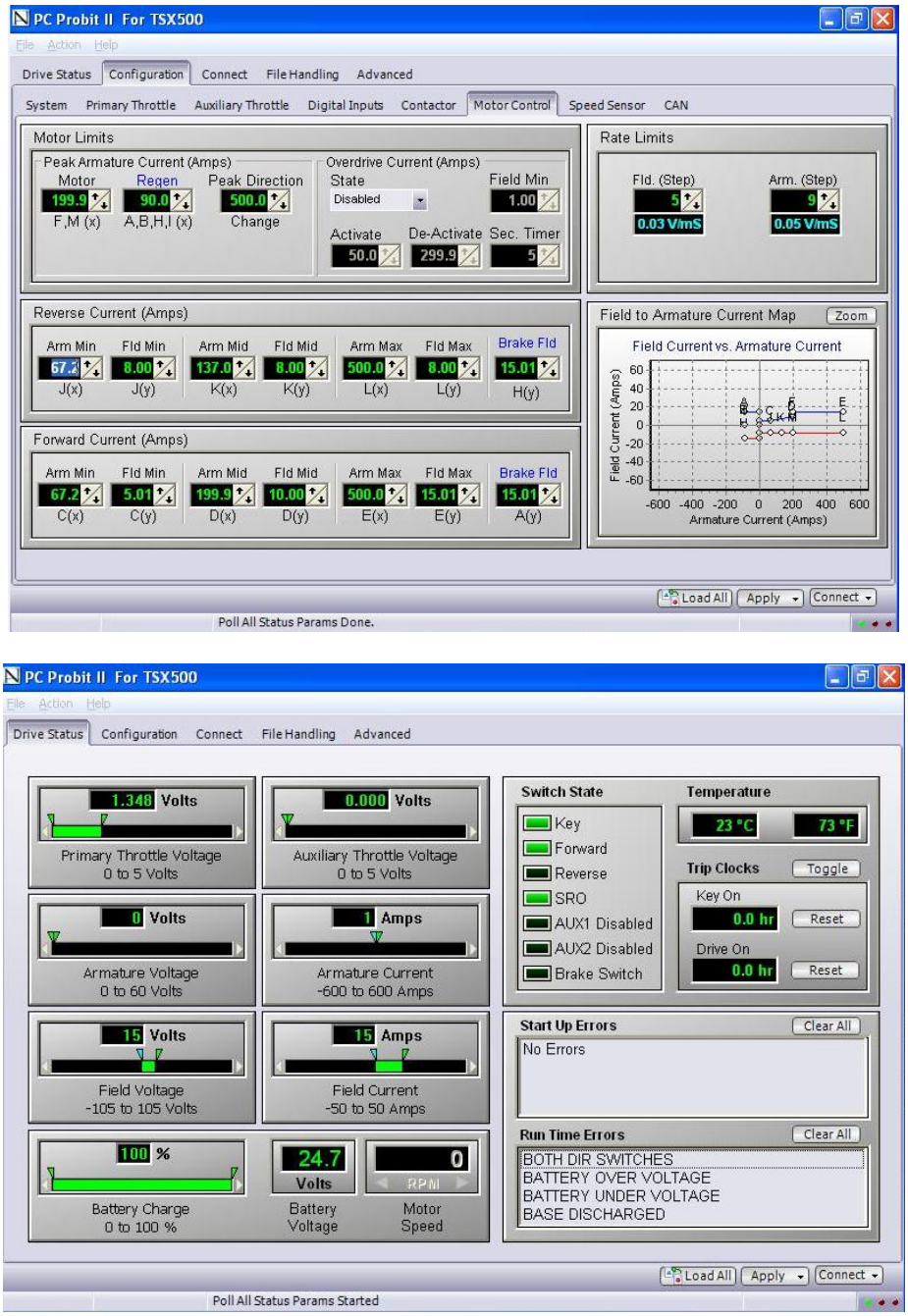

Figure 3-29: DC Motor driver software.

3.4.2 Stepper motor driver

As mentioned in Section 3.2.9 (CVT), a stepper motor, which is a type of linear actuator, has been employed to change the ratio of the CVT. As shown in Figure 3-30, a MH10 Microstep Drive has been used to drive the stepper motor. The command used for controlling the driver adjusts the speed and step parameters using a DS4004 board.

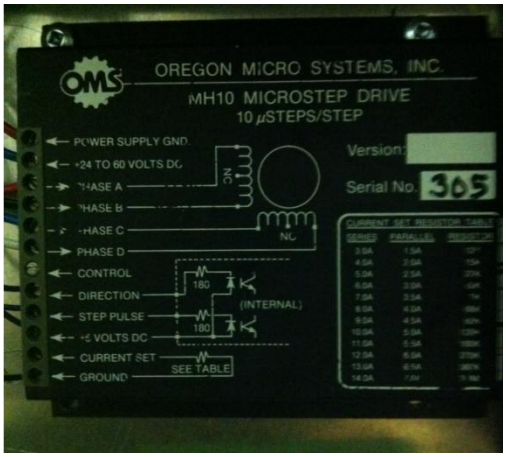

Figure 3-30: Stepper motor driver.

3.4.3 DC load driver

The DC load driver is an intermediate component between the DS2103 board and the friction brake. This component acts as a voltage controller in order to control the voltage-torque profile of the brake.

3.4.4 460 Volt motor driver

The driver used here to drive the road simulator load motor is the MX1600, as shown in Figure 3-31. This driver works with 460V AC three-phase motor. The required voltage is produced by a transformer that changes the input voltage of 208V three-phase to an output voltage of 460V three-phase.

Figure 3-31: MX 1600 driver and 460V 3 phase transformer.

3.4.5 Current sensor

In order to measure and perform real-time monitoring of a battery's current as well as the power supply and load, two transducer current sensors have been employed. As shown in Figure 3 32, each of the transducer current sensors' voltage output is related to the current flowing in the orange wire passing through the sensor's orifice. According to the manufacturer, the relationship between the voltage output of this sensor and the value of the current can be determined using:

$$I = (V_{out} - 2.5) * 100 \quad (3.5)$$

The sensor has a +/- 1% accuracy [38]. To obtain better accuracy, the relationship of each sensor has been calibrated with an accurate current meter.

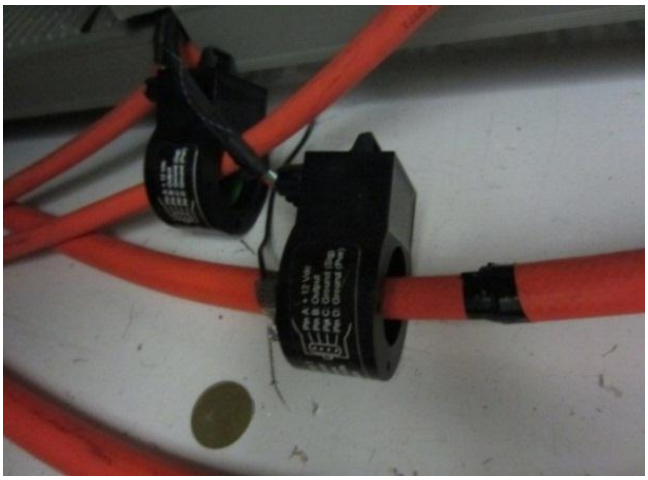

Figure 3-32: Current sensors.

3.4.6 Voltage sensor

To calculate the amount of power used or produced by the DC motor-generator, it is important to know the voltage of the electrical bus as well as the battery voltage while performing the tests. For this purpose, the voltage in real time needs to be measured. A Phidgets 1135-Precision Voltage Sensor has been employed for this reason. The factory-defined relationship between the sensor`s voltage output and the voltage measured by this sensor is given by:

$$V = (V_{out} - 2.5)/0.069 \quad (3.6)$$

The sensor has a +/- 2% accuracy. In order to obtain better accuracy, the relationship of each sensor has been calibrated with an accurate voltage meter [39]. Voltage sensors are shown in Figure 3-33.

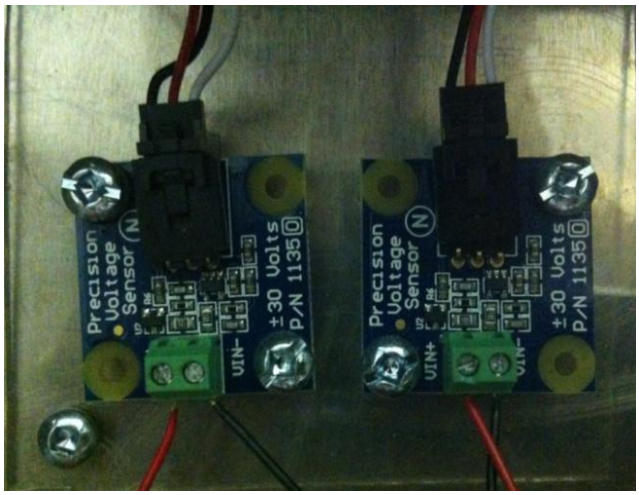

Figure 3-33: Voltage sensors.

3.5 Safety

The dangers associated with high voltage and high current as well as with moving components require considerable safety measures. These include the placement of safety relays, emergency stop switches, safety guards and appropriate gauges for wires. To obtain Canadian Standards Association (CSA) approval (which was mandated be the University of Waterloo), all electrical components were constructed in adherence to CSA guidelines. CSA approval was obtained on January 6th, 2012. Figure 3-34 illustrates the safety components and the CSA approval sticker.

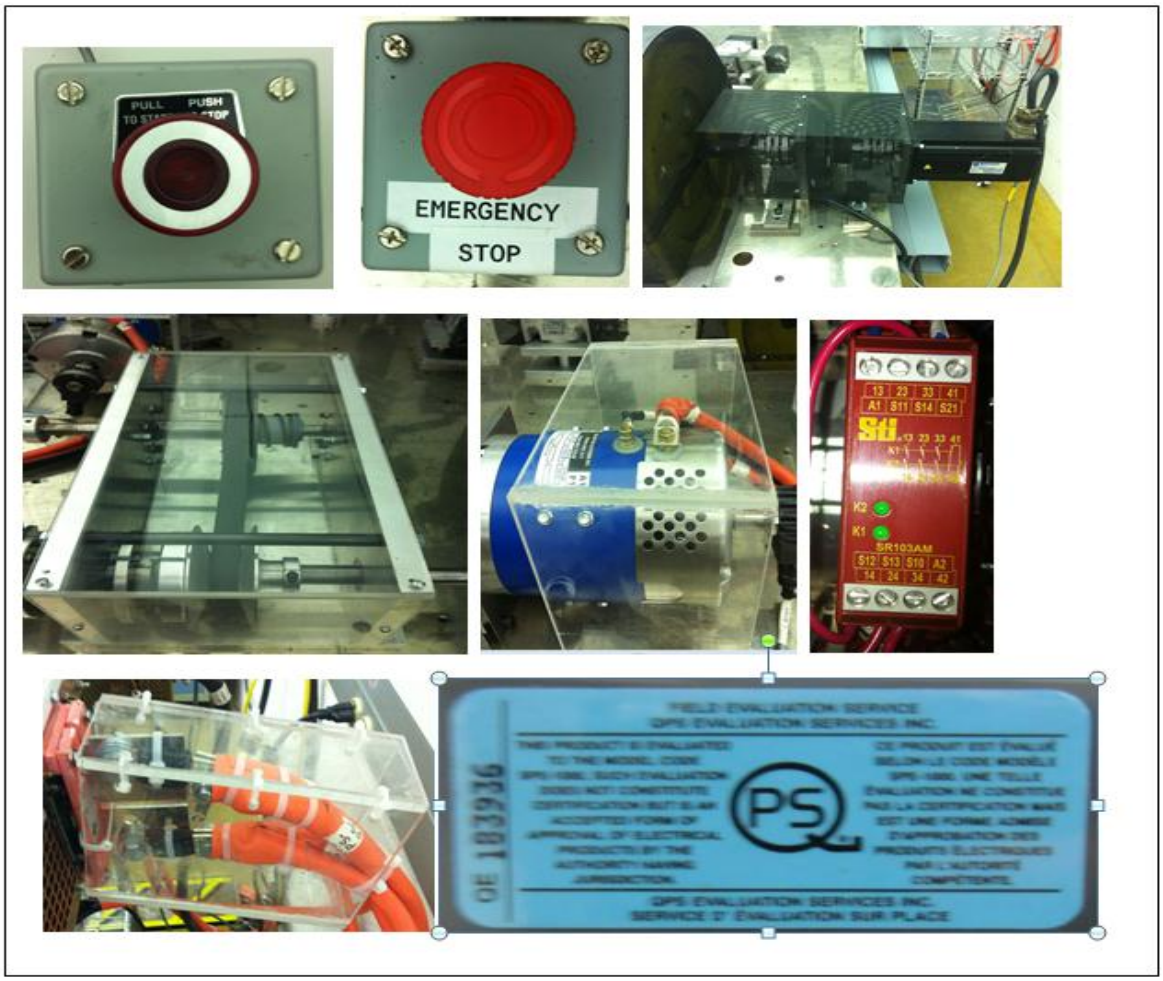

Figure 3-34: Safety components and CSA sticker.

Chapter 4 Experiment Studies and Analysis

After developing and constructing the test bench, a number of tests were conducted in order to define some of the key characteristics of the device. These tests focused on the flywheel, the DC motor, the brakes, the ICE-generator combination (for series-hybrid studies) and the batteries. As well, the Highway Fuel Economy Test (HWFET) was conducted in order to measure the amount of energy that a simulated vehicle requires to complete this standard drive test. All of these tests are described in detail below.

4.1 Flywheel

The aim of the flywheel test was to find the flywheel's damping coefficient in order to develop a flywheel model. As mentioned above, the flywheel is the component of the test bench that represents the mass of a vehicle, and the flywheel's rotational speed represents the vehicle's speed. From Newton's second law, Equation 4.1 can be used to represent the flywheel. Equation can be writhen as:

$$T = I\dot{\omega} + C\omega \tag{4.1}$$

Where T is the torque (N.m), I is the inertia, ω is the rotational speed (rad/sec), C is the damping coefficient of the flywheel and $\dot{\omega}$ is derivative of flywheel's rotational speed. ω is known quantity provided by the encoders in the test bench and $\dot{\omega}$ can be found from ω easily. Furthermore, I is a constant equal to 3.99 $\frac{Kg.m^2}{rad^2}$, as represented by the SolidWorks model of the flywheel. The only unknown variable is the damping coefficient.

To find the amount of torque (T) applied to the flywheel, it is necessary to find the damping coefficient. Knowing the damping coefficient enables one to fully develop the model representing the flywheel and to calculate the mechanical power used by the motor to speed up the flywheel. It also allows one to calculate the amount of friction exerted on the flywheel and its axels. The mechanical power to drive the flywheel is:

$$Mechanical\ power = T\omega \tag{4.2}$$

The experimental procedure involves accelerating the flywheel and turning the motor off immediately after the flywheel reaches a speed of 2000 rpm (which is equal to 210 rad/sec). Subsequently, with the motor turned off, the flywheel is left to decelerate as a result of combined damping of the flywheel, the emergency brake and the DC motor (when it is turned off). Figure 4-1 illustrates the flywheel's speed verses time during the deceleration profile.

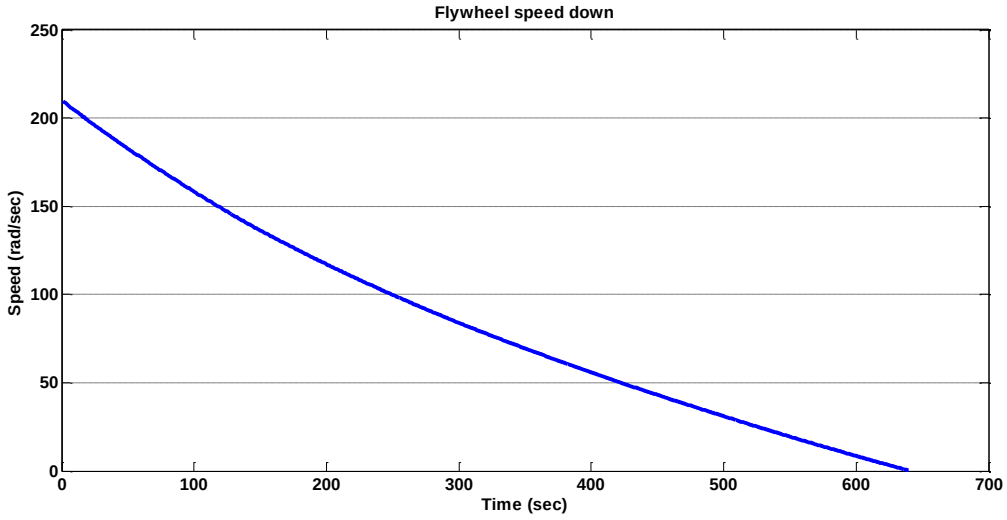

Figure 4-1: Flywheel speed down.

Considering that the motor is turned off here, no external torque is being applied. Hence, the torque (T) value is zero, and Equation (4.1) can be rearranged for the combined damping coefficient, as:

$$C = -\frac{I\dot{\omega}}{\omega} \tag{4.3}$$

Graphing the above equation for a speed range of 0 to 210 rad/sec depicts the profile of the damping coefficient shown in Figure 4-2. In order to simplify the calculations, the combined damping coefficient is considered to be a constant equal to the average value of 0.0143 for a speed range of 20 to 210 rad/sec. The reason for choosing this speed range is that these speed values are the required values for most of the tests and drive cycles.

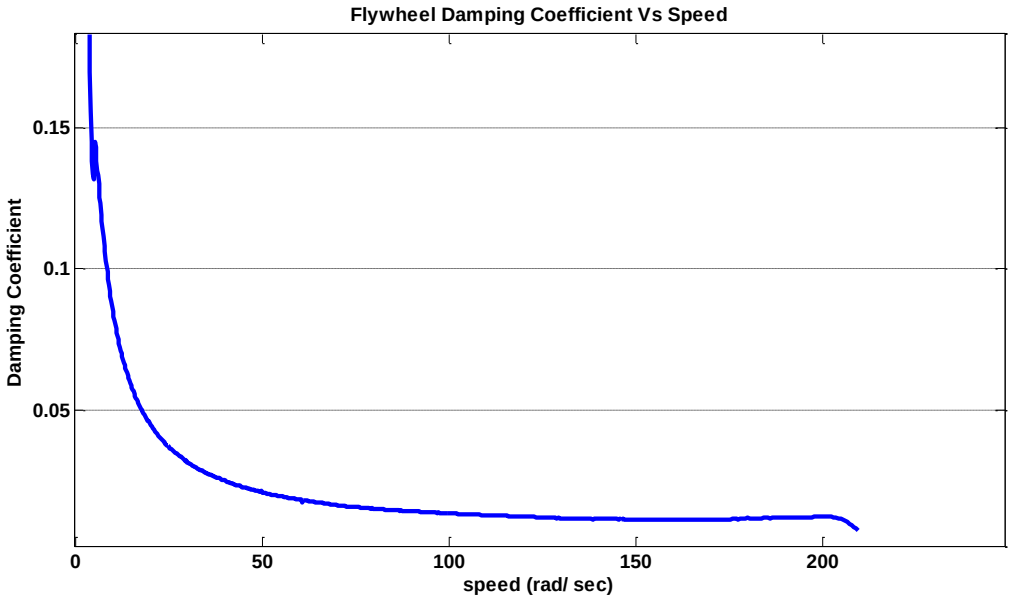

Figure 4-2: Combined damping coefficient vs. speed.

4.2 DC motor

The test conducted on the DC motor was to generate characteristic plots for its two modes of operation—the traction and generator modes. The characteristic plots include flywheel speed vs. time, torque vs. time, and power vs. time. As mentioned previously, the DC motor in the test bench plays a pivotal role. During drive cycles, when the motor decelerates the flywheel, the generator mode reverts to regenerative braking mode. In this mode, the DC motor starts generating electrical energy and charging the battery. The amount of electrical energy produced by the DC motor depends on the speed of its axel and other parameters such as the field and the armature currents. These values can be set in the PC Probit II for TX500 software.

Figure 4-3 shows the initial values set for the DC Motor Driver. As shown, the values for the maximum armature current and the field current for traction modes are 200 and 15, respectively. For the regenerative mode, the values for the armature current and brake field are 90 and a constant 15, respectively. These parameters are directly related to the power of the motor in both modes. The greater the current is, the greater the power will be.

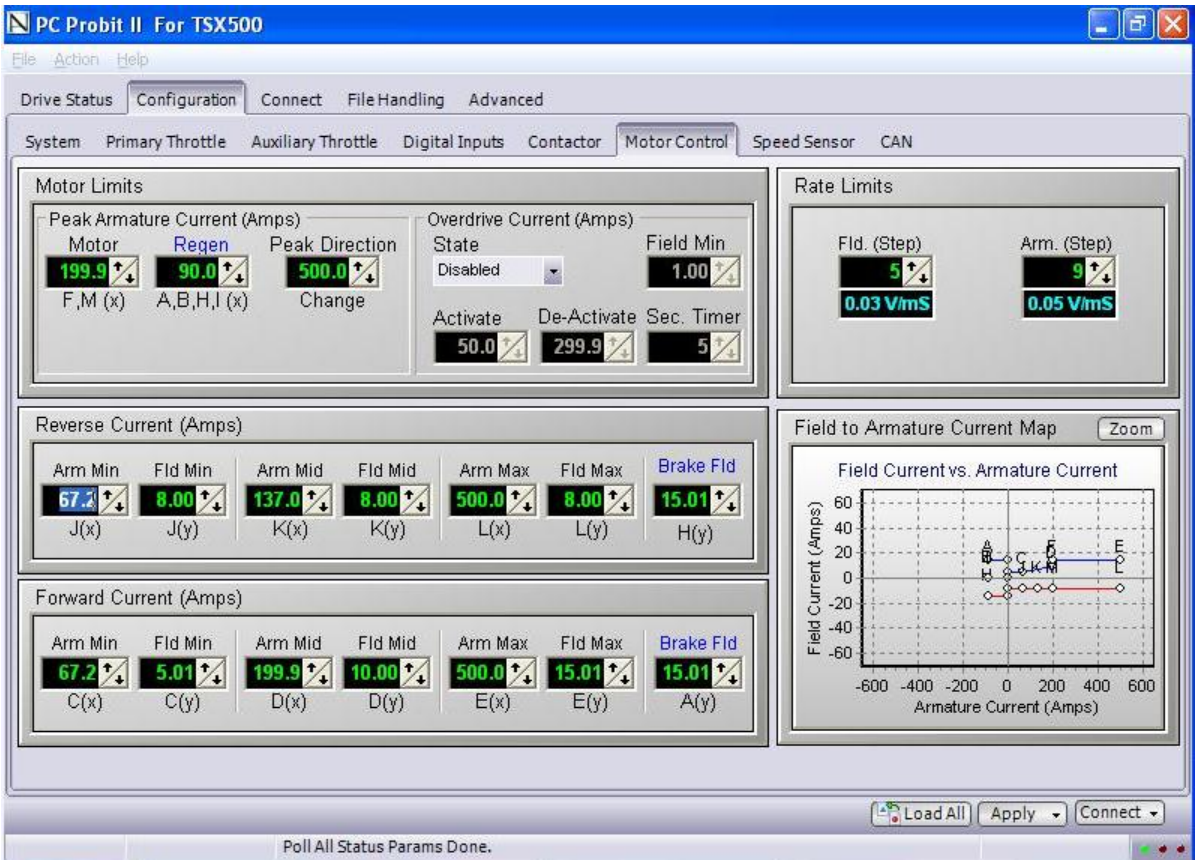

Figure 4-3: DC Motor generator driver's initial values.

Figure 4-4 shows the flywheel speed vs. time profile for motor traction and regenerative modes. In this test, the motor was connected to the flywheel, after which the speed was increased to 1600rpm (169 rad/sec) and then reduced to 0 in the regenerative braking mode. Obtaining the speed profile is the first step in finding the amount of power used for this test, as explained below.

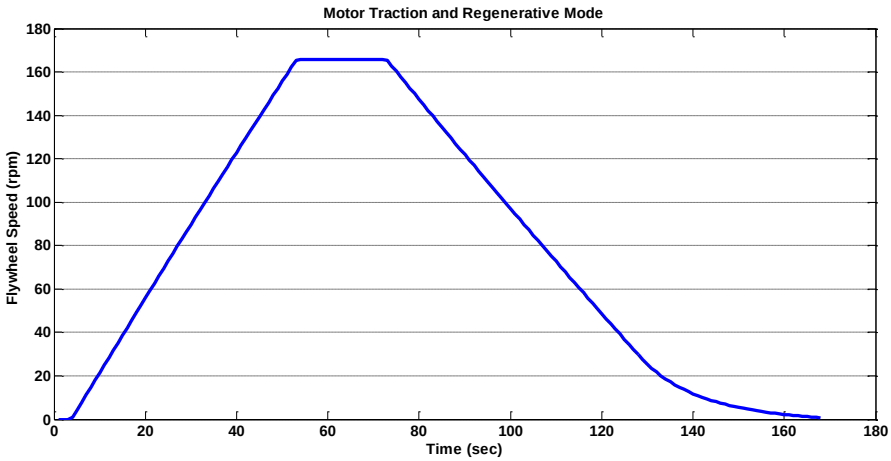

Figure 4-4: DC Motor traction and regenerative mode, speed vs. time.

Having obtained the speed profile, Equation (4.1) can be used to generate the torque profile of the motor pertaining to this test, as shown in Figure 4-5. As previously discussed, all parameters are known in this equation and the damping coefficient (C) of the flywheel was obtained by the flywheel test. As it is clear in the figure, when the mode switches to regenerative braking, the motor starts converting mechanical power to electrical power, resulting in the motor producing a negative torque in order to decelerate the flywheel. Figure 0-1 and Figure 0-5 in the Appendix show the battery voltage and the current in this test. Figure 4-6 illustrates the test's electrical and the mechanical power. The result is that the DC motor and driver can convert 70% of electrical energy to mechanical energy in the traction mode and convert 50% of the mechanical energy to electrical energy in regenerative mode in order to charge the batteries.

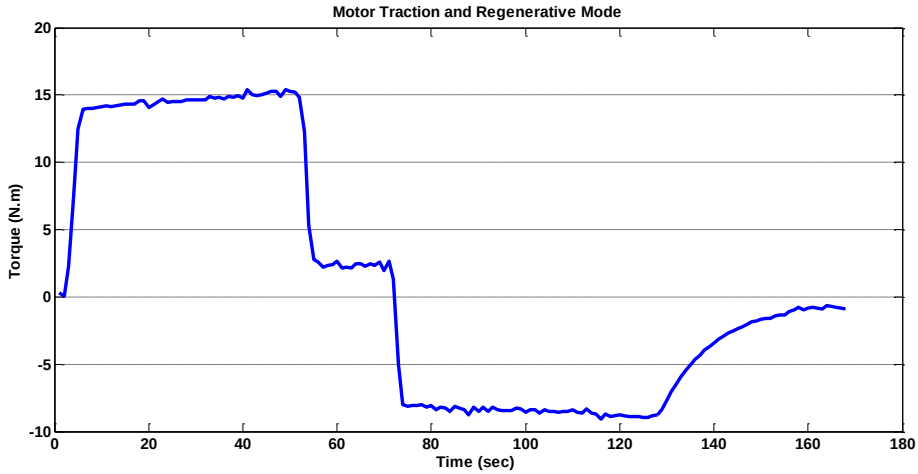

Figure 4-5: DC Motor traction and regenerative mode, mechanical torque produced vs. time.

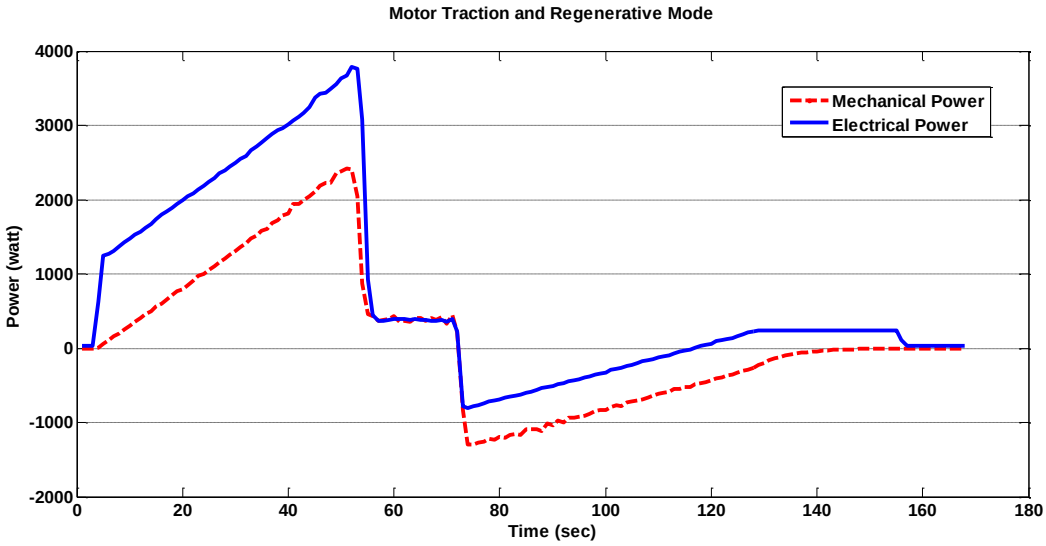

Figure 4-6: DC motor traction and regenerative mode electrical and mechanical power vs. time.

4.3 Brakes

To obtain a better understanding of the emergency brake performance, a test was conducted to create a profile. Figure 4-7 shows the performance of the emergency brake when it is actively stopping the flywheel from a speed of 2000 rpm. The flywheel fully stops in 4.9 seconds. The average torque produced by the emergency brake can be calculated using Equation (4.1). The calculated average torque is about -170 N.m.

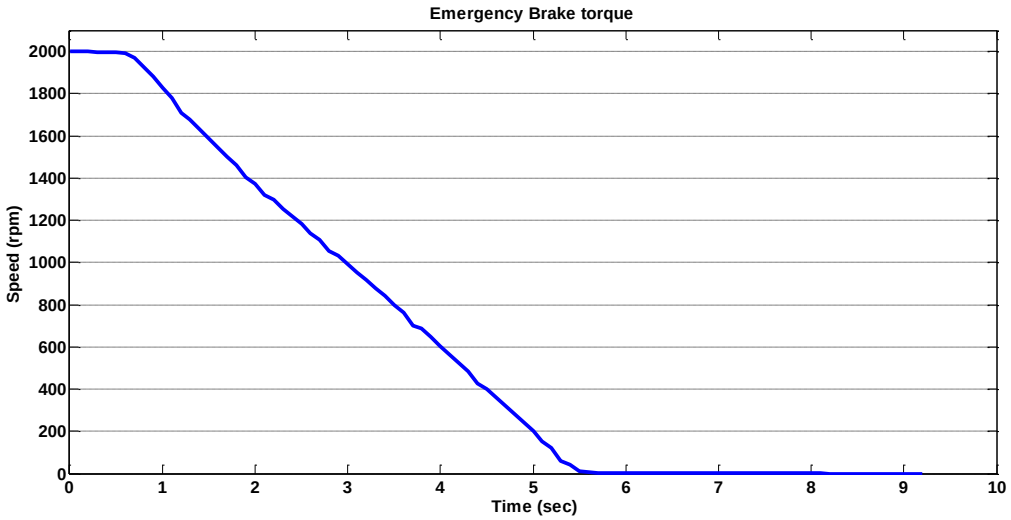

Figure 4-7: Emergency brake performance.

As mentioned above, one of the power train components is a friction brake. The friction brake of the test bench is controllable by an applied voltage. To characterize the friction brake and find its Torque-Speed-Voltage profile, a test was conducted. This test involved the installation of the friction brake between the DC motor and the flywheel. Initially, the motor increased the speed of the flywheel to 200 rad/sec, after which the motor was turned off and the friction brake activated. Figure 4-8 shows the resulting speed reduction from 200 rad/sec to zero when the applied voltage to the friction brake is 16V. In order to attain a complete torque-speed profile of the voltage controllable friction brake, the test was repeated for other applied voltages ranging from 2V to 24V, as shown in Figure 4-9. Figure 4-10 shows the MATLAB Simulink block of the friction brake.

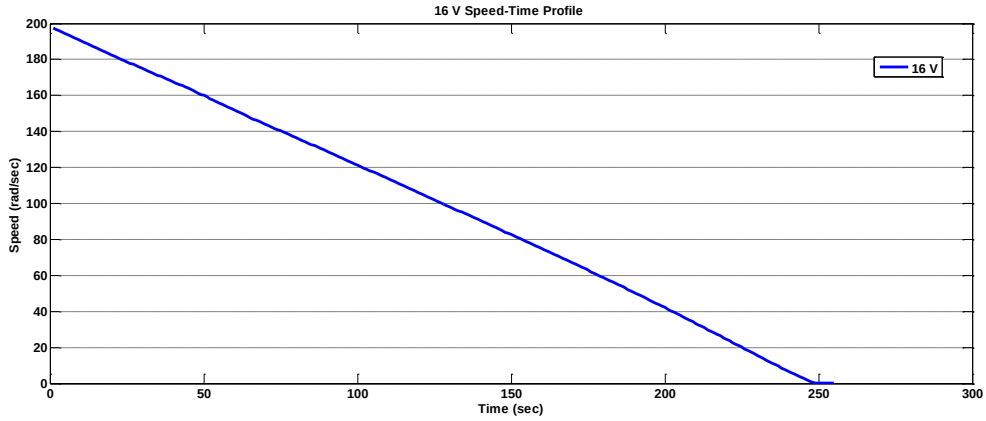

Figure 4-8: Influence of 16V friction brake on flywheel speed.

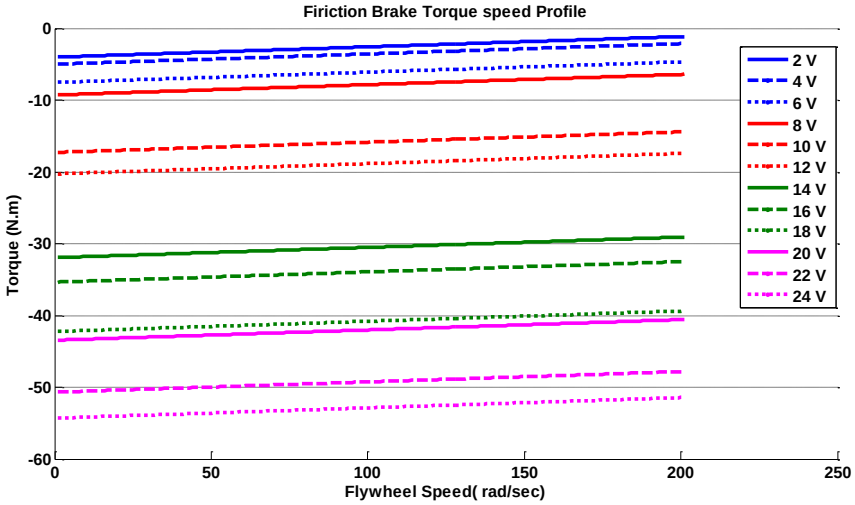

Figure 4-9: Friction brake torque-speed profile for different voltages.

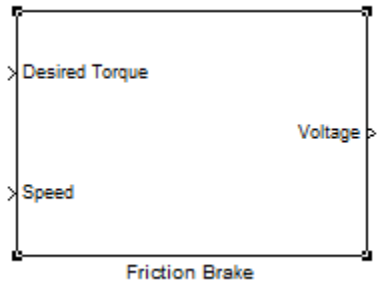

Figure 4-10: Friction brake MATLAB Simulink block.

4.4 Internal Combustion Engine and Generator

There are two power trains in the series configuration of HEV: the electric motor and the battery, and the ICE and the generator. In order to use the test bench for the series HEV studies, the ICE-generator powertrain must first be explored. Figure 4-11 shows how the ICE and the generator are connected to each other. As mentioned in Section 3.2.2, in order to turn the ICE on, the motor-generator must be in traction mode. Here, the motor increases the speed of the ICE up to 2750 rpm, which is the best fuel-efficient point of the test bench ICE [35]. This speed turns the engine on, and after a second, the motor-generator is switched to the generator mode in order to produce power. Figure A-0-3, shows the working speed of the ICE + Generator, while Figure 0-4 and Figure 0-5 in the Appendix show the produced electrical voltage and current, respectively.

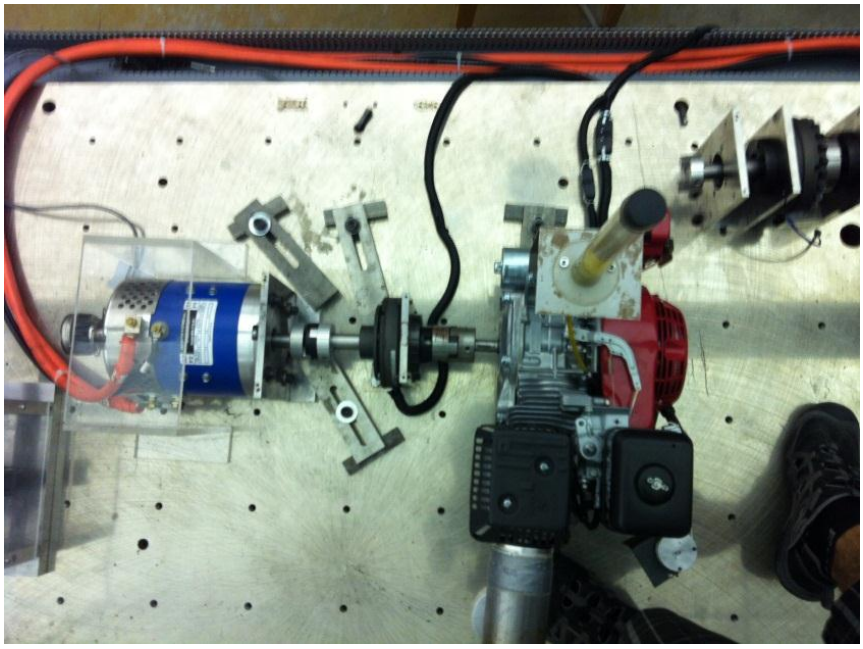

Figure 4-11: ICE + Generator.

The ICE uses 10 ml of 87 octane petrol within 25 seconds, and the generator produces 40.321 kJ of electrical energy, storing it in the battery. The fuel consumption per second is equal to 0.4 ml;, with the energy generated per second being equal to 1.694 kJ. Figure 4-12 shows the produced electrical power versus time.

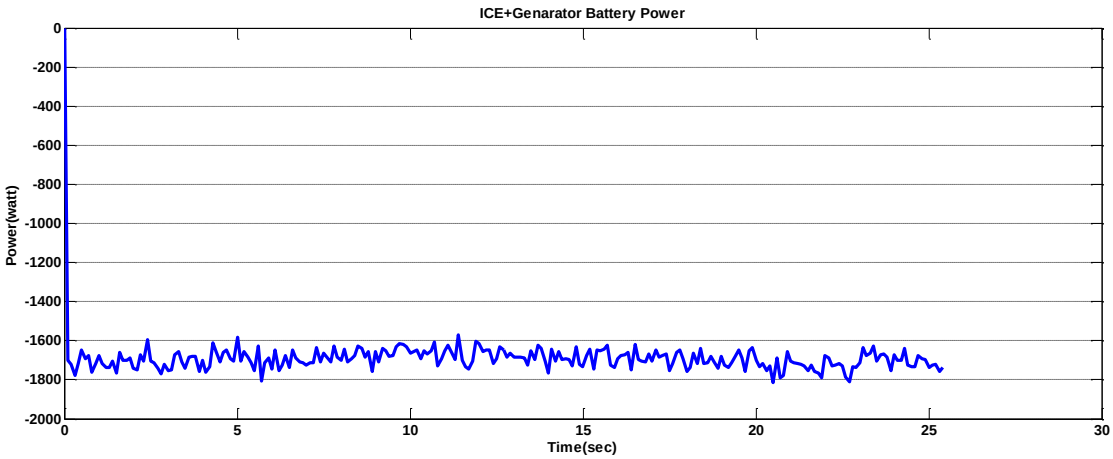

Figure 4-12: ICE + Generator-produced electrical power.

4.5 Battery

In this section, the lead-acid battery employed in the test bench is characterized by measuring some of its key parameters, such as internal resistance, columbic efficiency (η), charging capacity, discharging capacity, and open circuit voltages. These parameters were used to derive a model for the battery which could be used for scale-up purposes.

4.5.1 Measurements

In order to find the battery capacity, the lead-acid battery was first fully discharged, after which the power supply fully charged the battery with a constant voltage. By tracking the current and the time elapsed during the test, the battery's charging capacity can be calculated using:

$$Battery\ capacity\ [Ahr]\ =\ Current\ [Amper]\ *\ Time\ [Hours] \qquad (4.4)$$

Figure 0-6 shows the battery charging profile versus time.

The charging capacity was calculated to be 86.3 Ahr. Using the same equation for discharging the battery, the discharging capacity was calculated to be 70 Ahr.

Substituting the total energy used to charge and the total energy discharged from the battery into Equation (4.5), the columbic turnaround efficiency is calculated to be 81%.

$$\eta_{\text{coulombic}} = \frac{\int I_{\text{out}}\, dt}{\int I_{\text{in}}\, dt} = 81\% \tag{4.5}$$

In order to find the internal resistance of the battery during charging and discharging for all of the battery's states of charge (SOC), the Hybrid Pulse Power Characterization (HPPC) [40] test was conducted. The applied current was equal to 2.5 times the discharging capacity (C):

$$2.5C = 2.5(70) = 175\ Amps \tag{4.6}$$

The current applied here is equal to 175 amps for the battery. Figure 4-13 shows the results of the HPPC test. As illustrated, the battery discharges for 10 seconds at the applied current, followed by a 40-second rest period. Subsequently, the battery charges with 75% of the applied current for 10 seconds.

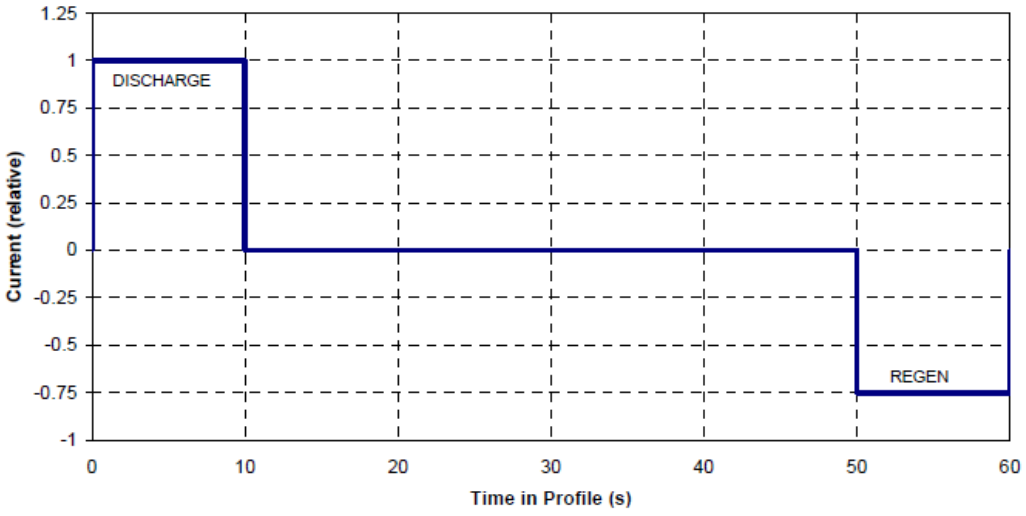

Figure 4-13: Hybrid pulse power characterization test profile [40].

Figure 4-14 shows the complete sequence of the HPPC test. The first step in this test is the full discharging of the battery, followed by an hour rest. The charging cycle is then started, followed by another one-hour rest. The second step involves discharging 10% of the battery at a current rate of C/1. This corresponds to the battery used for the test bench, where the discharging capacity is 70Ahr and the rate of discharging is 70 amps. Thus, to discharge 10% of the battery, discharging is continued for 6 minutes. After one hour of rest, the battery is subjected to the HPPC Profile Test with high current discharging and charging (as mentioned above). This process is repeated until the battery is fully discharged. The data generated by this procedure is required to obtain the battery's internal resistance for charging and discharging at a certain SOC.

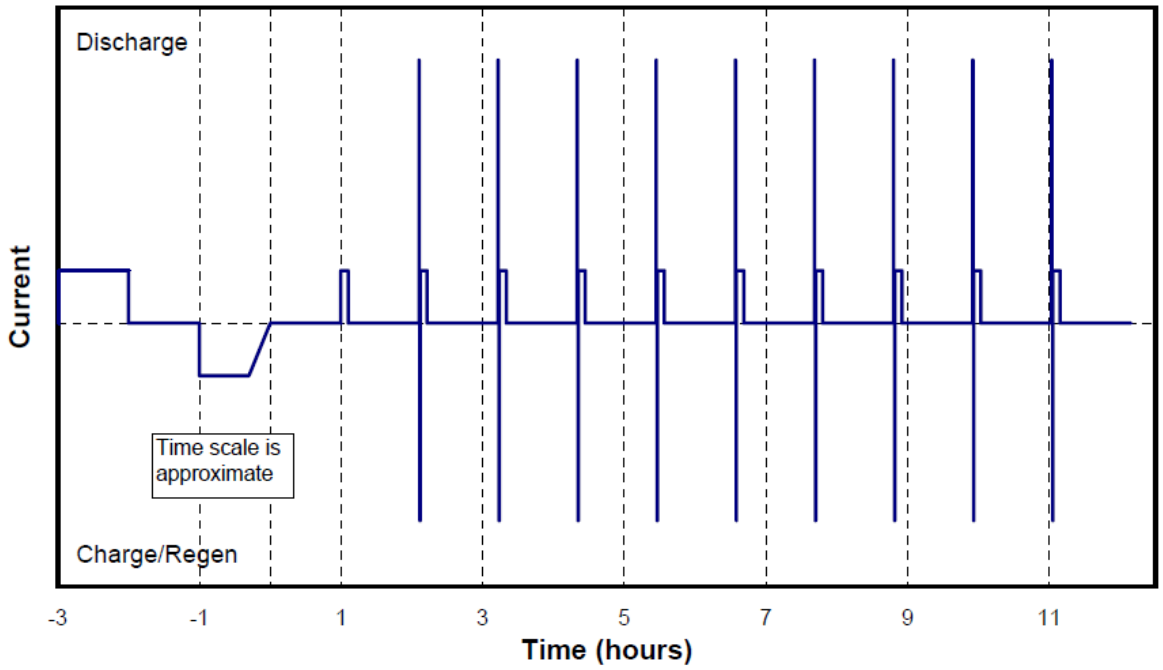

Figure 4-14: Hybrid Pulse Power Characterization Test (Complete HPPC Sequence) [40].

Figure 4-15 shows the HPPC discharging and charging profile at 80% SOC. To calculate the internal resistance, Equations 4.7 and 4.8 [40] have been used. The change in voltage and current between

points 1 and 2 for discharging and points 3 and 4 for charging resistance at a given SOC are required for these calculations.

$$R_{int-discharge} = \frac{\Delta\, Voltage\ (1\ to\ 2)}{\Delta\, Current\ (1\ to\ 2)} \tag{4.7}$$

$$R_{int-charge} = \frac{\Delta\, Voltage\ (3\ to\ 4)}{\Delta\, Current\ (3\ to\ 4)} \tag{4.8}$$

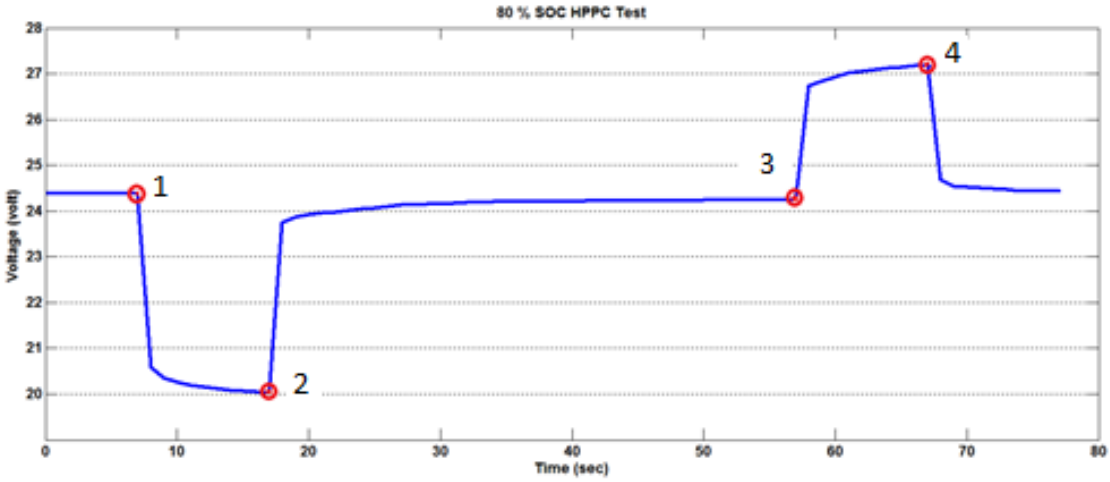

Figure 4-15: 80% SOC HPPC profile test results.

Using Equations (4.7) and (4.8), the graphs shown in Figure 4-16 and Figure 4-17 are obtained which represents a lead-acid battery's internal resistance to discharging and charging process, respectively.

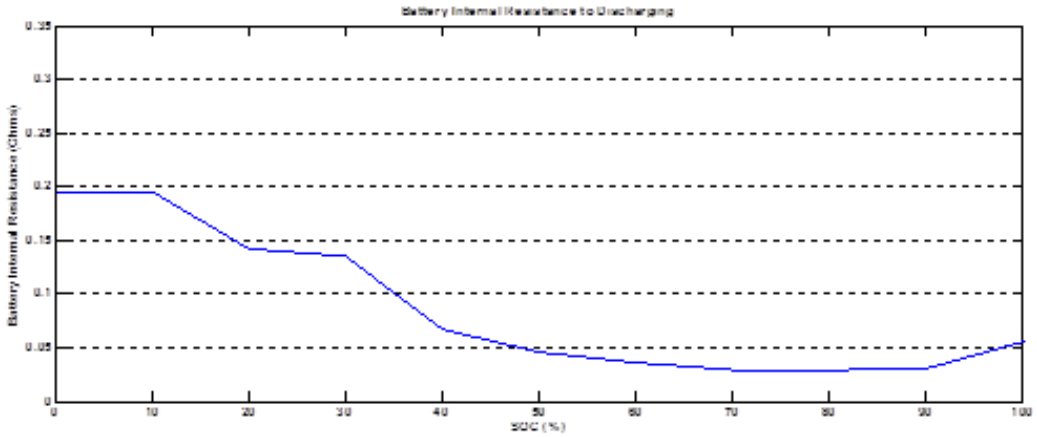

Figure 4-16: Lead-acid battery's internal resistance to discharging.

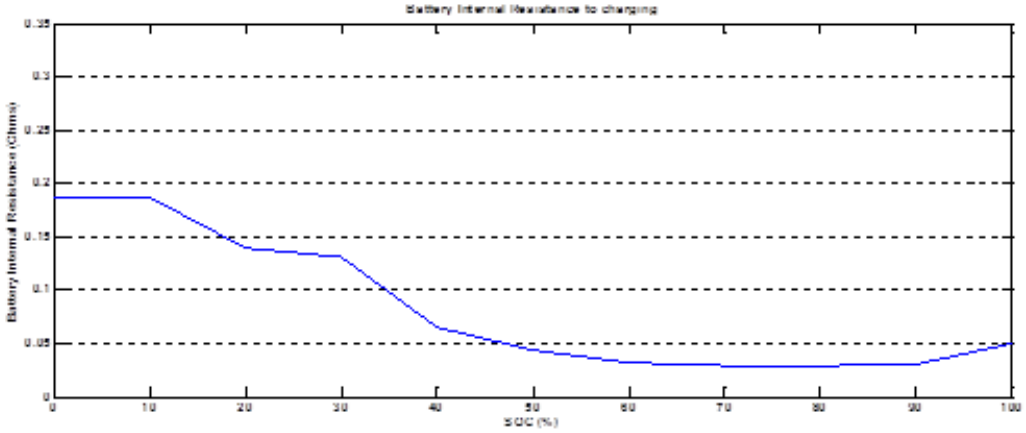

Figure 4-17: Lead-acid battery's internal resistance to charging.

In the HPPC testing, the battery's voltage was recorded during the last minutes of the one-hour rest periods. Subsequently, the Open-Circuit Voltage vs. SOC map was generated using the voltage values obtained and the corresponding SOC values, as shown in Figure 4-18.

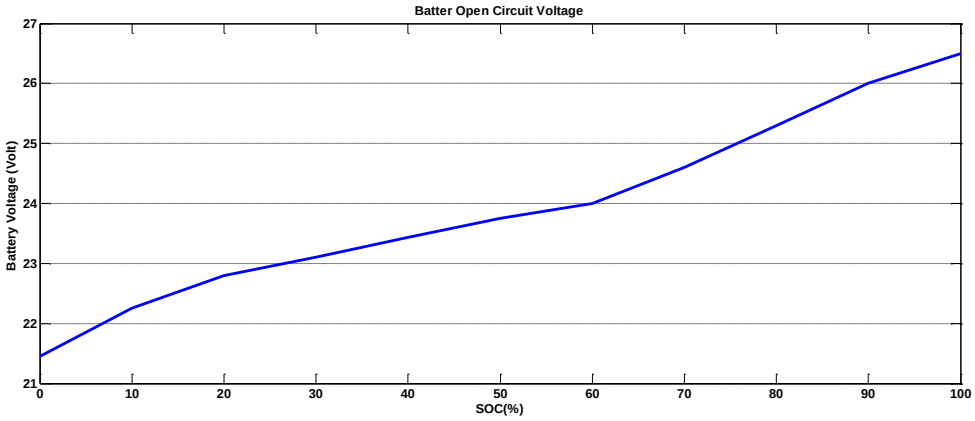

Figure 4-18: Lead-acid battery's open circuit voltage.

4.5.2 Signal scaling using Buckingham's Pi Theorem

To obtain acceptable results, a meaningful scaling is required when simulating a full-sized system with a smaller prototype. Dimensional analysis must be used in order to relate phenomena that are different in size but behave similarly to each other. For the batteries in this project, scaling has been used at the inputs and outputs of the battery cycler. In order to map two systems that follow the same principle with different parameter values, Buckingham's Pi Theorem can be used. The Pi Theorem states: "If an equation in n arguments is dimensionally homogeneous with respect to m fundamental units, it can be expressed as a relation between $n - m$ independent dimensionless arguments" [41].

Seven parameters are important for analyzing batteries. These parameters are the battery's state of charge (SOC), power (P), voltage (V), current (I), capacity (Q), equivalent series resistance (R), and characteristic time (T). The output of the system is considered to be the battery's state of charge, which is a dimensionless parameter. Thus, the state of charge of the two systems will be the same as long as the other dimensionless groups of the system are the same.

As the input to the battery cycler, the battery's power needs to be scaled properly. A dimensional analysis' aim would be to identify the scaling factor for the battery's power. All of the parameters mentioned above can be written as a function of the four fundamental units: mass (M), time (T), length (L), and current (A), as shown in Table 4-1.

Parameter	Dimension
V	$[M][L]^2[T]^{-3}[A]$
I	$[A]$
P	$[M][L]^2[T]^{-3}$
T	$[T]$
R	$[M][L]^2[T]^{-3}[A]^{-2}$
Q	$[A][T]$

Table 4-1: Important parameter in battery analysis.

It is important to note that the dimensional bundles of $[M][L]^2$ always appear together and thus can be considered as a fundamental unit also [T] and [A] are the other fundamental units . This is why the Pi Theorem states that a battery can be presented by $6 - 3 = 3$ dimensionless groups. The rest of the parameters are shown in dimensionless groups, as presented in Table 4-2.

Dimensionless group	Parameter	Relation
π_1	Voltage	$\frac{P}{VI}$
π_2	capacity	$\frac{It}{Q}$
π_3	resistance	$\frac{RI^2}{P}$

Table 4-2: Group of dimensionless parameters in battery analysis.

In this experimental setup, the full battery pack is represented by a few battery cells. Here, the characteristic time would be considered as the discharge time, which is related to the battery's

capacity and power. Expecting the test-bench battery (TB) and the vehicle's battery (VB) to behave the same, the following relations must be satisfied:

$$\pi_{1VB} = \pi_{1TB} \tag{4.9}$$

$$\pi_{2VB} = \pi_{2TB} \tag{4.10}$$

$$\pi_{3VB} = \pi_{3TB} \tag{4.11}$$

This leads to:

$$\left[\frac{P}{VI}\right]_{VB} = \left[\frac{P}{VI}\right]_{TB} \tag{4.12}$$

$$\left[\frac{It}{Q}\right]_{VB} = \left[\frac{It}{Q}\right]_{TB} \tag{4.13}$$

$$\left[\frac{RI^2}{P}\right]_{VB} = \left[\frac{RI^2}{P}\right]_{TB} \tag{4.14}$$

Combining Equations (4.12) to (4.14) would lead to the following relation which shows the relationship between the powers of the vehicle's battery and the desired scaled-down battery of the test bench.

$$\frac{P_{TB}}{P_{VB}} = \frac{V_{TB}}{V_{VB}} . \frac{Q_{TB}}{Q_{VB}} \tag{4.15}$$

By scaling the power, the SOC of the battery can be scaled as well.

Now having characterized the various components of the test bench, the next step is to evaluate their performance using a standard drive cycle.

4.6 HWFET drive cycle

This section describes the evaluation of the fabricated test bench using a standard drive-cycle. There are many standard drive-cycles available which are used worldwide. These tests are directed at evaluating the performance of the all the components of the test setup including the flywheel, the batteries, ICE, and the DC motor. In this test, the standard highway drive cycle developed by the US Environmental Protection Agency (EPA) is used and the results of this drive cycle on the test bench are presented. Figure 4-19 shows the HWFET, with the vehicle's speed in mph. The conversion method has been described in Section 3.2.4. By converting the unit to rad/sec and giving it as an input to the DC motor, the speed controller tried to track the drive cycle. Figure 4-20 illustrates flywheel speed and desired speed.

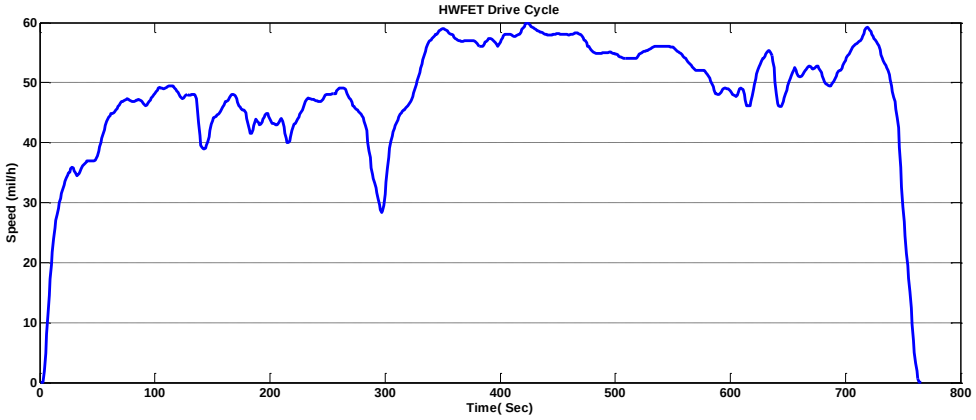

Figure 4-19: Standard EPA HWFET highway cycle [42].

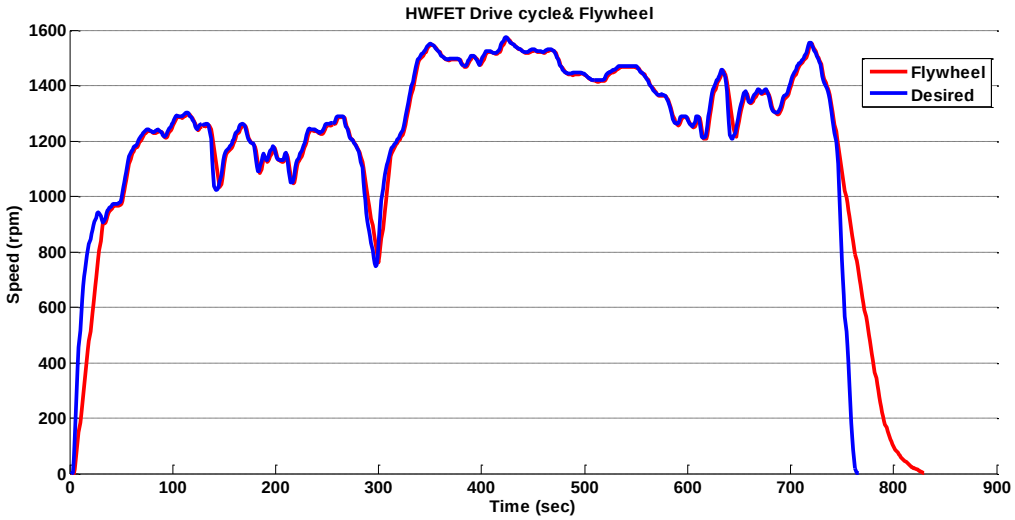

Figure 4-20: HWFET drive cycle and flywheel.

As the speed increases, the DC motor is in traction mode and uses electrical power. Hence, the battery's electrical power is positive, its voltage decreases, and its current is positive. When the speed needs to decrease, the DC motor is switched to regenerative mode and starts generating electrical power which is stored in the battery. Consequently, the battery's voltage increases, and its current and electrical power are negative. Figure 4-21, Figure 4-22, and Figure 4-23 show HWFET-battery voltage, current, and power, respectively. As it was mentioned before the DC motor PID controller generates appropriate signal for DC motor driver in order to follow the drive cycle. The MATLAB Simulink snapshots are provided in Appendix G.

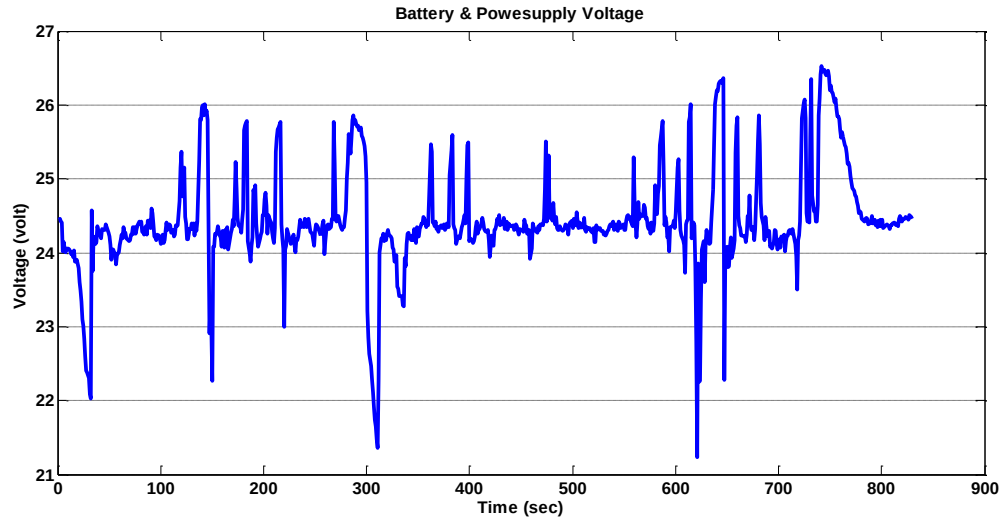

Figure 4-21: HWFET-battery voltage.

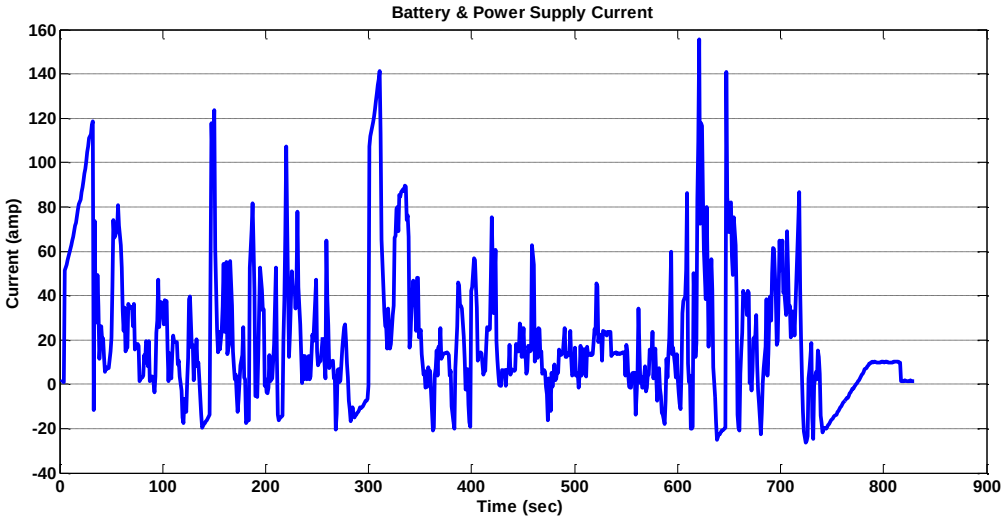

Figure 4-22: HWFET-battery current.

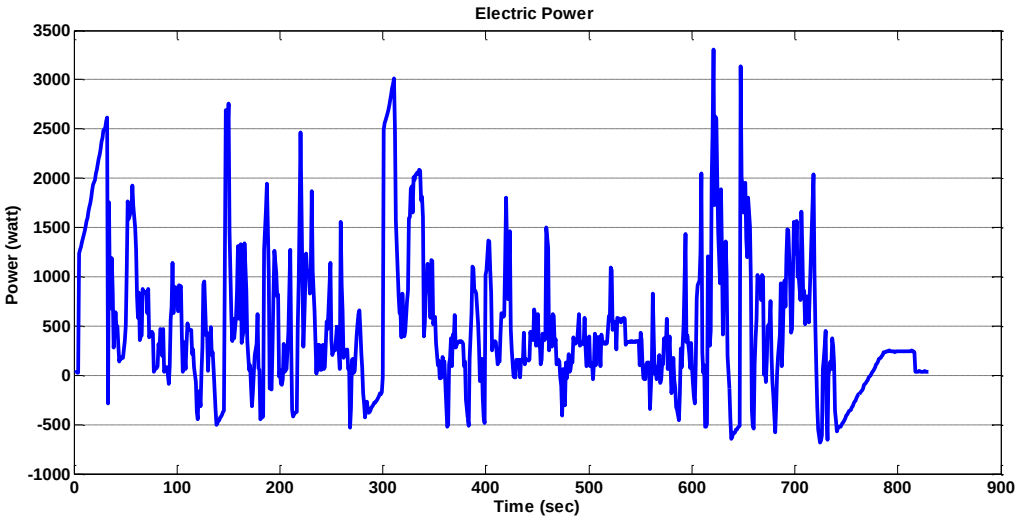

Figure 4-23: HWFET-electrical power.

Figure 4-24 shows the battery's state of charge during the HWFET drive cycle. The SOC was obtained from:

$$SOC = \frac{Capacity_{max} - Capacity_{used}}{Capacity_{max}}$$

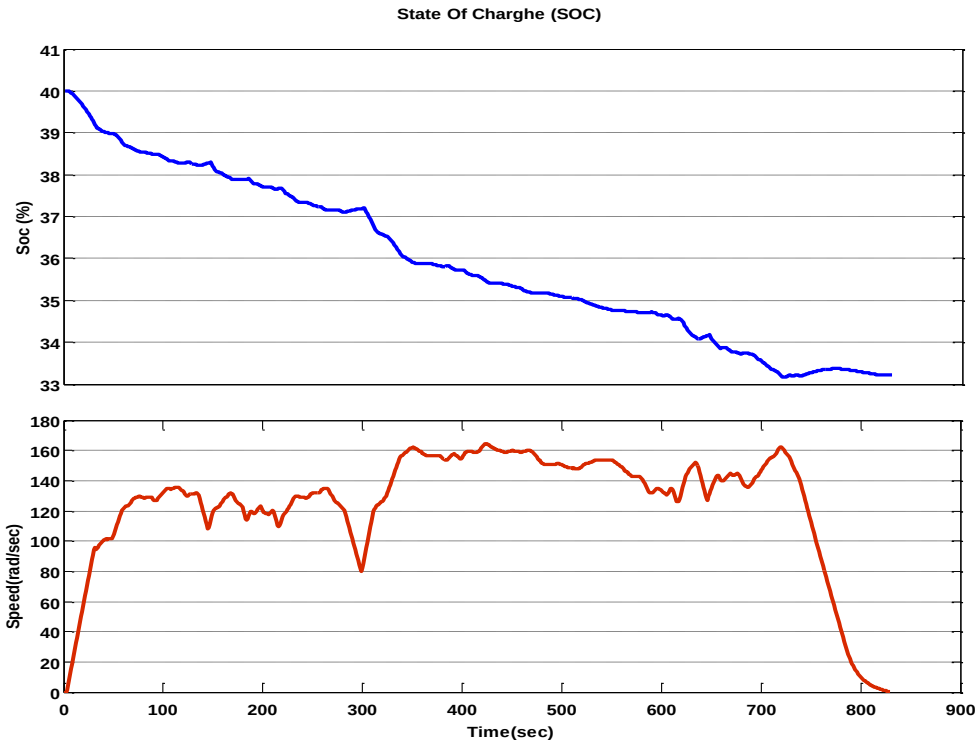

Figure 4-24: HWFET-battery SOC.

Note that with a battery capacity of 70Ahr, the battery's SOC is only dropping from 40% to almost 33% during the drive cycle. This shows that the amount of electrical energy used in this drive cycle is much smaller than the battery capacity. The aim here is to evaluate the ICE + Generator in a HEV series configuration. Evaluating the ICE + Generator however, requires a higher change in SOC in order to see the full extent of ICE + Generator interactions. In order to achieve a higher change in SOC an assumption was made that the battery's capacity is 4.3Ahr instead of 70Ahr, keeping the voltage constant. Under this assumption, the calculated SOC will be less than zero at the end of the drive cycle, as shown in Figure 4-25. The series HEV controller in the test bench turns on the ICE + Generator when the SOC is below 40%, and turns it off when it is above 60%. Figure 4-26 presents the SOC for the assumed battery when the ICE is turned on during the HWFET drive cycle. The total time that the ICE is turned on is 300 seconds. During these 300 seconds, 120ml of petrol has been used and 484kJ of energy is stored in the battery.

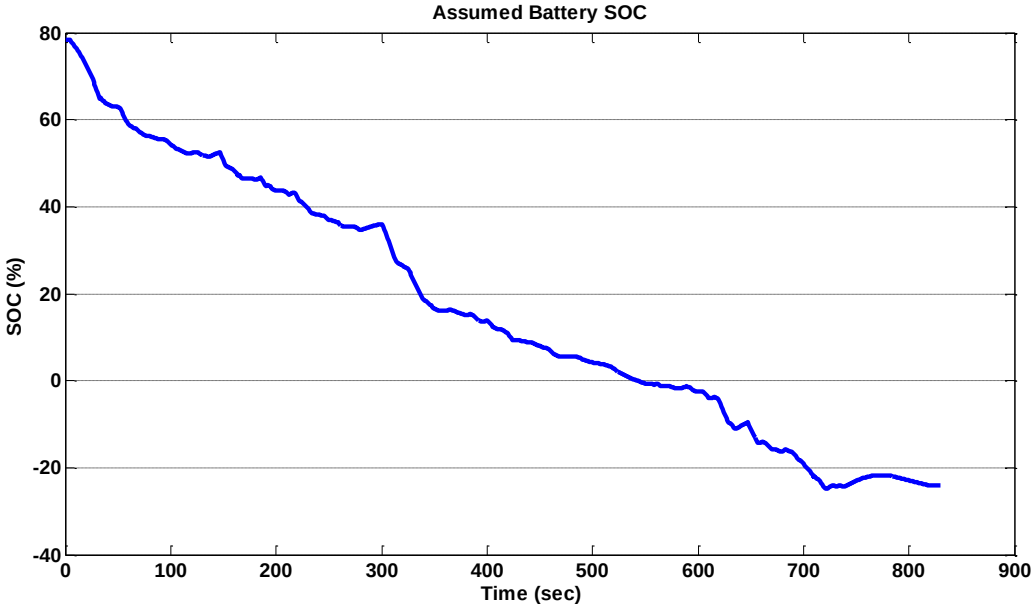

Figure 4-25: HWFET - Assumed battery SOC.

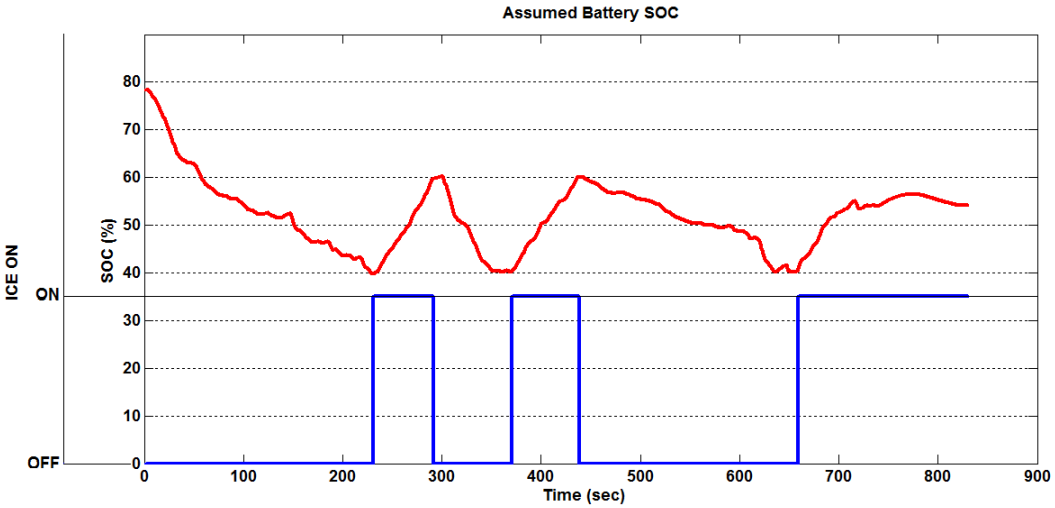

Figure 4-26: HWFET - Assumed battery SOC and ICE + Generator.

4.7 Summary

In this chapter, some tests were conducted in order to characterize the key components of the test bench as well as evaluating the test bench using a standard test. First, the flywheel's damping coefficient was found to be 0.0143 in average for a speed range of 20 to 210 rad/sec. This value was obtained from the speed-time profile of the flywheel on which no external torque (such as from a DC motor or brakes) was applied. In the next test, the characteristic plots of the traction and regenerative modes of the DC motor were generated and the efficiencies of both modes were shown. As well, the torque produced by the emergency brake was obtained when the flywheel went from a speed of 2000rpm to a full stop. The friction brake's torque-speed profile was presented for various voltages and a computer model was developed. Additionally, for the series HEV, the combination of ICE + Generator was tested to show the fuel consumption rate and the electrical power rate generated and stored in the battery.

In the battery section, the standard HPPC profile was applied to investigate the battery's characteristics, such as its internal resistance to discharge and charge. Also, the battery's open circuit voltage was found for different SOCs. Finally, a signal scaling was done to ascertain the battery's power, and Buckingham's Pi Theorem was used so that the relationships between the battery's SOC and an HEV battery could be found. At the end of the chapter, the standard HWFET drive cycle was used as an input to the system in order to determine the values of a battery's voltage, current, power, and SOC. To involve the role of ICE + Generator, the battery capacity was assumed to be 4.3 Ahr. Following this, the new SOC was demonstrated

Chapter 5 Conclusions and Future Work

5.1 Summary and Thesis Contributions

In this thesis a modular test bench for HIL testing and scaled down testing of HEVs and EVs was designed, fabricated and evaluated in one standard drive cycle. The test bench includes all the essential components of an HEV's and EV's powertrain, allowing various experimental studies to be conducted. This test bench is composed of four major components: the test bench workspace, the control panel, electrical energy storage, and the controller. The workspace is a table top with a matrix of tapped holes, designed to allow flexibility in placement of various components. There are nine components available for placement on this test bench: the flywheel, DC motor-generator, ICE, emergency brake, friction brake, CVT, road-load simulator motor, clutch, and the gearbox. The electrical energy storage is composed of two lead-acid batteries, one lithium ion battery, a power supply and an electrical load. The control panel is designed for the purpose of controlling various components and containing all of the relevant circuitry/electrical components, such as motor drivers, essential contactors, and sensors. The controller is a dSPACE RTI-1006 that is equipped with electrical boards such as the ADC, DAC, encoders, and digital output boards. The required programs are coded in MATLAB Simulink and then downloaded onto dSPACE. The dSPACE transfers the necessary signals to the control panel, which converts the signals to the appropriate voltage and current in order to control the components. With the aid of control desk software, it is possible to monitor and measure different variables and vary them in real-time simulations during the tests.

The completion of this project has faced many challenges. This required many safety measures to be applied, including the use of appropriate wire gages, safety relays, emergency stop button, etc. Another important challenge was the calibration of sensors such as the encoders, and various employed voltage and current sensors. Furthermore, there were many parameters that needed to be determined for the DC motor driver. These variables included the armature, and field currents. The growth rate of the armature and the field currents and voltages also needed to be determined. Determining these variables was crucial to ensuring that the motor was capable of handling the desired drive cycles.

Subsequently, a few experimental studies were done on the designed and fabricated test bench. The primary aim of these experiments was to characterize some of the test bench components. First, the flywheel's damping coefficient was obtained from the speed-time profile of the flywheel on which no

external torque (such as DC motor or any brakes) was being applied. The obtained value was 0.0143 for a speed range of 20 to 210 rad/sec. Next, the characteristic plots of the traction and regenerative modes of the DC motor were generated and the efficiencies of both modes were obtained. As well, the torque produced by the emergency brake was measured while the flywheel went from a speed of 2000 rpm to a full stop. Moreover, the friction brake's torque-speed profile was presented for different voltages and to develop a computer model.

The combination of ICE + Generator was likewise tested to show the fuel efficiency and the electrical power rate that was generated and stored in the battery for the series HEV. In the battery section, the standard HPPC profile was applied to investigate the battery's characteristics, such as its internal resistance to discharge and charge. At the same time, the open circuit voltage of the battery was found for different SOCs. Additionally, a signal scaling was performed to ascertain the battery's power, using Buckingham's Pi Theorem. This was done in order to find the relationships between the battery's SOC and an HEV battery. Finally, the standard HWFET drive cycle was used as an input to the system in order to determine the values of a battery's voltage, current, power, and SOC. To involve the role of ICE + Generator, the battery capacity was assumed to be 4.3 Ahr. Following this, the new SOC was shown by the graphs.

5.2 Future Work

Having completed the fabrication of the test bench and characterized its major variables, the test bench is now ready to conduct various hardware-in-the-loop studies on HEVs. For future work, it is that a planetary gear be added as a power/torque split to the components of the system in order to enable further testing for series-parallel configurations. It is also recommended that a torque-meter sensor be added, which would enable the full characterization of a DC motor. Additionally, to simulate external conditions more effectively, a road-load simulator motor should be used. Furthermore, in order to compare the results of the computer simulations and experiments, Powertrain System Analysis Toolkit (PSAT) software could be used. The PSAT is a very useful software developed for implementing control strategies and testing control benches or real vehicles [45]. It is highly recommended to do further studies for scaling down the HEV and EV powertrain for the various components of test bench using the Buckingham's Pi theorem. Finally, it is recommended that the flywheel be used as energy storage for heavy HEV studies, and that effectiveness comparisons be carried out by incorporating various control strategies.

Bibliography

[1] Ehsani, M., Gao, Y., & Emadi, A. "Modern electric,hybrid electric and fuel cell vehicles". (2 ed.). New York: CRC Press. 2010.

[2] P. Medisetti "REAL TIME SIMULATION AND HARDWARE-IN-LOOP TESTING OF A HYBRID ELECTRIC VEHICLE CONTROL SYSTEM" University of Akron, MASc. Thesis 2007.

[3] C.C. Chan and K.T. Chau, Modern Electric Vehicle Technology, Oxford University Press, Oxford, UK, 2001.

[4] E. H. Wakefield, "History of the Electric Automobile: Hybrid Electric Vehicles", Society of Automotive Engineers (SAE), ISBN: 0-7680-0125-0,Warrendale, PA, 1998.

[5] Y. Gao, M. Ehsani, and J. M. Miller, " Hybrid electric vehicle overview and state of the art", IEEE Int. Symp. Industrial Electronics, ISIE'05, Dubrovnik, Croatia, Jun. 20–23, 2005, mini-track on automotive control, MTAC.

[6] M. Ehsani, Y. Gao, and K. L. Butler, "Application of electrically peaking hybrid (ELPH) propulsion system to a full size passenger car with simulated design verification". IEEE Trans. Vehicular Technol., vol. 40, no. 6, Nov. 1999.

[7] B.S. Fan, "Multidisciplinary Optimization of Hybrid Electric Vehicles: Component Sizing and Power Management Logic" University of Waterloo, Ph.D. Thesis 2011.

[8] B. S Fan, "Modeling and Simulation of a Hybrid Electric Vehicle Using MATLAB/Simulink and ADAMS," University of Waterloo, Waterloo, ON, MASc Thesis 2007.

[9] J. M. Miller, "Hybrid electric vehicle propulsion system architecture of the e-CVT type," IEEE Trans. Power Electron., vol. 21, no. 3, pp. 756–767, May 2006, 2005-2416-SI.

[10] J. M. Miller, M. Ehsani, and Y. Gao, "Understanding power flows in HEV eCVT's with ultracapacitor boosting using simplorer, " in IEEE Power

[11] G. Zorpette, "The smart hybrid, " IEEE Spectr., vol. 41, no. 1, pp. 44–47,Jan. 2004.

[12] S. S. Williamson and A. Emadi, "Comparative assessment of hybrid electric and fuel cell vehicles based on comprehensive well-to-wheels efficiency analysis," IEEE Trans. Veh. Technol., vol. 54, no. 3, pp. 856–862, May 2005.

[13] S. S.Williamson, S. M. Lukic, and A. Emadi, "Comprehensive drive train efficiency analysis of hybrid electric and fuel cell vehicles based on motor controller efficiency modeling," IEEE Trans. Power Electron., vol. 21, no. 3, pp. 730–740, May 2006.

[14] S. S. Willamson, A. Emadi, and K. Rajashekara, "Comprehensive efficiency modeling of electric traction motor drives for hybrid electric vehicle propulsion applications, " IEEE Trans. Veh. Technol., vol. 56, no. 4, pp. 1561–1572, Jul. 2007.

[15] M. Amrhein and P. T. Krein, "Dynamic simulation for analysis of hybrid electric vehicle system and subsystem interactions, including power electronics, " IEEE Trans. Veh. Technol., vol. 56, no. 3, pp. 825–836, May 2005.

[16] T. Katrasnik, F. Trenc, and S. R. Opresnik, "Analysis of energy conversion efficiency in parallel and series hybrid powertrains, " IEEE Trans. Veh. Technol., vol. 56, no. 6, pp. 3649–3659, Nov. 2007.

[17] A.Emadi, "Power Electronics and Motor Drives in Electric,Hybrid Electric, and Plug-In Hybrid Electric Vehicles," in IEEE conference on TRANSACTIONS ON INDUSTRIAL ELECTRONICS, VOL. 55, NO. 6, JUNE 2008

[18] Zhang R, Alleyne AG. "Dynamic emulation using an indirect control input. " J Dyn Sys Meas Con 2005;127(1):114–24.

[19] Tor A. Johansen, Thor I. Fossen, Bjørnar Vik .," Hardware-in-the-loop Testing of DP systems." Dynamic positioning conference, November 15-16, 2005.

[20] Fathy HK, Ahlawat R, Stein JL. "Proper powertrain modeling for engine-in-the loop simulation". ASME dynamic systems and control division, Orlando (IMECE2005-81592); 2005.

[21] Fathy HK, Filipi ZS, Hagena J, Stein JL. "Review of hardware-in-the-loop simulation and its prospects in the automotive area. " In: Proceedings of the SPIE, modeling and simulation for military applications (6228:62880E); 2006.

[22] Rulka W, Pankiewicz E. "MBS approach to generate equations of motions for HiL-simulations in vehicle dynamics". Mult Sys Dyn 2005;14(3–4):367–86.

[23] Schupbach RM, Balda JC. " A versatile laboratory test bench for developing powertrains of hybrid electric vehicles". In: Proceedings of the 2002 vehicle technology conference, vol. 3; 2002. p. 1666–70.

[24] Oh SC. "Evaluation of motor characteristics for hybrid electric vehicles using the hardware in the loop concept". IEEE Trans Veh Technol 2005;54(3):817–24.

[25] Lo Bianco G, Pede G, Puccetti A, Rossi E, Mantovani G. "Vehicle testing in ENEA drive-train test facility" (SAE 2001-01-0961); 2001.

[26] Lemesˆ Z, Vath A, Hartkopf T, Mäncher H. "Dynamic fuel cell models and their application in hardware in the loop simulation". J Power Sources 2006;154(2):386–93.

[27] Vath A, Lemesˆ Z, Mäncher H, Söhn M, Nicoloso N, et al. "Dynamic modelling and hardware in the loop testing of PEMFC". J Power Sources 2006;157(2):816–27.

[28] Kittirungsi B, Fathy HK, Stein JL. "An efficient scaling methodology for dynamic models using dimensional and activity analyses". In: Proceedings of the 2006 ASME international mechanical engineering congress and exposition (IMECE2006-14587), Chicago; 2006.

[29] McMahon TA, Bonner JT. "On size and life". New York: W. H. Freeman; 1983.

[30] Zhao Hui, L. C. (2008). "Design of a Versatile Test Bench for Hybrid Electric Vehicles". IEEE Vehicle Power and Propulsion Conference. Harbin.

[31] Lohse-Busch, H. "Development and Applications of the Modular Automotive Technology Testbed (MATT) to Evaluate Hybrid Electric Powertrain Components and Energy Management Strategies". Phd. Dissertation submitted to Varginia Polytechnic Institute and State University . Blacksburg, VA. ,2009.

[32] J. Y. Wong, "Theory of Ground Vehicle". New York: Wiley, 1978, pp. 132–133.

[33] Z. Rahman, K. L. Butler, and M. Ehsani, "Effect of extended-speed, constant-power operation of electric drives on the designand performance of EV propulsion system",presented at the SAE Future Future Car Congr.,Apr. 2000, 2001-01-0699.

[34] M. Ehsani, Y. Gao, and J. M. Miller, "Hybrid Electric Vehicles:Architecture and Motor Drives, " Proceedings of the IEEE., vol. 95, no. 4, April,2007.

[35] http://engines.honda.com/models/model-detail/gx200

[36] http://www.transbearco.com/Tech_Support_Files/Emerson_Manuals/MX_Manual.pdf

[37] http://www.epa.gov/nvfel/testing/dynamometer.htm

[38] http://www.inpowerdirect.com/docs/OM-24D.pdf

[39] http://www.phidgets.com/products.php?category=8&product_id=1135_0

[40] Department of Energy and Idaho National Engineering & Environmental Laboratory Technical Staff, FreedomCAR, Department of Energy and Idaho National Engineering & Environmental Laboratory, 2003.

[41] T.P. Cleary. "Development and Testing of a Flexible Topology Micro-Hybrid Passenger Vehicle Powertrain for Hardware-in-the Loop Simulation and Education, " M.S. thesis, Mech. and Nuc. Eng. Dept., Penn. State Univ., University Park, PA. 2010.

[42] http://www.dieselnet.com/standards/cycles/hwfet.php

[43] http://www.encoder.com/literature/datasheet-25t.pdf

[44] http://www.ogura-clutch.com/products.html?category=2&product=93

[45] http://web.anl.gov/techtransfer/pdf/PSAT.pdf

Appendix A Electrical Drawing

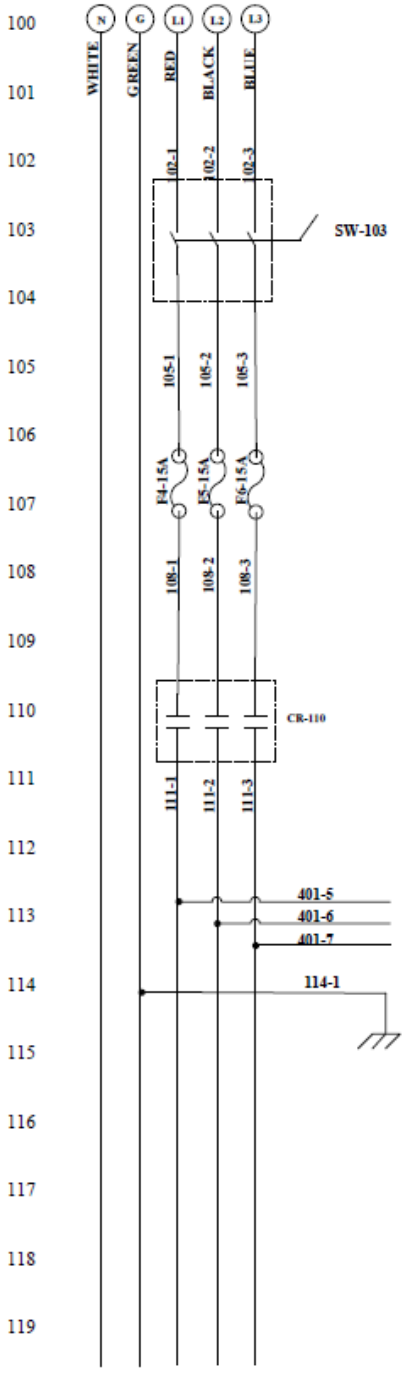

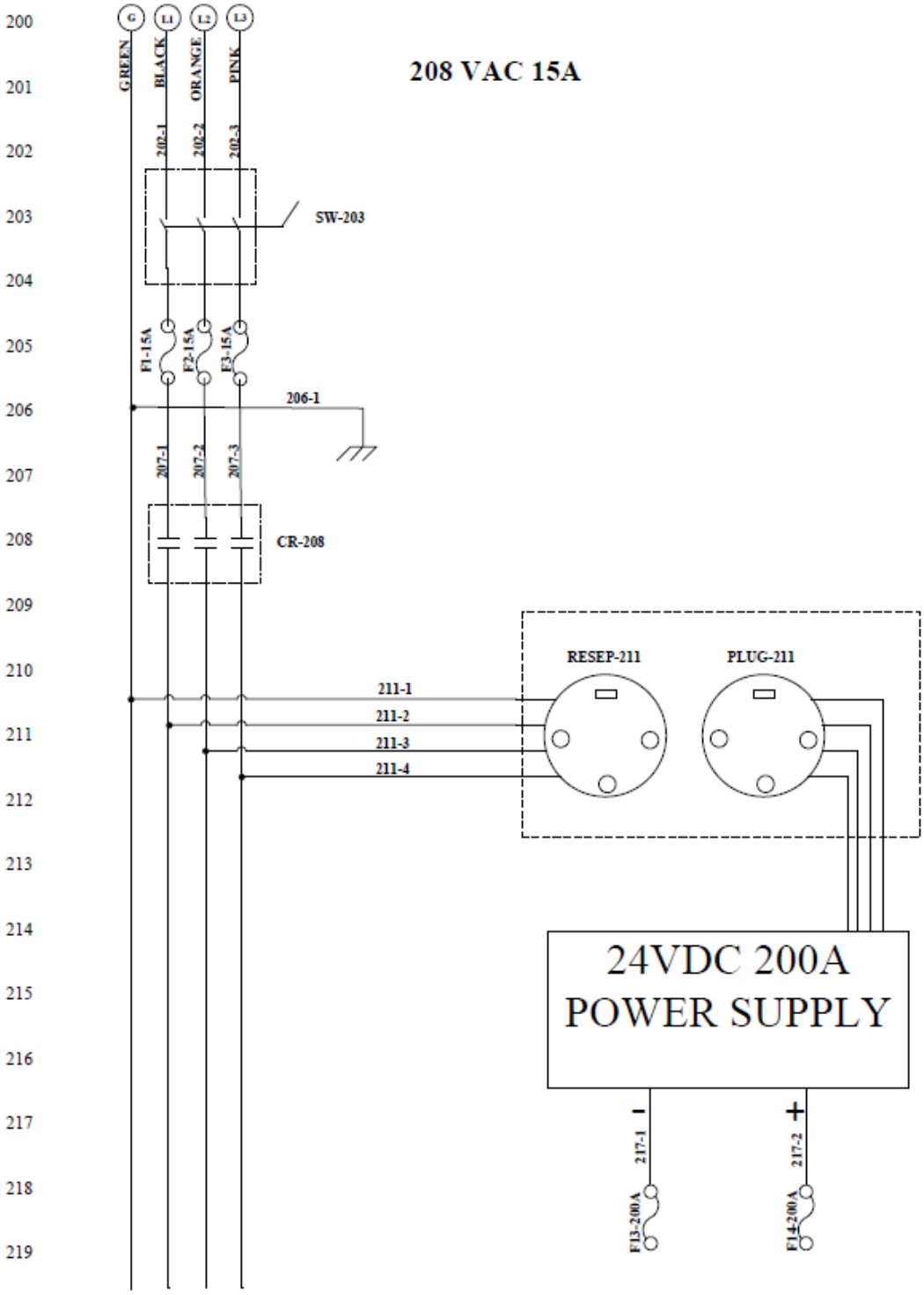
208 VAC 15A
G
L1
L2
L3
GREEN
BLACK
ORANGE
PINK
202-1
202-2
202-3
SW-203
F1-15A
F2-15A
F3-15A
206-1
207-1
207-2
207-3
CR-208
RESEP-211
PLUG-211
211-1
211-2
211-3
211-4
24VDC 200A
POWER SUPPLY
217-1
217-2
F13-200A
F14-200A

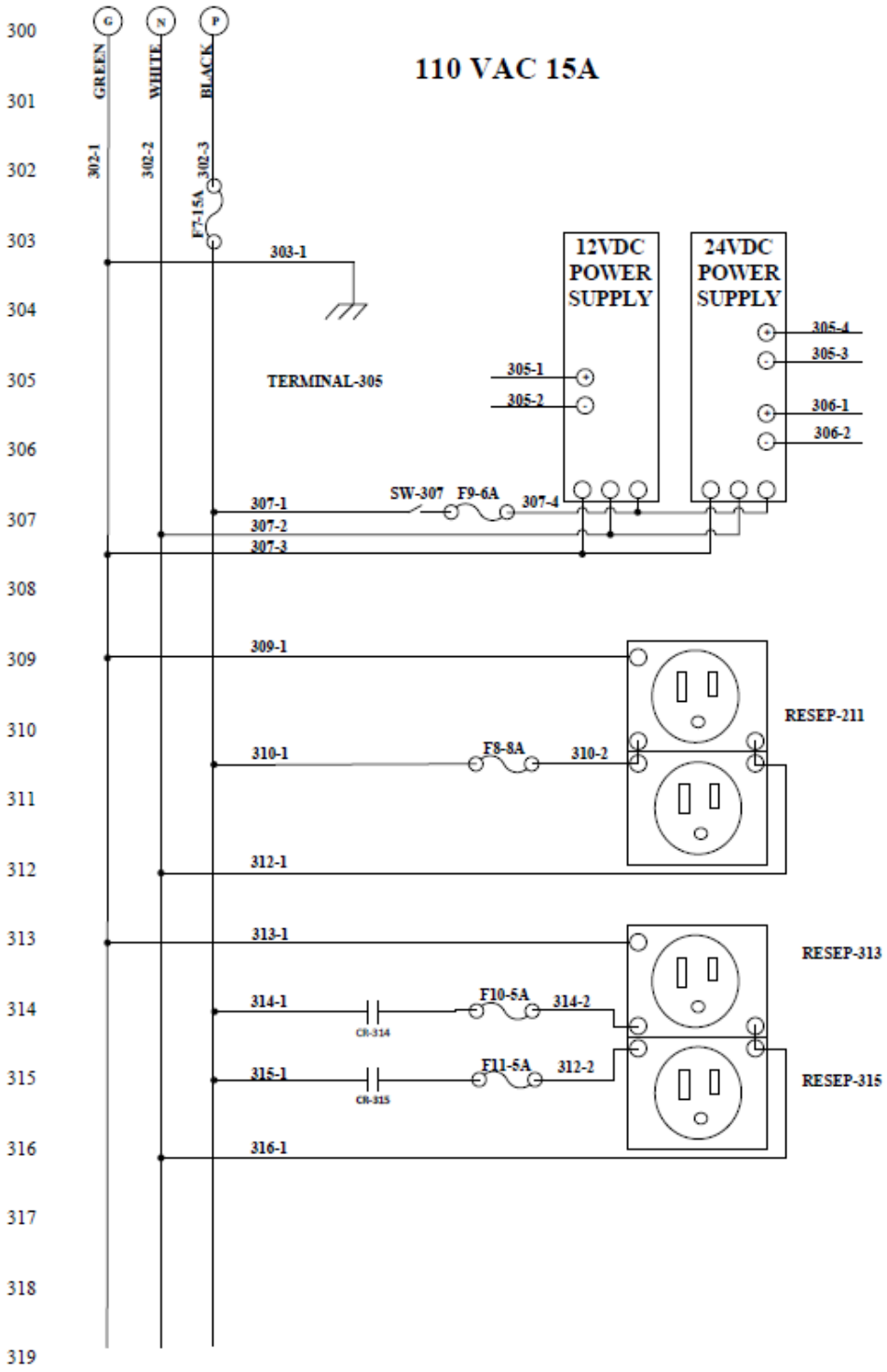
110 VAC 15A
G
N
P
GREEN
WHITE
BLACK
302-1
302-2
302-3
F7-15A
303-1
12VDC POWER SUPPLY
24VDC POWER SUPPLY
TERMINAL-305
305-1
305-2
305-4
305-3
306-1
306-2
SW-307
F9-6A
307-4
307-1
307-2
307-3
309-1
RESEP-211
310-1
F8-8A
310-2
312-1
313-1
RESEP-313
314-1
CR-314
F10-5A
314-2
315-1
CR-315
F11-5A
312-2
RESEP-315
316-1

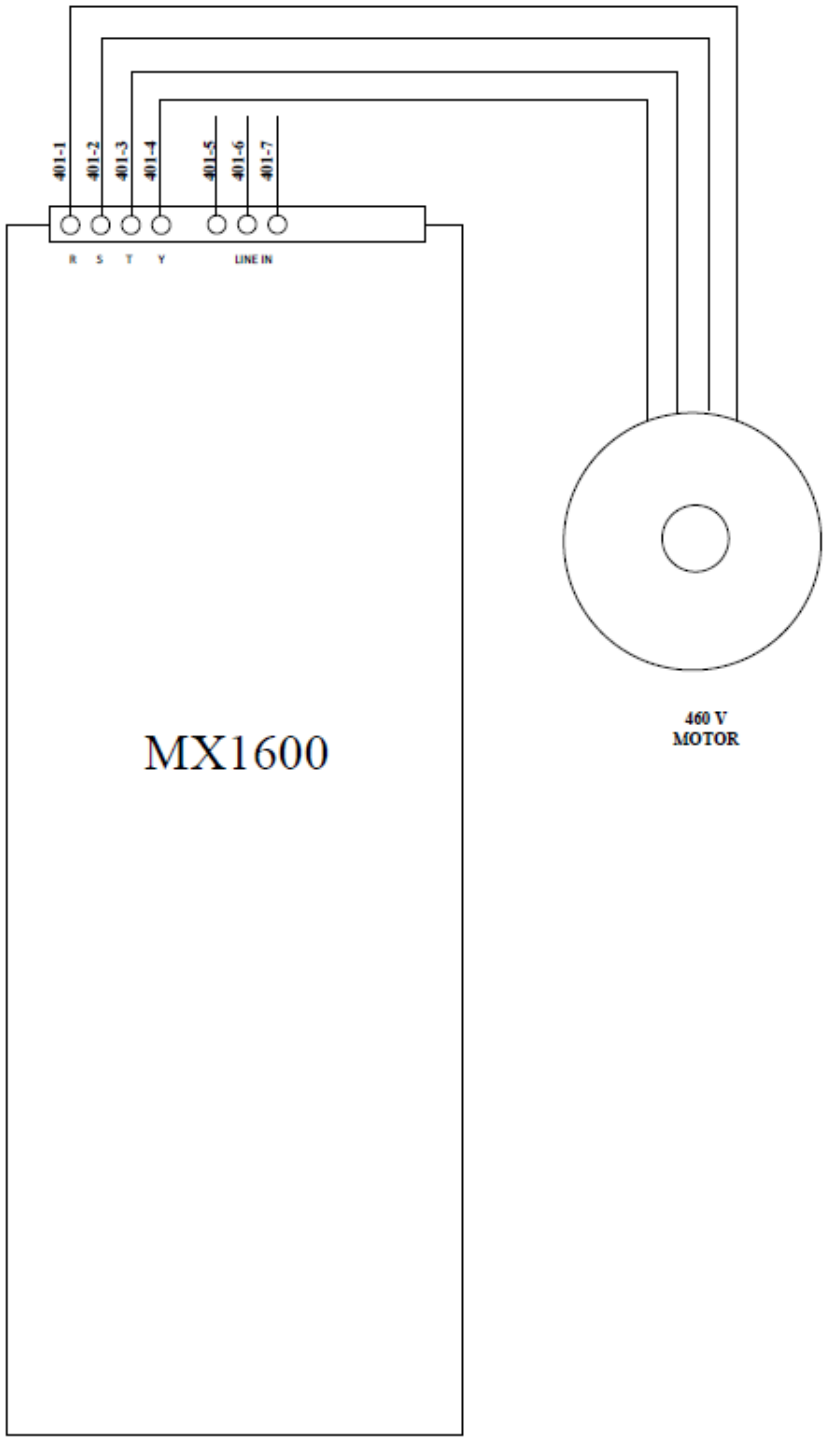
401-1
401-2
401-3
401-4
401-5
401-6
401-7
R
S
T
Y
LINE IN
MX1600
460 V
MOTOR

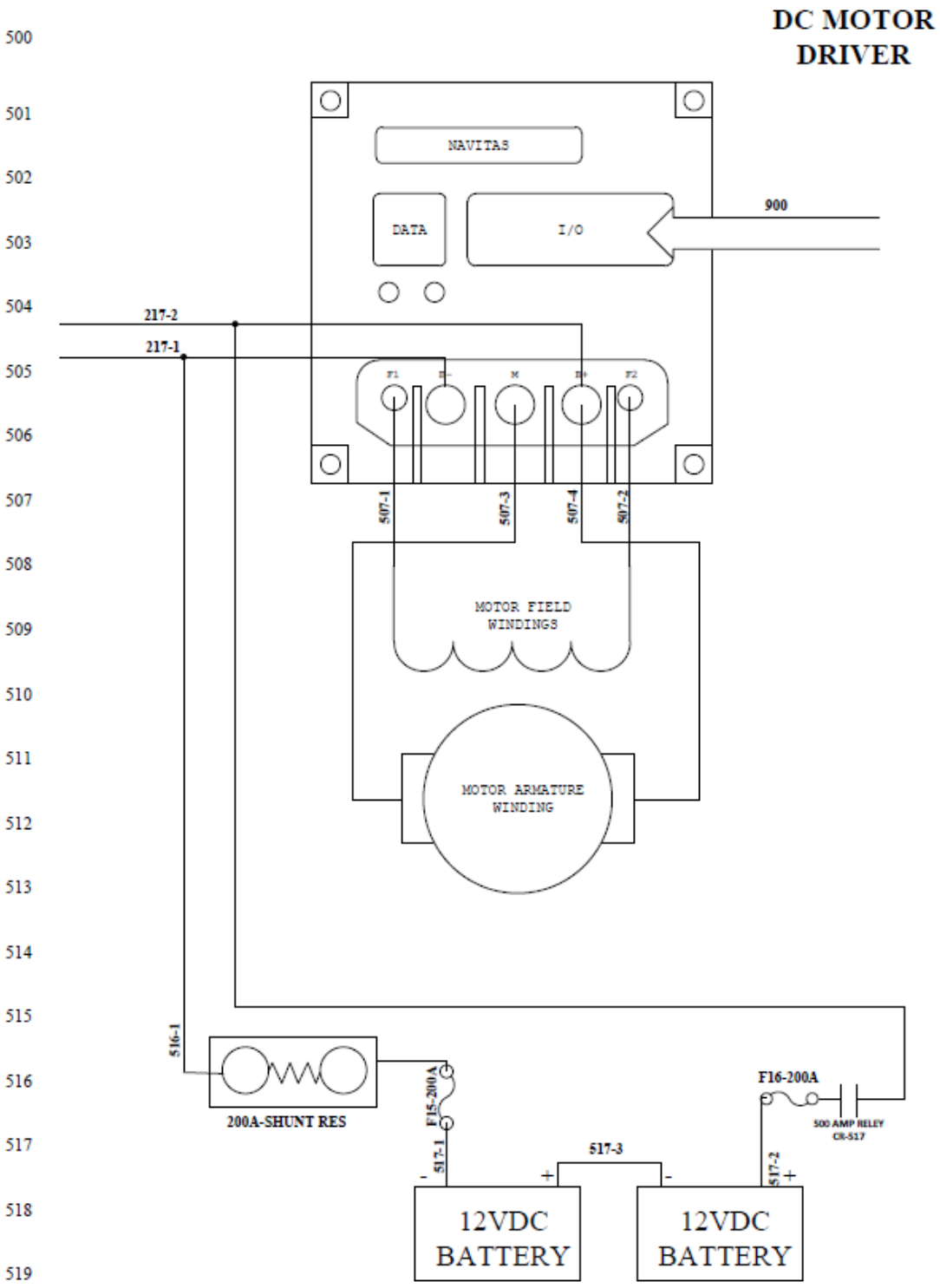
DC MOTOR
DRIVER
NAVITAS
DATA
I/O
900
217-2
217-1
F1
S-
M
S+
F2
507-1
507-3
507-4
507-2
MOTOR FIELD
WINDINGS
MOTOR ARMATURE
WINDING
516-1
200A-SHUNT RES
F15-200A
517-1
517-3
F16-200A
500 AMP RELEY
CR-517
517-2
12VDC
BATTERY
12VDC
BATTERY

SAFTEY

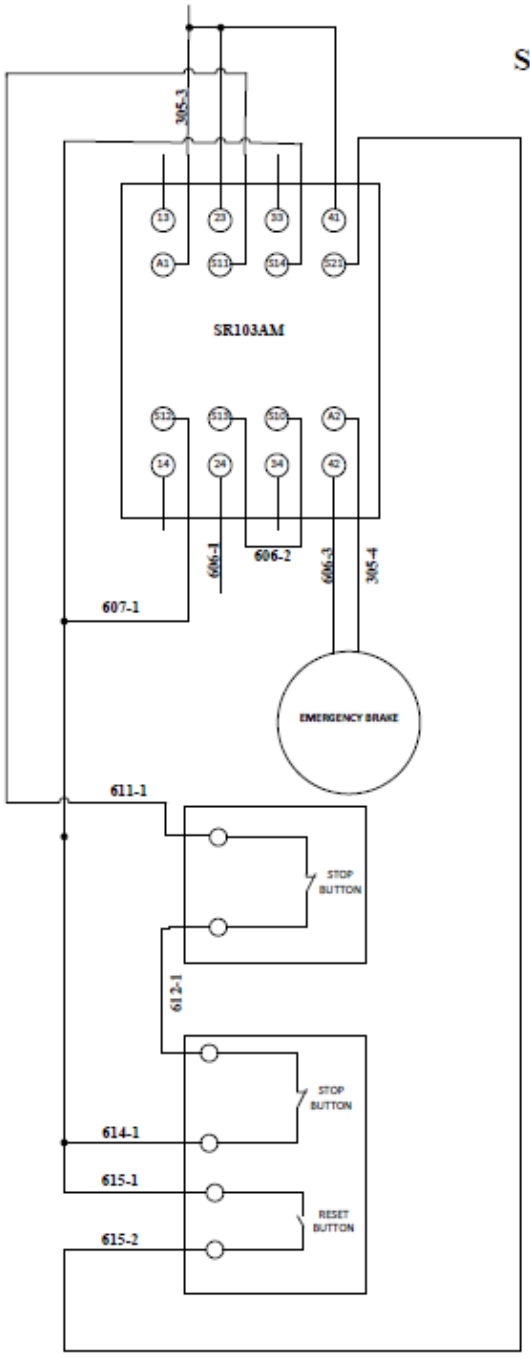

600
601
602
603
604
605
606
607
608
609
610
611
612
613
614
615
616
617
618
619

Internal combustion engine

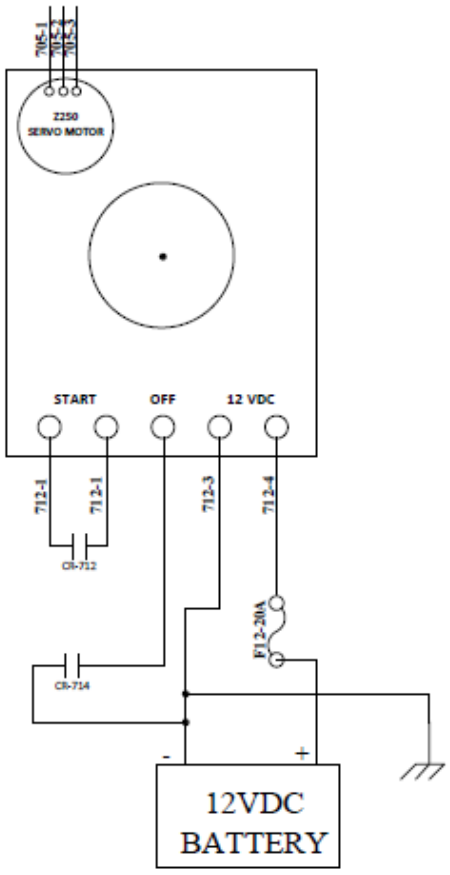

DS 4004

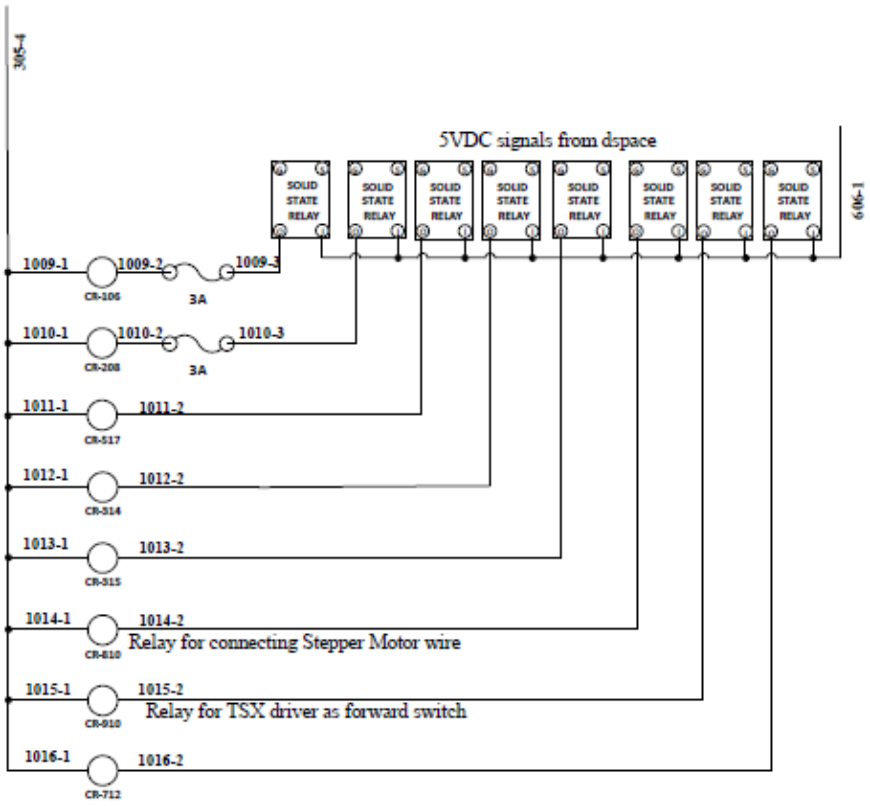
305-4
5VDC signals from dspace
SOLID STATE RELAY
606-1
1009-1
1009-2
1009-3
CR-106
3A
1010-1
1010-2
1010-3
CR-208
3A
1011-1
1011-2
CR-517
1012-1
1012-2
CR-314
1013-1
1013-2
CR-315
1014-1
1014-2
CR-810
Relay for connecting Stepper Motor wire
1015-1
1015-2
CR-910
Relay for TSX driver as forward switch
1016-1
1016-2
CR-712

Appendix B Dc Motor datasheet

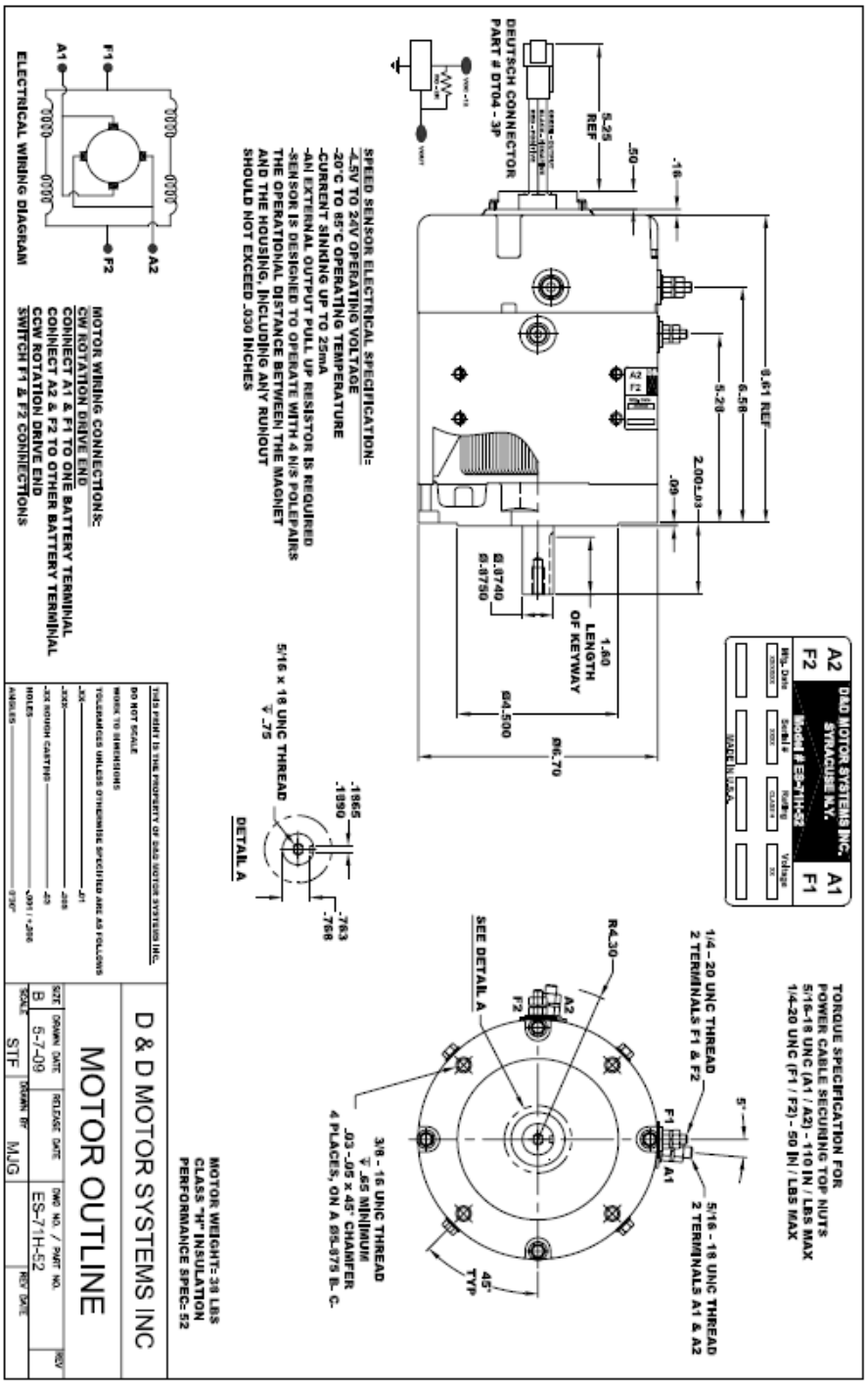

Appendix C Voltage Sensor

Analog Input Cable Connectors

Each Analog Input uses a 3-pin, 0.100 inch pitch locking connector. Pictured here is a plug with the connections labeled. The connectors are commonly available - refer to the Table below for manufacturer part numbers.

Cable Connectors		
Manufacturer	**Part Number**	**Description**
Molex	50-57-9403	3 Position Cable Connector
Molex	16-02-0102	Wire Crimp Insert for Cable Connector
Molex	70543-0002	3 Position Vertical PCB Connector
Molex	70553-0002	3 Position Right-Angle PCB Connector (Gold)
Molex	70553-0037	3 Position Right-Angle PCB Connector (Tin)
Molex	15-91-2035	3 Position Right-Angle PCB Connector - Surface Mount

Note: Most of the above components can be bought at www.digikey.com

Device Specifications

Characteristic	Value
Current Consumption	3.6mA
Input Impedance	1MegaOhm
Recommended Max Difference between Vin+ and Vin-	30V
Absolute Maximum Difference between Vin+ and Vin-	35V
Input CMR	40V
Ouput Range	0 to 5V
Min/Max Error	±2.0%
Typical Error	±0.7%
Maximum Offset at 0V input	±100mV

Product History

Date	Board Revision	Comment
March 2010	0	Product Release

Support

Call the support desk at 1.403.282.7335 9:00 AM to 5:00 PM Mountain Time (US & Canada) - GMT-07:00

or

E-mail us at: support@phidgets.com

Technical Information

General

The Voltage Sensor measures the differential voltage between the input terminals and outputs the difference proportionally. The maximum differential voltage that can be measured accurately is +/-30V. When the positive and negative inputs are equal, the analog output value is 2.5V. When the positive input is 30V greater than the negative input, the analog output is 4.5V and when the positive input is 30V less than the negative input, the analog output is 0.5V.

Since the 1135 Voltage Sensor can measure a differential voltage, the common mode rejection (CMR) is an important specification. CMR refers to the amount of voltage that both input terminals of an differential amplifier can be offset without affecting the output gain. For example, if the positive terminal sees a voltage of 7V and the negative terminal sees a voltage of 5V, then the CMR would be 5V and would output a value of 2V at unity gain. For the 1135 Voltage Sensor, it is able to measure the differential voltage of +/-10V with a CMR of 40V while keeping the accuracy within 2%.

Please note that the error specifications do not include the error introduced by the Analog to Digital Conversion on the Analog Input. (if you are using the 1135 with a PhidgetInterfaceKit) The majority of error introduced by the Analog to Digital Conversion is from the error in the voltage reference (0.5% max), and the limitation of resolution in the SensorValue property. The best accuracy can be achieved by using a 2 or more point calibration of your system - effectively calibrating the 1135 and the PhidgetInterfaceKit in a single step. If you are calibrating, be sure to use a good quality multimeter to determine the voltage being applied.

Using RawSensorValue in the formula will increase the resolution, which is limited by SensorValue to about 67mV.

Formulas

The Formula to translate SensorValue into differential voltage is:

$$Vdifference = ((SensorValue / 200) - 2.5) / 0.0681$$

where Vdifference is defined as Vpositive - Vnegative.

Other Interfacing Alternatives

If you want maximum accuracy, you can use the RawSensorValue property from the PhidgetInterfaceKit. To adjust a formula, substitute (SensorValue) with (RawSensorValue / 4.095)

If the sensor is being interfaced to your own Analog to Digital Converter and not a Phidget device, our formulas can be modified by replacing (SensorValue) with (Vin * 200). It is important to consider the voltage reference and input voltage range of your ADC for full accuracy and range.

Coding for your Sensor

Phidget analog sensors do not have their own API, but instead their output is a voltage that is typically converted to a digital value and accessed through the SensorValue properties and events on a Phidget InterfaceKit. It is not possible to programmatically identify which sensor is attached to the Analog Input. Your application will need to apply the formula from this manual to the SensorValue to translate it into usable data.

Please see the Phidget InterfaceKit product manual for code samples, an overview of its API, and a description of our architecture.

Appendix D Current Sensor

OWNERS MANUAL

DCS 35/36 Series
Hall-Effect DC Current Sensors

A. Introduction

The DCS 35/36 Series is a family of Hall-effect dc current sensors designed to interface to electronic instruments or vehicle multiplexed systems. Although they are typically used in vehicle and marine applications to measure battery charging or discharging currents, they can be applied in a variety of dc circuits to measure bidirectional current. The sensors measure positive and negative current values, or just a positive range. In the example of the model DCS35-300-1, the measuring range is -300 amps to +300 amps, with a corresponding output of 2.5 V ± 2.0 V. The model DCS36-300-2 would measure 0 to 300 amps, with a corresponding output of 0 volts to +5.0 volts. The sensors require a power source of 12 Vdc (ground and +12 volts).

DC Current Sensor Models

Model	Current Range	Output	Model	Current Range	Output
DCS35-100-1	± 100 Amps	2.5 V ± 2.0 V	DCS35-400-1	± 400 Amps	2.5 V ± 2.0 V
DCS35-200-1	± 200 Amps	2.5 V ± 2.0 V	DCS35-500-1	± 500 Amps	2.5 V ± 2.0 V
DCS35-300-1	± 300 Amps	2.5 V ± 2.0 V	DCS35-600-1	± 600 Amps	2.5 V ± 2.0 V
DCS35-100-2	± 100 Amps	2.5 V ± 2.5 V	DCS35-400-2	± 400 Amps	2.5 V ± 2.5 V
DCS35-200-2	± 200 Amps	2.5 V ± 2.5 V	DCS35-500-2	± 500 Amps	2.5 V ± 2.5 V
DCS35-300-2	± 300 Amps	2.5 V ± 2.5 V	DCS35-600-2	± 600 Amps	2.5 V ± 2.5 V
DCS36-100-1	0 to 100 Amps	0.5 to 4.5 V	DCS36-400-1	0 to 400 Amps	0.5 to 4.5 V
DCS36-200-1	0 to 200 Amps	0.5 to 4.5 V	DCS36-500-1	0 to 500 Amps	0.5 to 4.5 V
DCS36-300-1	0 to 300 Amps	0.5 to 4.5 V	DCS36-600-1	0 to 600 Amps	0.5 to 4.5 V
DCS36-100-2	0 to 100 Amps	0 to 5.0 V	DCS36-400-2	0 to 400 Amps	0 to 5.0 V
DCS36-200-2	0 to 200 Amps	0 to 5.0 V	DCS36-500-2	0 to 500 Amps	0 to 5.0 V
DCS36-300-2	0 to 300 Amps	0 to 5.0 V	DCS36-600-2	0 to 600 Amps	0 to 5.0 V

System Diagram

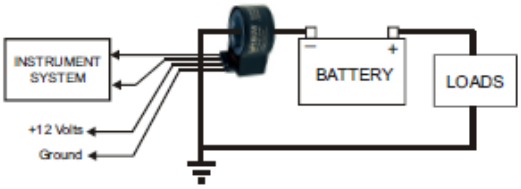

Sensor Wiring

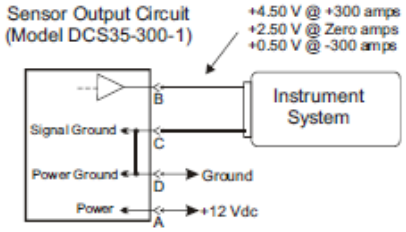

InPOWER LLC
3555 Africa Road
Galena, Ohio 43021 U.S.A
(866)548-0965
www.InPowerDirect.com

Owners Manual

Document: OM-24 Revision: D
Date: May 26, 2004 Date: January 14 , 2008

B. Specifications

Sensor Type:	Open loop Hall-effect
Linearity:	1.5%
Supply Voltage Range:	+7 to + 20 Vdc
Current Consumption:	8.1 milliamps maximum
Sensor Output:	0.5 V to 4.5 Vdc, 0 V to 5.0 V, 2.5 V ± 2.0 V, or 2.5 V ± 2.5 V
Operating Temperature:	-40° C to +125° C
Storage Temperature:	-40° C to +125° C
Aperture Size:	1.23 inches
Weight:	0.30 lbs
Dimensions:	2.66" x 2.10" x 1.10"
Connector System:	Packard Sealed Metri-Pak 150. Note - Mating plug not supplied with sensor. See InPower Technical Bulletin TB-31 for details and purchasing source.

C. Installation

1. Getting Started

Before starting, make sure that you have the correct connector plug parts, interface cable, sensor mounting bracket and screws, and tools. Determine the location where the sensor will mount and the required cable length/routing to the instrument system. Avoid mounting the sensor close to very hot engine parts such as the exhaust manifold.

2. Install The Sensor

Mount the sensor and route the battery cable through its aperture. The sensor may be secured to the battery cable using tie wraps, or a mounting bracket could be fabricated that will secure the sensor via its three bracket holes to a mounting surface or to the battery cable. Use #6 self tapping screws and be sure that the screws do not protrude into the sensor more than 0.30 inches. **Be sure to mount the sensor in the proper direction to correctly measure the charging (plus) and discharging (minus) battery current.** See the following diagram for suitable sensor mounting locations.

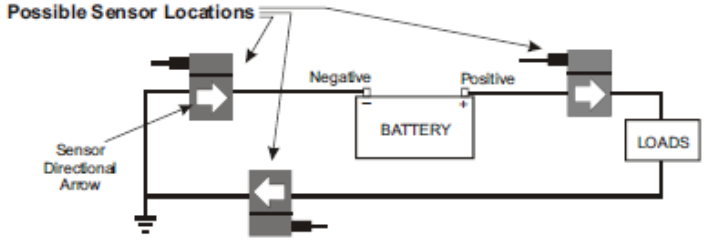

3. Install and Wire the Cable

Wire the mating four-pin plug that connects to the sensor and route the cable to the instrument system. You will need to wire two sensor connector pins to the instrument system and two pins to ground and +12 volts.

4. Check Sensor and Meter Operation

Apply power to the sensor and verify that the meter is working correctly by checking battery charging and discharging conditions. It would be helpful to use a clamp-on ammeter such as a Fluke to verify proper operation.

D. Mechanical Drawing

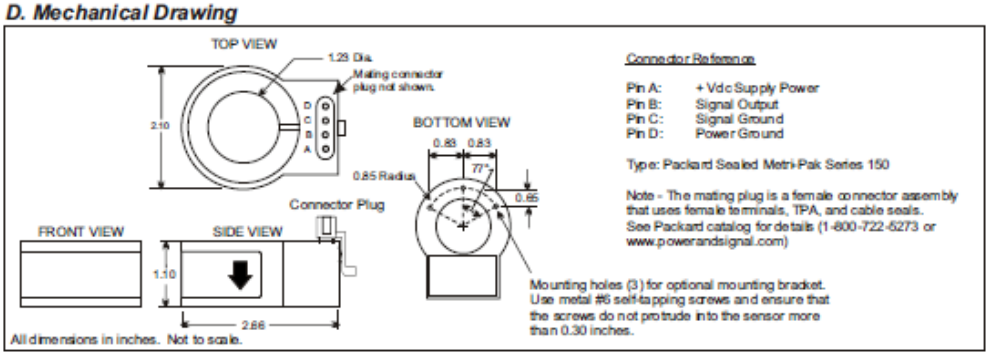

Appendix E Emergency Brake Manual (TMB 20H) [44]

TMB-H

EM Brake (with hub)

Types: 0.6, 1.2, 2.5, 5, 10, 20

[EM: Electromagnet]

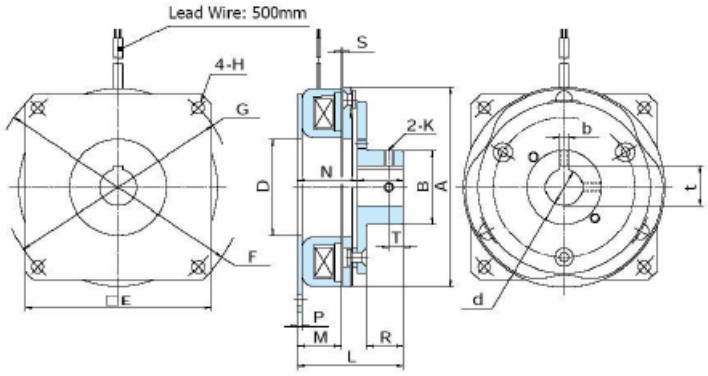

[Special Order]

TMB		0.6H	1.2H	2.5H	5H	10H	20H
Static Torque [ft-lbs / N-m]		4.4 / 6	8.9 / 12	18 / 24	37 / 50	74 / 100	148 / 200
Coil (20°C)	Voltage [DC-V]	24					
	Current [A]	0.5	0.65	0.92	1.35	1.6	2.2
	Resistance [Ω]	48	37	26	18	15	11
	Wattage [W]	12	15	22	33	38	53
Armature	Pull-In Time [ms]	10	16	16	25	40	55
	Release Time [ms]	10	10	24	25	35	62
Torque Build-Up Time [ms]		42	46	51	56	78	95
Max Allowable Speed [rpm]		5000	5000	4500	4000	3600	3000
Moment of Inertia (J) [kg-cm²]		0.75	2.5	7.8	23	72	248
Max Air Gap Until Adjustment [mm]		0.5	0.6	0.7	0.8	1.2	1.5
Total Energy Until Adjustment [J]		2.9×10^7	6.6×10^7	13×10^7	26×10^7	62×10^7	120×10^7
Total Energy Until Life [J]		13×10^7	25×10^7	49×10^7	88×10^7	170×10^7	320×10^7
Bore [mm]	d_{H7}	12	15	20	25	30	40
Key Way [mm]	b_{E9}	4	5	5	7	7	10
	$t_{+0.15/-0}$	13.5	17	22	28	33	43.5
Dimensions [mm]	A	67	86	108	136	170	215
	B	26	32	40	50	65	80
	$D_{+0.2/-0}$	35	45	52	65	80	107
	E	62	82	100	125	156	200
	$F_{+0/-0.2}$	85	110	135	165	210	265
	G	75	98	122	150	190	240
	H	4.5	5.5	6.5	6.5	8.5	11
	K	M4	M5	M5	M6	M8	M8
	L	39.5	47.5	56.5	65	80	97.5
	M	19.2	21.1	23.4	25.2	27.1	31.2
	N	24.5	27.5	31.5	35	40	47.5
	O	15	20	25	30	40	50
	P	1.8	2.1	2.4	2.4	2.7	3
	R	11.5	16	20	24	33	41
	S	0.2~0.3	0.2~0.3	0.2~0.3	0.2~0.3	0.3~0.4	0.4~0.5
	T	6	8	8	10	10	15
Weight [lbs / kg]		0.9 / 0.4	2.0 / 0.9	3.5 / 1.6	6.0 / 2.7	11 / 5	21 / 10

[Included parts & accessories : shims, surge protector]

[1 inch = 25.4 mm]

Ogura Industrial
100 Randolph Rd.
Somerset, NJ 08875

www.ogura-clutch.com
info@ogura-clutch.com
(732) 271-7361

Appendix F Encoder 25T-1200N-SMH [43]

Model 25T Thru-Bore, or
Model 25H Hollow Bore (Blind)

ENCODER PRODUCTS COMPANY

Features

- 2.5" Opto-ASIC Encoder with a Low Profile (2.0")
- Standard Bore Sizes Ranging from 0.625" to 1.125"
- Metric Bore Sizes Ranging from 6 mm to 28 mm
- Single Replacement Solution For 2.0" to 3.5" Encoders
- Resolutions to 10,000 CPR; Frequencies to 1 MHz
- Versatile Flexible Mounting Options
- RoHS Compliant

Introducing the next generation of high performance encoders - the Model 25T. As contemporary as its appearance, the Model 25T features the largest thru-bore available in a 2.5" encoder, mounting directly on shafts as large as 1.125" or 28 mm. With resolutions of up to 10,000 CPR, and Frequencies of up to 1MHz this industrial strength encoder is perfect for fast revving motors. The 25T features the next generation of EPC's proprietary Opto-ASIC sensor which provides superior accuracy and precision counts. The injection molded housing, made from EPC's custom blend of nylon composites, is grooved with "cooling fins" and can take the extreme heat of the motion control industry. With sealing available of up to IP66 and many new rugged flexible mounting options, the Model 25T can perform in demanding industrial environments. This revolutionary new 2.5" encoder truly is unlike any other.

Common Applications

Motor-Mounted Feedback and Vector Control, Specialty Machines, Robotics, Web Process Control, Paper and Printing, High Power Motors

Model 25T/H Ordering Guide

Blue type indicates price adder options. Not all configuration combinations may be available. Contact Customer Service for details.

Mechanical | Electrical | Optional Features (Leave Blank For Standard Options)

25T	[ ]	-	42	SE	-	0500	N	V1	R	OC	-	SMW	[ ]	[ ]	[ ]
MODEL	Housing Option		BORE SIZE[1]	MOUNTING		CYCLES PER REVOLUTION	COMMUTATION	INPUT VOLTAGE	NUMBER OF CHANNELS[1]	OUTPUT TYPE		CONNECTOR TYPE	OPERATING TEMPERATURE	SEALING	CERTIFICATION
													-20° to +85°C Std	IP50 Std	None Std

MODEL
25T Thru-Bore
25H Hollow Bore

Housing Option (Leave Blank for Standard)
Standard
C Corrosion Resistant

BORE SIZE[1]
03 5/16", 0.3125"
01 1/4", 0.250"
02 3/8", 0.375
05 1/2", 0.500"
11 5/8", 0.625"
34 3/4", 0.750"
78 7/8", 0.875"
40 1", 1.000"
42 1-1/8", 1.125"
04 6 mm
14 8 mm
10 10 mm
09 11 mm
12 12 mm
13 14 mm
15 15 mm
16 16 mm
19 19 mm
20 20 mm
24 24 mm
25 25 mm
28 28 mm

MOUNTING
SE 2.25" to 2.75" B.C. 3-point Flex Mount
SG 3.50" to 5.90" B.C. (4.5" C-face) Tether Arm Kit
SJ 3.50" to 8.10" B.C. (8.5" C-face) Tether Arm Kit
SH 2.72" to 3.42" B.C. (Block & Pin) Tether Arm Kit

CYCLES PER REVOLUTION
See CPR Options below
Price Adder For Resolutions Over 2000

COMMUTATION
N None

INPUT VOLTAGE
V1 5 to 28 VDC

NUMBER OF CHANNELS[1]
Channel A Leads B
Q Quadrature A & B
R Quadrature A & B with Index
Channel B Leads A[11]
K Reverse Quadrature A & B
D Reverse Quadrature A & B with Index
See http://www.encoder.com/literature/index-phasing.pdf for additional options, and waveforms.

OUTPUT TYPE
5 - 28V In/Out[9]
OC Open Collector
PP Push-Pull
HV Line Driver[4]
PU Pull-Up Resistor[5]
5 - 28V In/5V Out[6]
H5 Line Driver[4]
P5 Push-Pull

CONNECTOR TYPE
SMW 6-pin MS Style[12]
SMY 7-pin MS Style
SMX 10-pin MS Style
SMJ 5-pin M12 (12 mm)
SMK 8-pin M12 (12 mm)
SMH 10-pin Bayonet[10]
F00 Gland, 24" Cable[7]
9D 9-pin D-Sub[10]

OPERATING TEMPERATURE
-20 to 85° C (Std)
T4 -20° to +105° C[2]

SEALING
IP50 (Standard)
S3 IP66

CERTIFICATION
None (Std)
CE CE Marked[8]

For specification assistance call Customer Service at 1-800-366-5412

Model 25T/H CPR Options

0002	0003	0004	0005	0008	0010	0011
0012	0024	0025	0030	0032	0060	0064
0070	0080	0100	0105	0115	0120	0125
0150	0192	0240	0250	0256	0300	0336
0360	0500	0512	0600	1000	1024	1200
2000	2048	2500	4096	5000	10,000	

Contact Customer Service for other disk resolutions.

NOTES:
1 Contact Customer Service for additional options.
2 Contact Customer Service for availability on resolutions < 360 CPR.
3 24 VDC max for T4 temperature option.
4 Not available with 5-pin M12 or 6-pin MS style connectors. Available with 7-pin MS style connector without index Z.
5 With Input Voltage above 16 VDC, operating temperature is limited to 85° C max.
6 Standard operating temperature only.
7 For non-standard English cable lengths enter 'F' plus cable length expressed in feet. Example: F06 = 6 feet of cable.
8 Please refer to Technical Bulletin TB100: *When to Choose the CE Option* at www.encoder.com. Contact Customer Service for availability.
9 Not available with Pull-Up Output Type.
10 Not available with corrosion resistant option.
11 Reverse Quadrature not available with PU output type.
12 Not available with CE option.

Model 25T Thru-Bore, or
Model 25H Hollow Bore (Blind)

ENCODER PRODUCTS COMPANY

Model 25T/H Specifications

Electrical

- Input Voltage: 4.75 to 28 VDC max for temperatures up to 85° C
  4.75 to 24 VDC max for temperatures between 85° and 105° C
- Input Current: 100 mA max with no output load
- Output Format: Incremental- Two square waves in quadrature with channel A leading B for clockwise shaft rotation, as viewed from the mounting face.
  See *Waveform Diagram*.
- Output Types: Open Collector- 20 mA max per channel
  Pull Up - Open Collector with 2.2K ohm resistor, 20 mA max per channel
  Push-Pull- 20 mA max per channel
  Line Driver- 20 mA max per channel (Meets RS 422 at 5 VDC supply)
- Index: Once per revolution.
  361 to 10,000 CPR: Gated to output A
  1 to 360 CPR: Ungated
  See *Waveform Diagram*.
- Max Frequency: 250 kHz for 1 to 2500 CPR
  500 kHz for 2501 to 5000 CPR
  1 MHz for 5001 to 10,000 CPR
- CE Testing: Emissions tested per EN61000-6-3:2001 as applicable. Immunity tested per EN6100-6-2: 2005 as applicable
- Min. Edge Sep.: 45° electrical min, 63° electrical or better typical
- Rise Time: Less than 1 microsecond
- Accuracy: Within 0.1° mechanical from one cycle to any other cycle, or 6 arc minutes.

Mechanical

- Max Shaft Speed: 6000 RPM, 8000 RPM intermittent
  4000 RPM for IP66 seal option
- Bore Size: 0.250" through 1.125"
  6 mm through 28 mm
- Bore Tolerance: -0.00007/+0.0008"
- User Shaft Tolerances
  - Radial Runout: 0.005" max
  - Axial Endplay: ±0.050" max
- Starting Torque: IP50 sealing: 1.0 oz-in typical
  IP66 sealing: 4.0 oz-in typical
  Note: Add 1.0 oz-in typical for -20° C operation
- Moment of Inertia: 7.6×10^{-4} oz-in-sec^2
- Max Acceleration: 1×10^5 rad/sec^2
- Electrical Conn: 6-, 7-, or 10-pin MS Style, 5- or 8-pin M12 (12 mm), 10-pin Bayonet or gland with 24 inches of cable (foil and braid shield, 24 AWG conductors), 9-pin D-Sub
- Housing: Proprietary nylon composite
- Mounting: 2.25" to 2.75" B.C. 3-point flex mount
  3.50" to 5.90" B.C. (4.5" C-face) tether arm kit, 3.50" to 8.10" B.C. (8.5" C-face) tether arm kit and 2.72" to 3.42" B.C. (Block & Pin) tether arm kit. See mechanical drawing for dimensions
- Weight: 8 oz typical

Environmental

- Operating Temp: -20° to 85° C for standard models
  -20° to 105° C for high temperature option
- Storage Temp: -20° to +85° C
- Humidity: 98% RH non-condensing
- Vibration: 20 g @ 5 to 2000 Hz
- Shock: 80 g @ 11 ms duration
- Sealing: IP50, IP66 with shaft seals at both ends

Protect your encoder with the 56C Cover.

Model 25T/H

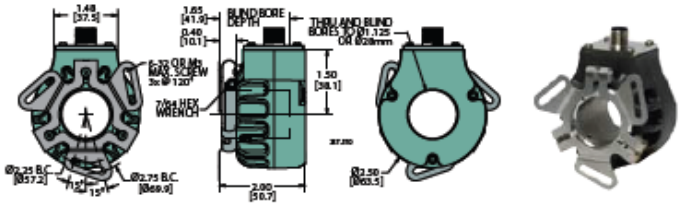

Model 25T/H Connector Options

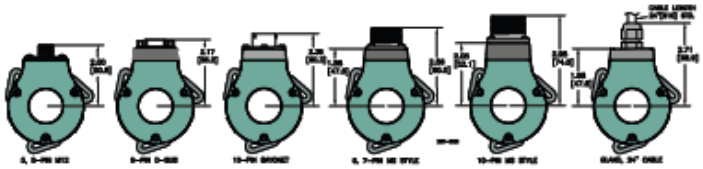

Model 25T/H Mounting Options

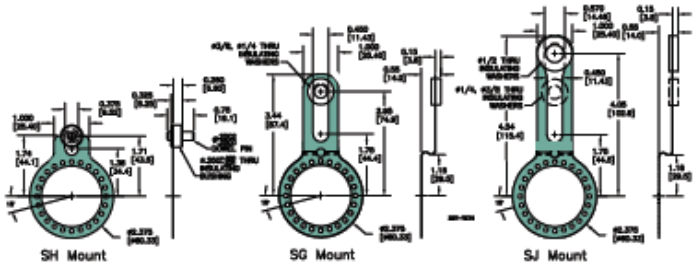

All dimensions are in inches with a tolerance of ±0.005" or ±0.01" unless otherwise specified

Waveform Diagram

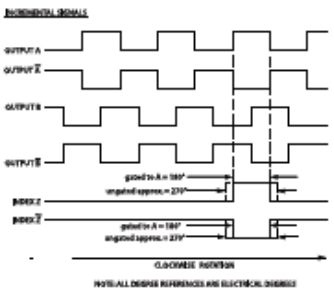

Wiring Table

Function	Gland Cable Wire Color	5-pin M12[1]	8-pin M12[2]	10-pin MS	7-pin MS MV, MS	7-pin MS PU, PP, QQ, RR	8-pin MS RJ, PP, QQ, PR	9-pin D-sub	10-pin MS MV, MS, MP, QQ, PR
Com	Black	3	7	F	F	F	A,F	9	F
+VDC	White	1	2	D	D	D	B	1	D
A	Brown	4	1	A	A	A	D	2	A
Ā	Yellow	---	3	H	C	---	---	3	H
B	Red	2	4	B	B	B	E	4	B
B̄	Green	---	5	I	E	---	---	5	J
Z	Orange	5	6	C	---	C	C	6	C
Z̄	Blue	---	8	J	---	---	---	7	K
Case	---	---	---	G	G	G	---	8	G
Shield	Bare[1]	---	---	---	---	---	---	---	---

[1] CE Option: Cable shield (bare wire) is connected to internal case
[2] CE Option: Read Technical Bulletin TB 111

Appendix G MATLAB Simulink Snapshots

Total Snapshots

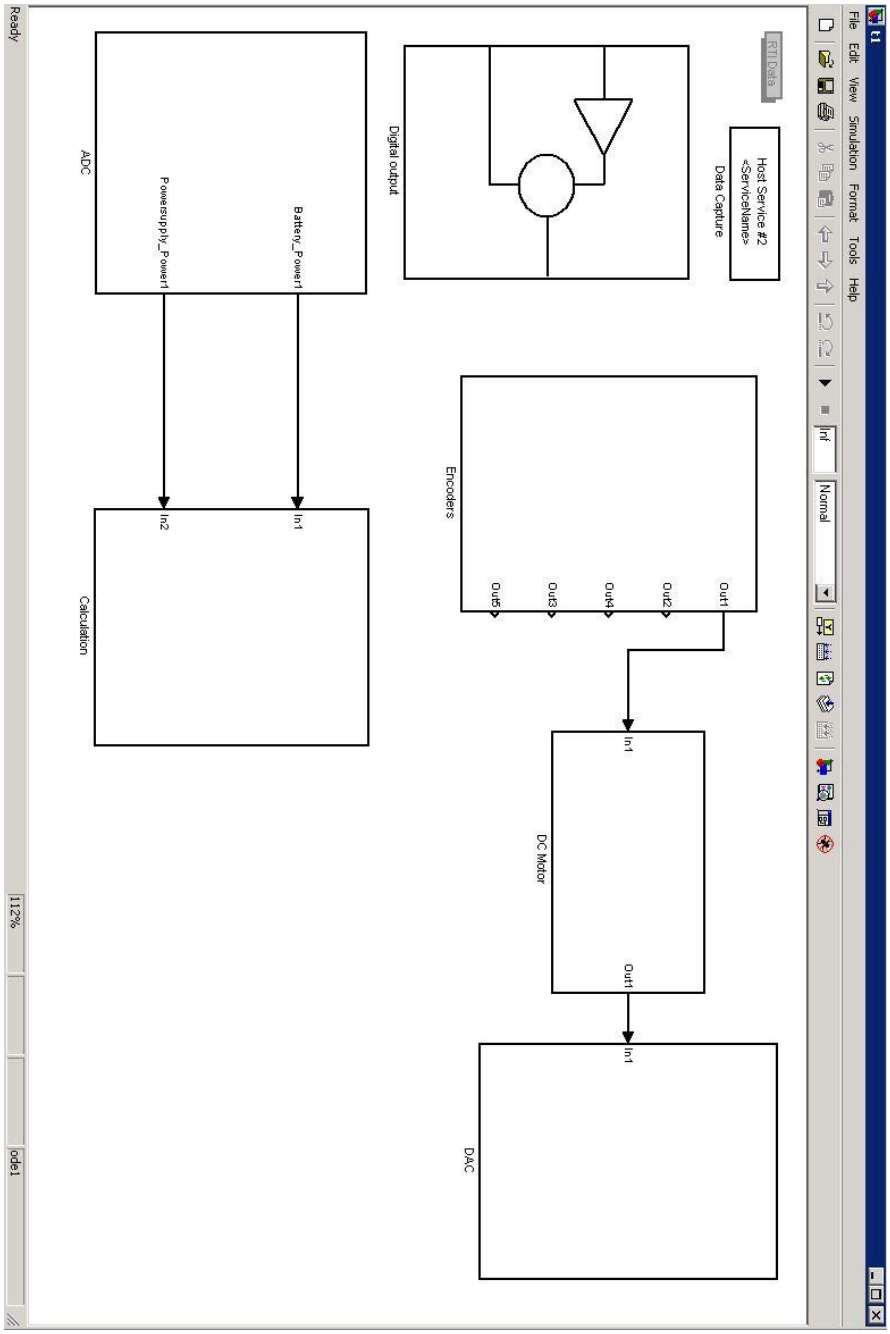

Digital Output (DS 4004)

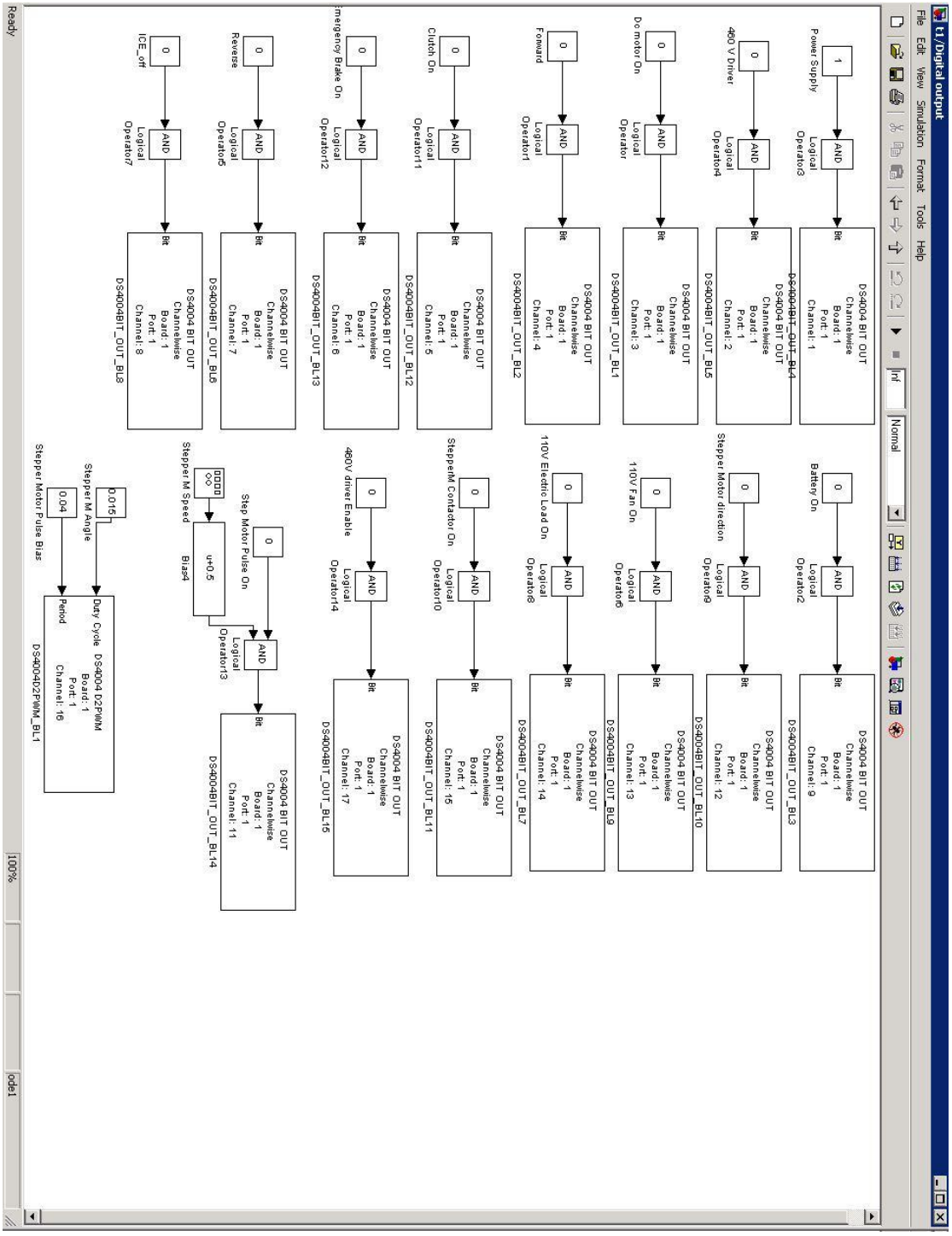

Encoders (DS 3001)

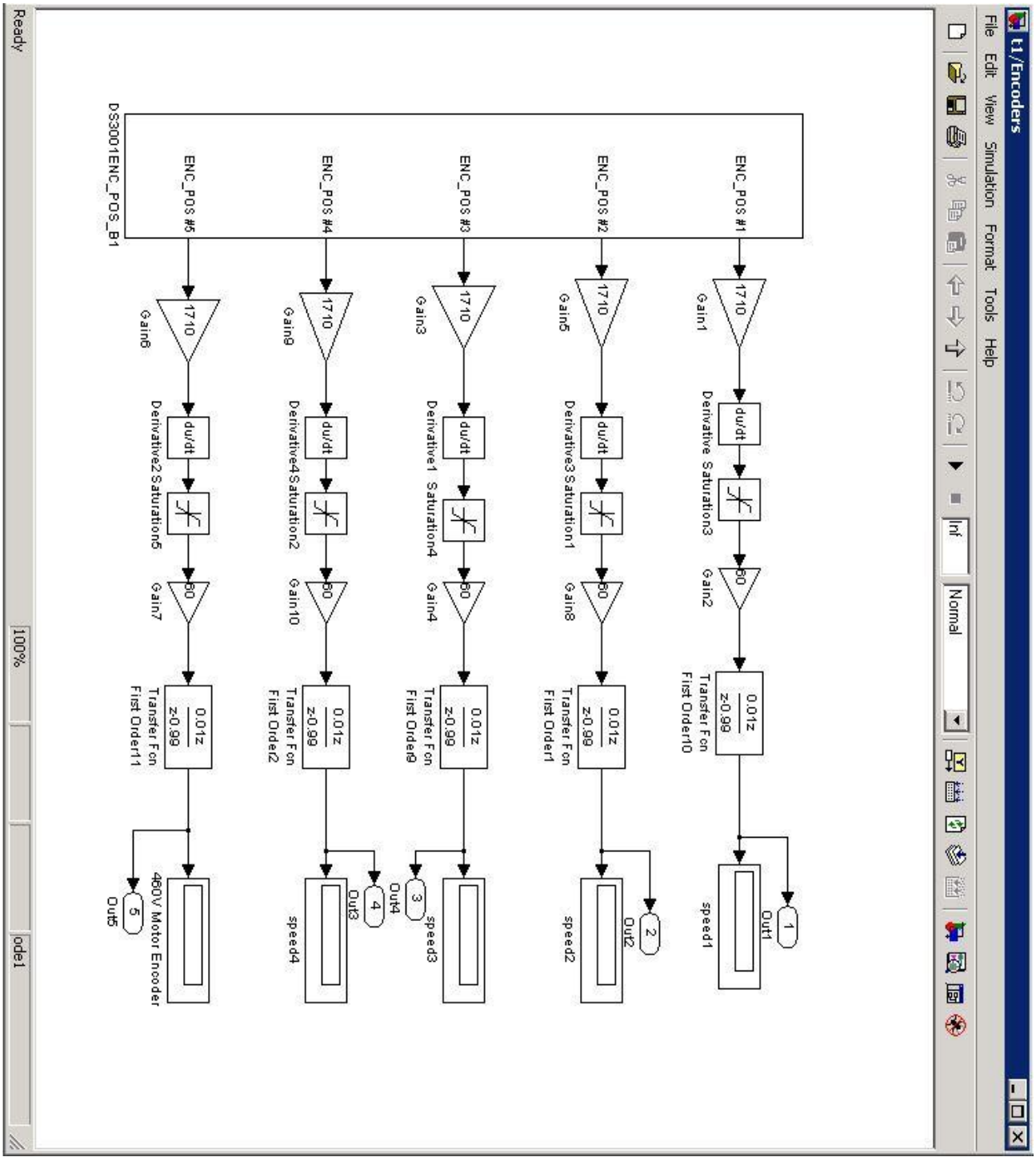

Analog output (DS 2103)

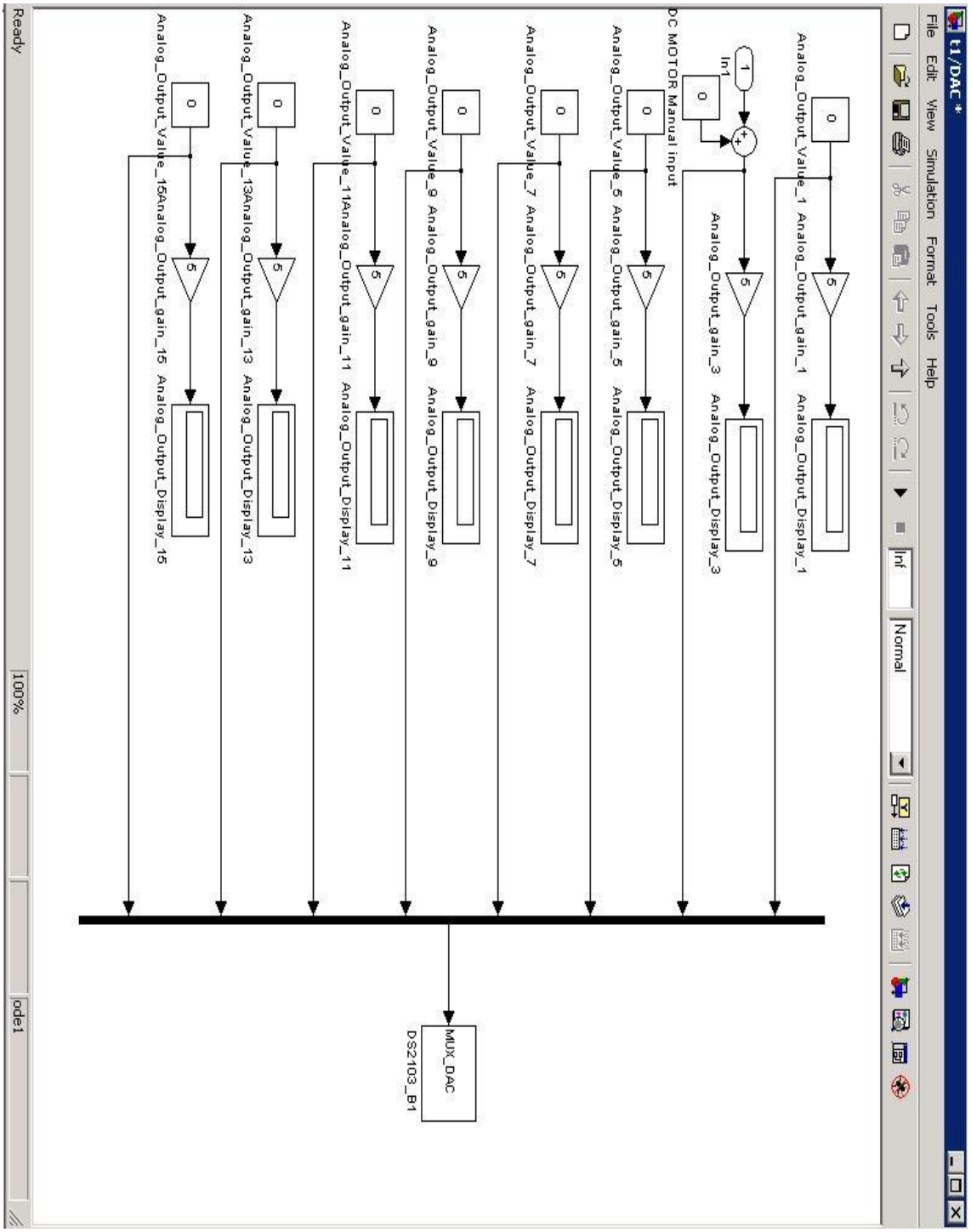

Analog input (DS 2002)

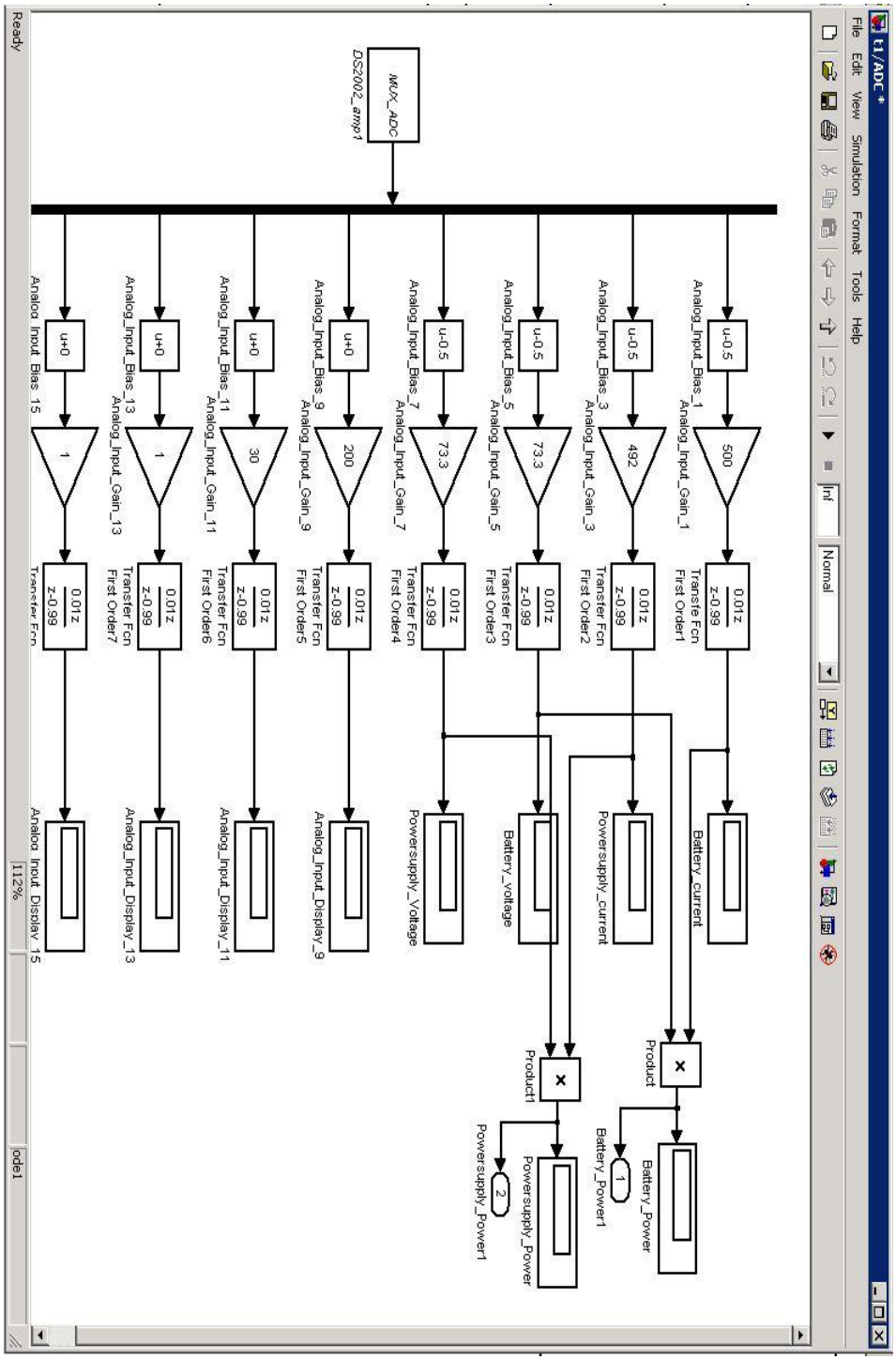

DC motor PID controller

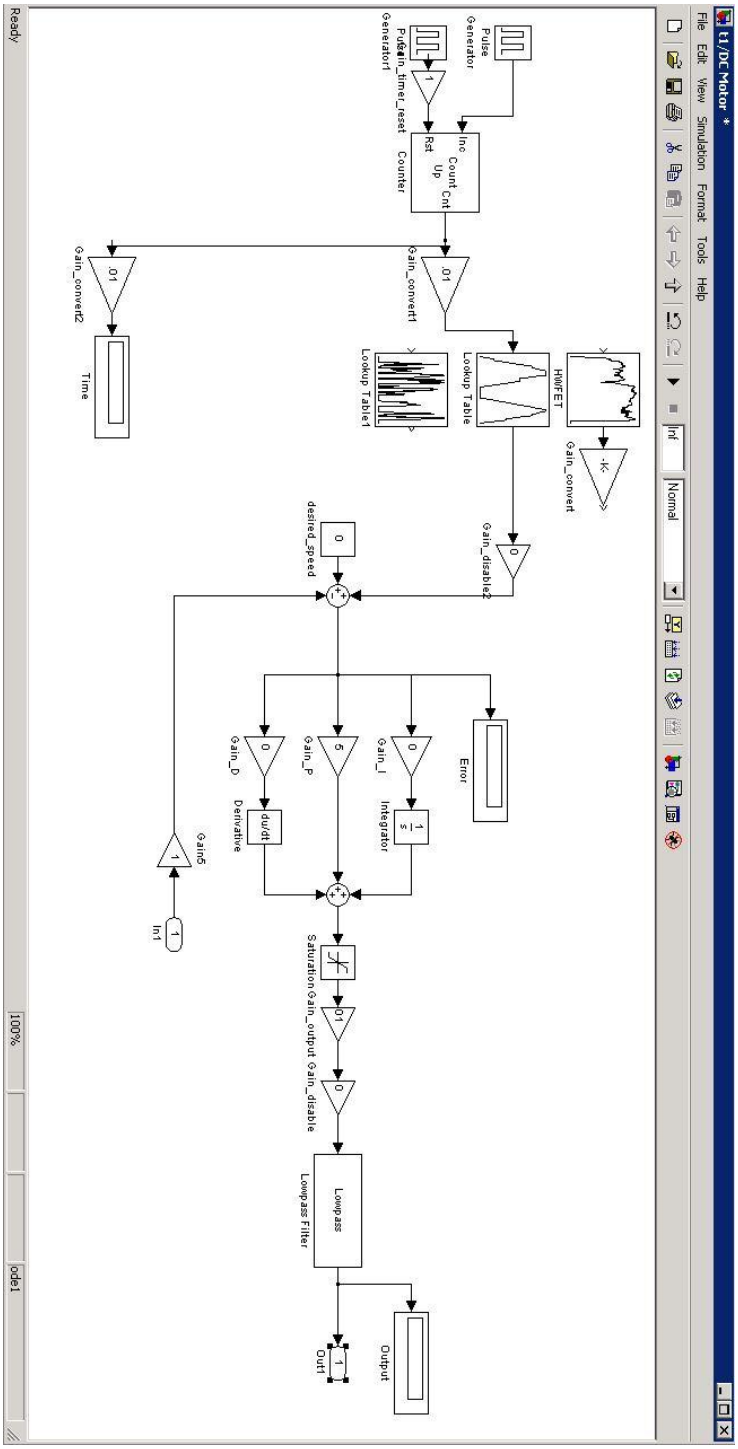

Appendix H Control desk layout

DC Motor Layout

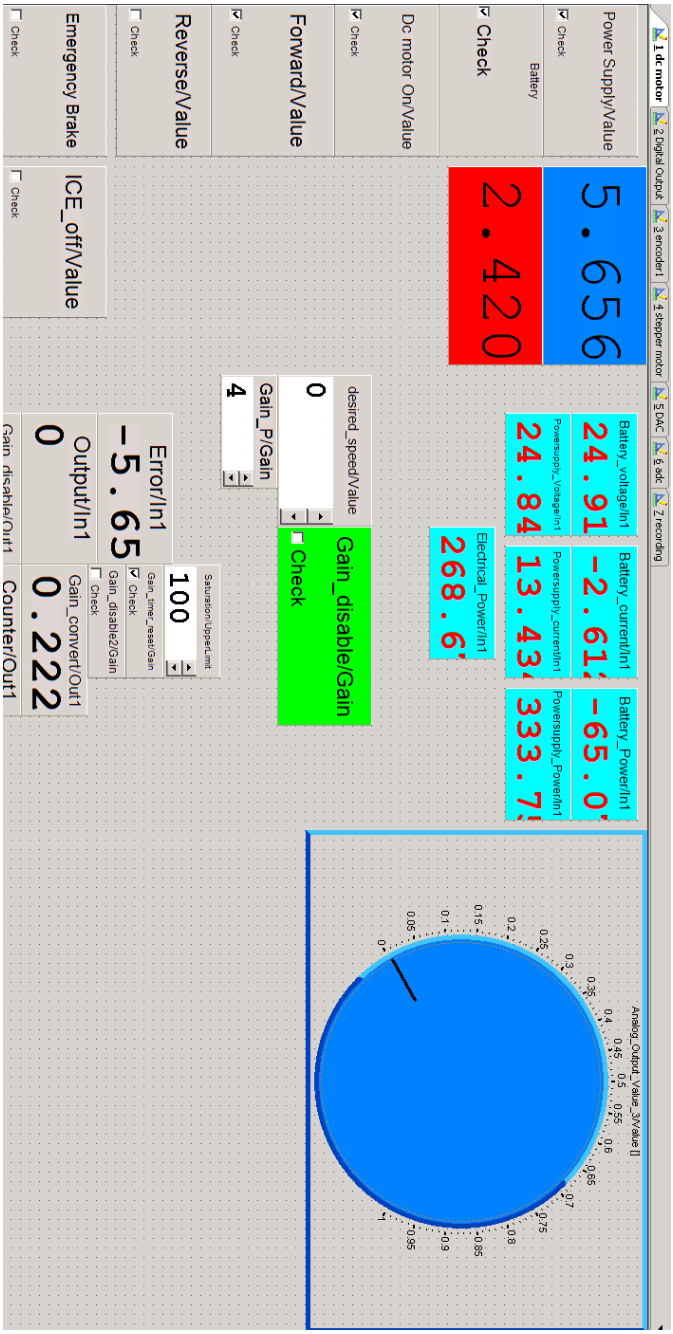

Digital Output Layout

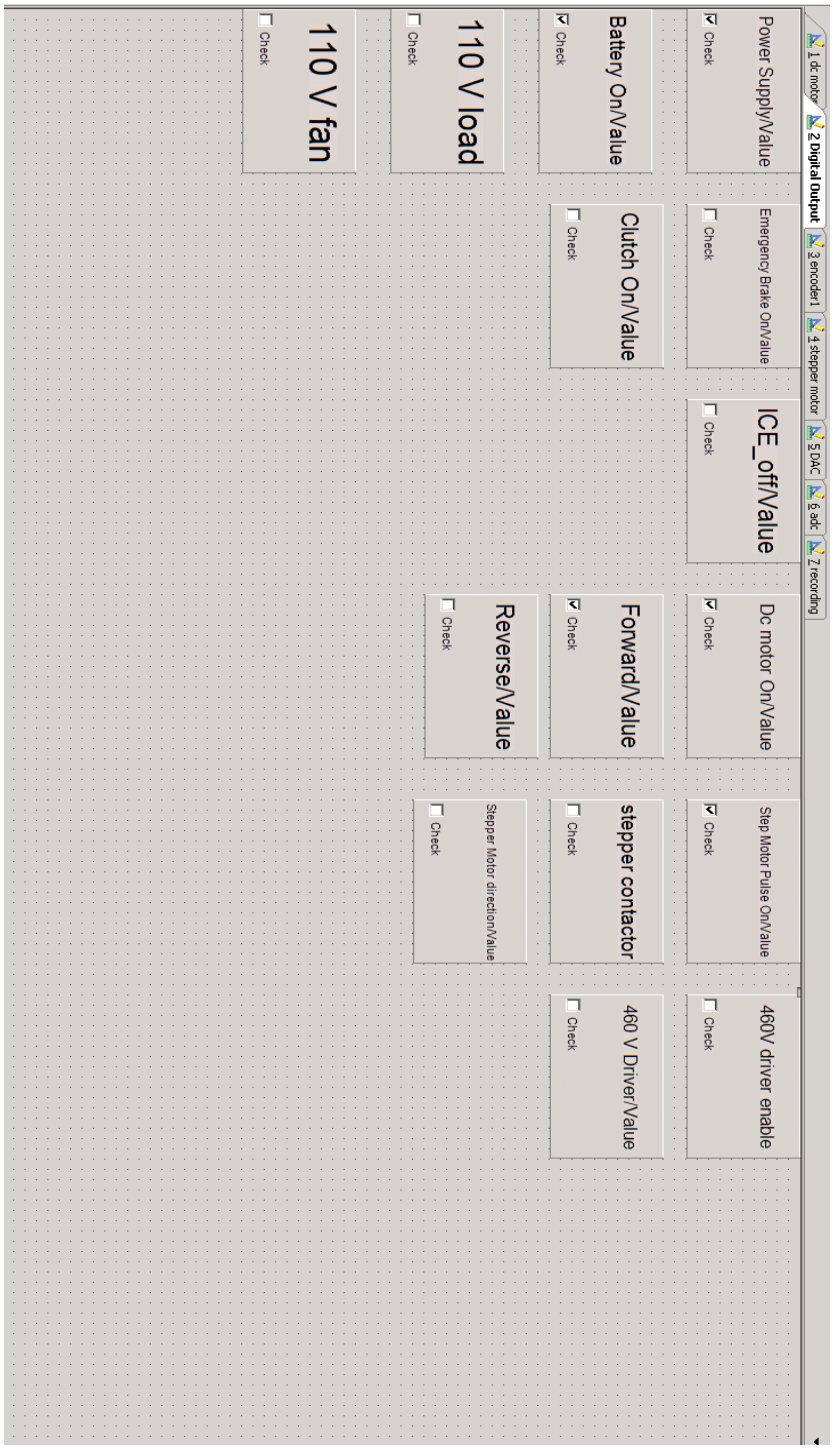

Encoders Layout

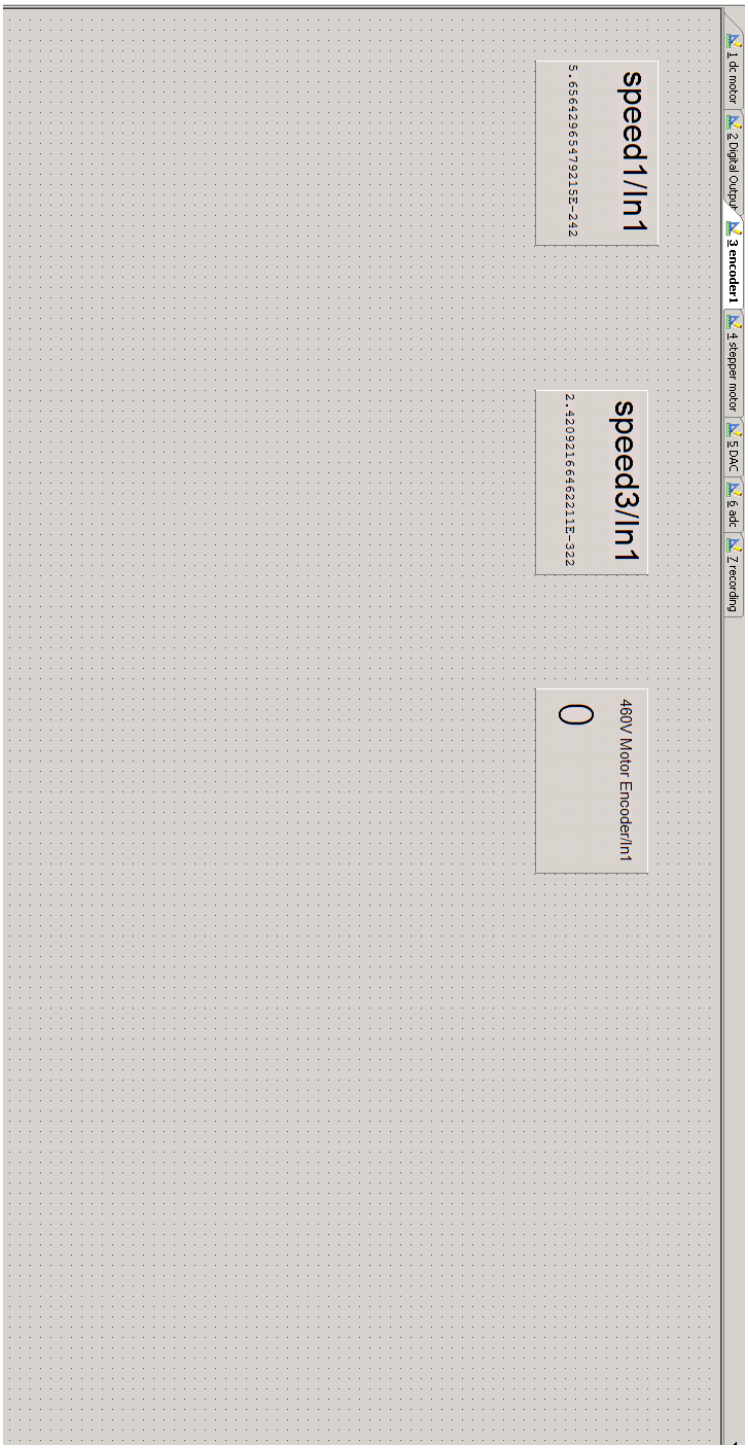

Stepper Motor Layout

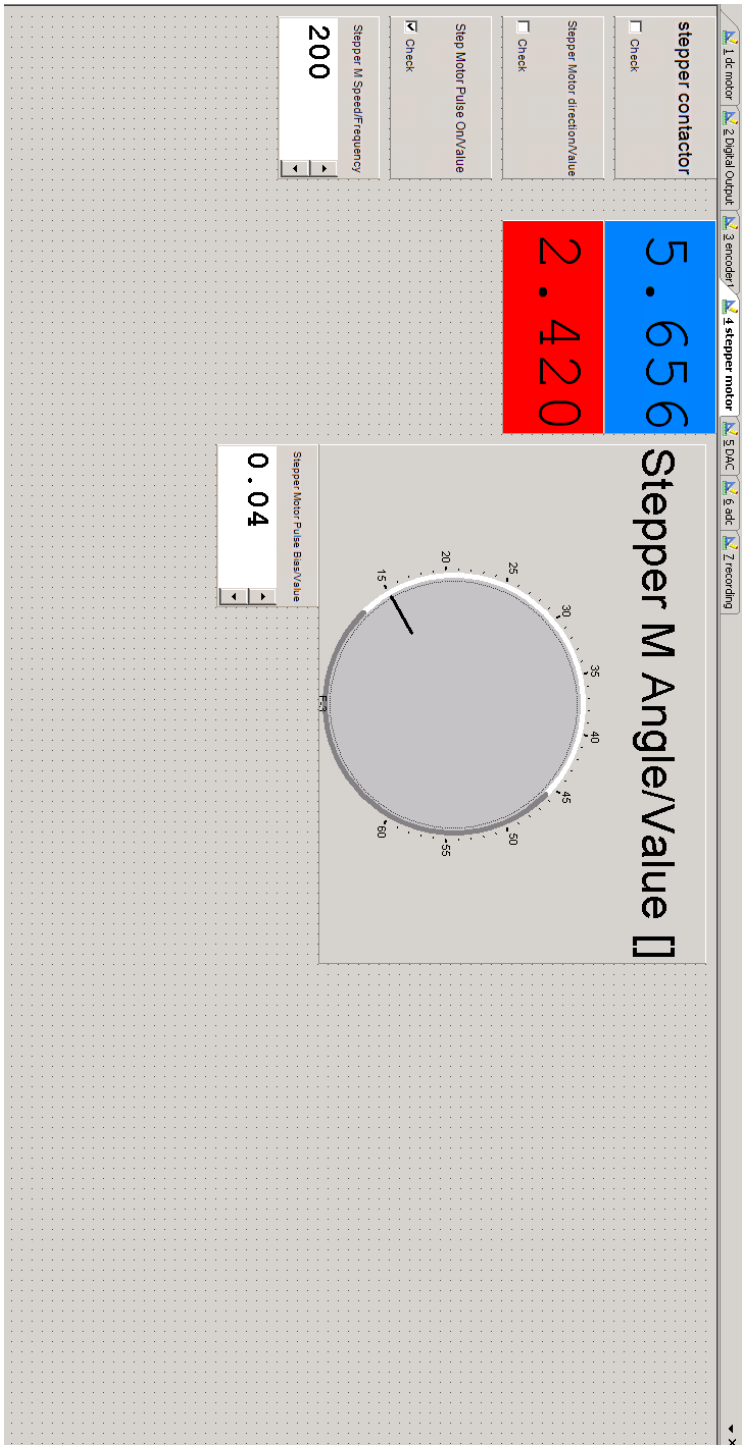

ADC layout

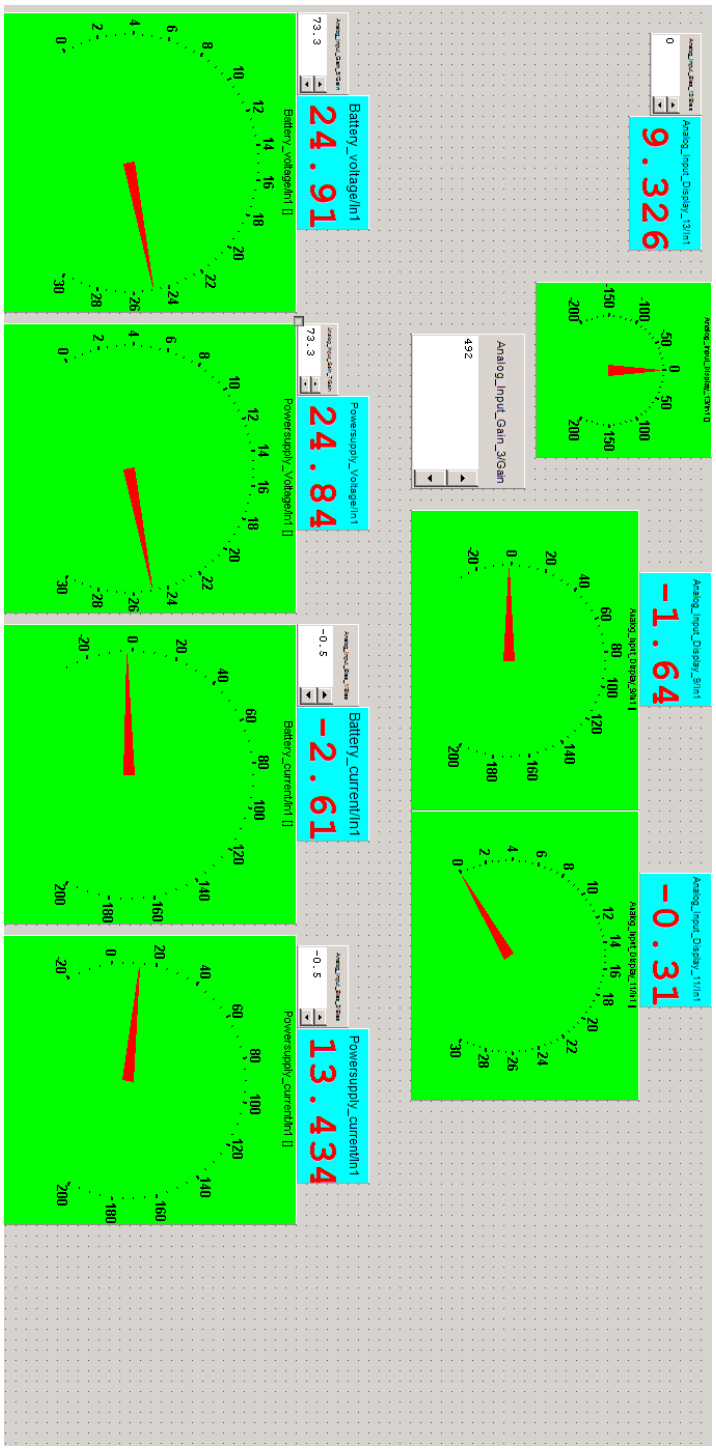
Battery_voltage/in1
24.91
Powersupply_Voltage/in1
24.84
Battery_current/in1
-2.61
Powersupply_current/in1
13.434
Analog_Input_Display_9/in1
-1.64
Analog_Input_Display_11/in1
-0.31
Analog_Input_Display_13/in1
9.326
Analog_Input_Gain_3/Gain
492

DAC Layout

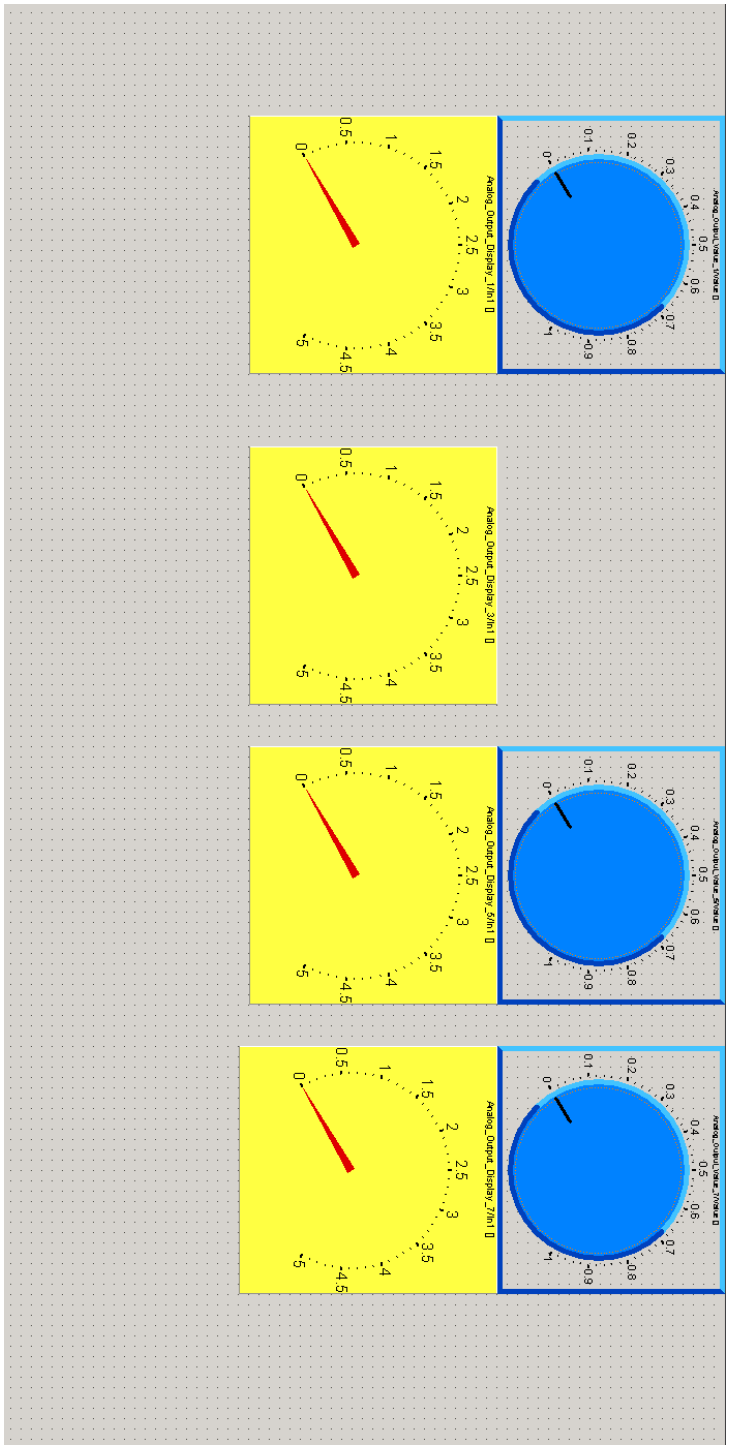

Recording Layout

Appendix I Additional Figures

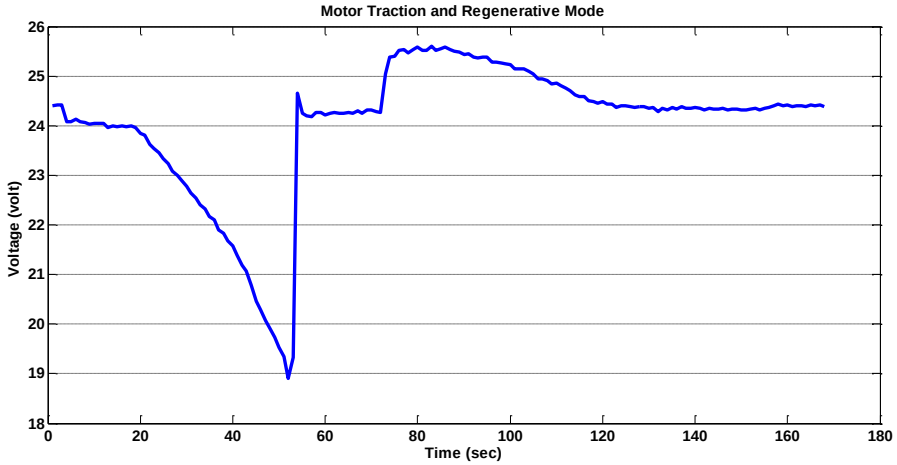

Figure 0-1: DC Motor Traction and Regenerative Mode Battery Voltage vs. time

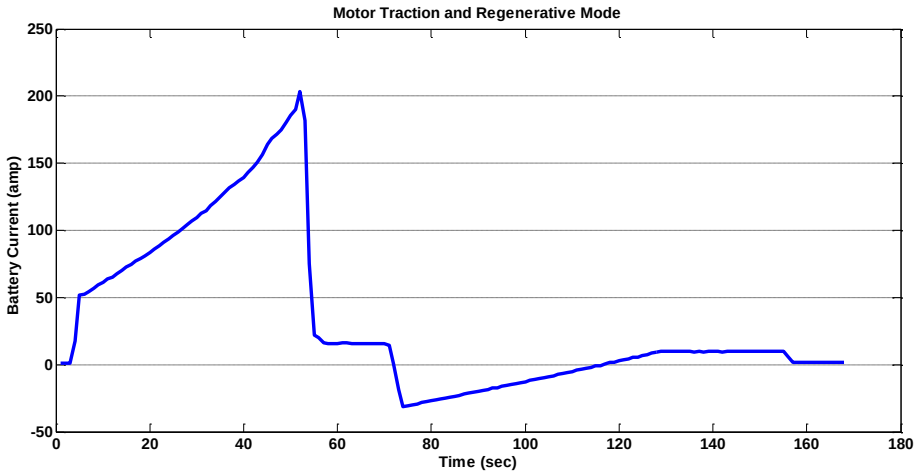

Figure 0-2: DC Motor Traction and Regenerative Mode, Battery Current vs. time

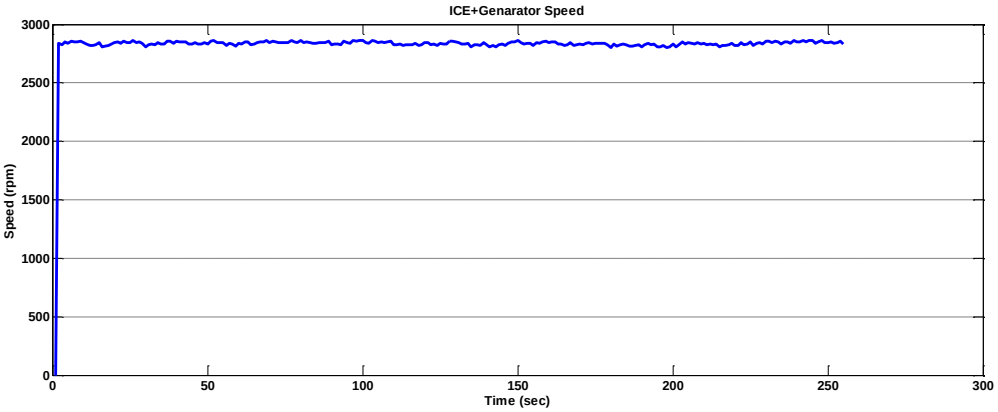

Figure A-0-3: ICE+ Generator speed

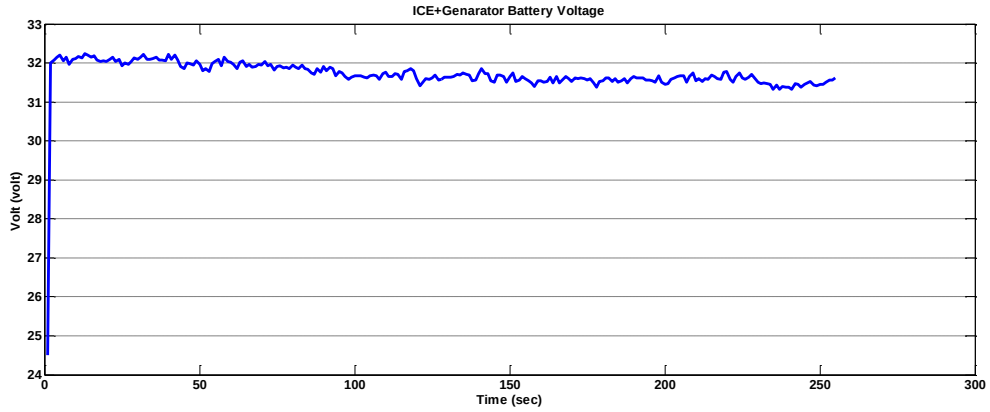

Figure 0-4: ICE + Generator Battery Voltage

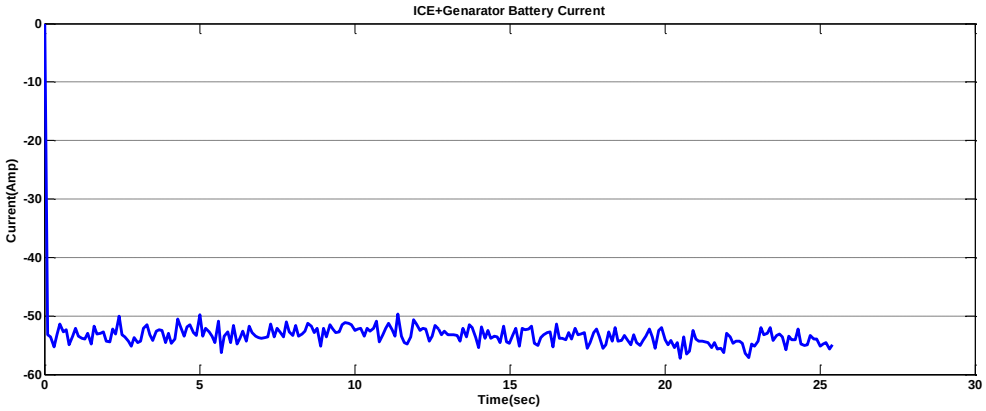

Figure 0-5: ICE + Generator Battery Current

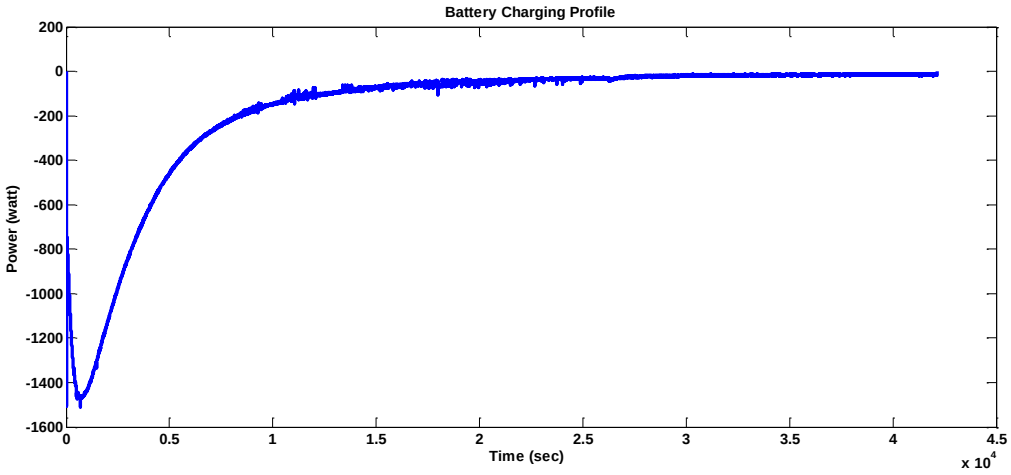

Figure 0-6: Battery charging Power vs. time